Cornell Center for Materials Research

Research Experience for Undergraduates

Summer Program 2015

Section 2

Support for the REU program is provided by the NSF MRSEC program (DMR-1120296) and the REU Site program (DMR-1063059).

Table of Contents

Endothelial Cell Matrix Stiffening and its Role in Atherosclerosis

Angelia Laudermilch, Marsha Lampi, Cythia Reinhart-King
Department of Biomedical Engineering, Cornell University, Ithaca, NY 14853

Abstract

Atherosclerosis is a disease of the arteries that involves the buildup of fatty plaques along the interior layer of the artery, which can contribute to cerebral vascular accident or myocardial infarction. The response of the endothelial cells to the dynamic stiffening of the artery is known to contribute to atherosclerosis. However, because the endothelium is the innermost layer of the artery, *in vivo* studies on entholeilial cell response to arterial stiffening are difficult to perform. By using a methacrylated hyaluronic acid gel (MeHA gel), a model developed by Guvendiren and Burdick[1], we are able to mimic the dynamic stiffening of the intima, the artery layer where the endothelial cells reside. This allows the behavior of the cells to be observed as their environment stiffens. We attempt to verify this model, as well as improve the visualization of the cell-cell junction behavior in response to changes in the mechanical stiffness of the extracellular matrix. This would allow the interface between soft and stiff tissue and the cells' response to this junction to be observed.

Introduction

Atherosclerosis is a growing problem with fatal implications. In fact, "in westernized societies, it is the underlying cause of 50% of all deaths."[2] As the artery stiffens with age, the area of the cells increase[3] and the junction width between cells expands, compromising the integrity of the cell-cell junctions. This allows leukocytes to cross the endothelial membrane and eventually can lead to the buildup of atherosclerotic plaques.[4] A plaque restricts blood flow and can also rupture, leading to further complications such as cardiovascular disease, the leading cause of death in the United States.[5]

While atherosclerosis can be accelerated by an unhealthy diet or aided by a genetic disposition[2], natural aging which leads to tissue stiffening can also contribute to atherogenesis. The earliest stage of atherosclerosis is the accumulation of macrophages surrounded by cholesterol, known as 'foam cells', which can be found in the human aorta in the first decade of life.[2]

In order to examine the junctions of endothelial cells, we used bovine aortic endothelial cells (BAECs). An *in vitro* hydrogel model of the intima capable of *in situ* stiffening was achieved using a technique developed by Guvendiren and Burdick[1]. A methacrylated hyaluronic acid (MeHA) gel is created that is first crosslinked with the addition of dithiothreitol (DTT) with a 15% weight to volume concentration. After the gel is seeded with cells, a technique that utilizes differential exposure to ultraviolet (UV) light allows the gel to stiffen as it photo-crosslinks. The cells are therefore grown on a surface that dynamically stiffens.

Methods and Materials

MeHA Gel Preparation

The MeHA gels were prepared with 22.0 mg MeHA polymer dissolved in 0.2 M triethanolamine (TE) buffer. The gel was polymerized after the addition of an adhesive peptide (arginine-glycine-aspartic acid, RGD)[1] on a 22x22mm glass coverslip in the dark for two hours before being

sterilized and seeded with BAECs. The concentration of MeHA in the gels was 15% mass to volume. This model was adopted from Guvendiren and Burdick.[1]

Cell Seeding

The BAECS were not used after the twelfth passage. The cells were seeded onto the MeHA gels with a density of 400,000 cells/gel. Cell culture was performed in M199 media. Incubation of the cells was controlled at 37° C and 5% carbon dioxide.

Ultraviolet Lighting System

The OmniCure Series 1500 was used for the UV light exposure. During the experiments, the wavelength used was 320-500nm. The power of the total exposure was measured as 10 mW/cm^2 using a light meter. The cells were exposed to UV light after forming confluent monolayers. Following UV exposure, the cells were allowed to recover for twenty-four hours followed by fixing and immunostaining.

Photo initiator

The photo initiator used was Irgacure with a 0.05% weight to volume concentration mixed with M199 media to promote photo-crosslinking of the MeHA gel during the UV exposure. The Irgacure provides free radicals to polymerize with the groups of methacrylate.[1] Each gel was submerged in a petri dish with 2mL of this solution for half an hour before exposure to UV to allow the Irgacure to diffuse into the gel.

Immunostaining

In order to image the BAECs on the MeHA gels, the cells were fixed with 3.2% paraformaldehyde. They were then stained with VE-Cadherin to study junction width or vinculin to examine focal adhesion behavior within cell junctions. Phalloidin was used to visualize the actin cytoskeleton.

Imaging

A fluorescent microscope was used in the reflected light setting for imaging the immunostained BAECs.

The live cells that were transduced were imaged using both the fluorescent microscope and the laser microscope.

Soft-Stiff Interface Imitation

The interface between soft and stiff was imitated by using a UV blocking film to cover half of the MeHA gel, only allowing half of the gel to crosslink further. This method was shown to block all UV light by using the UV light meter. The clear and opaque film was used in concurrence and was provided by UV Process Supply, Inc. During the UV exposure, the film is placed on top of the petri dish and covers half of the gel on the glass coverslip.

Mechanical Testing

The stiffness of the gels due to the exposure of UV light was determined using Atomic Force Microscopy (AFM). As previously mentioned, the ultraviolet light was set to 10 mW/cm^2. The stiffness of the control, 2 minute exposure, and 4 minute exposure gels were found to be 2.5 kPa, 6.5 kPa, and 11 kPa (Figure 1). This ensured that the cells on the MeHA gels were cultured within a physiologically relevant stiffness range.

Figure 1: The Mechanical testing yielded these values for the stiffness of the MeHA gels.

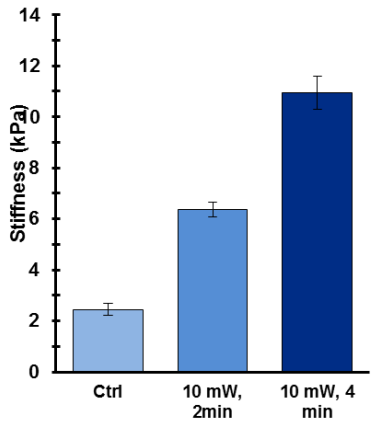

Live/Dead Assay

In order to ensure the viability of the cells after their exposure to UV light, a Live/Dead Assay was performed. The calcein and ethidium homodimer-1 dyes were purchased from Life Technologies.

Figure 2: a) Vinculin transduced into bovine aortic endothelial cells is a pRRL lentiviral backbone with vinculin mCherry. White arrows indicate focal adhesions.

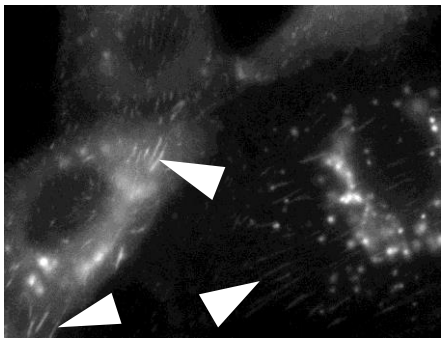

b) The lentivirus bound to other parts of the cell, creating bright fluorescent aggregates that impeded the imaging of the vinculin focal adhesions.

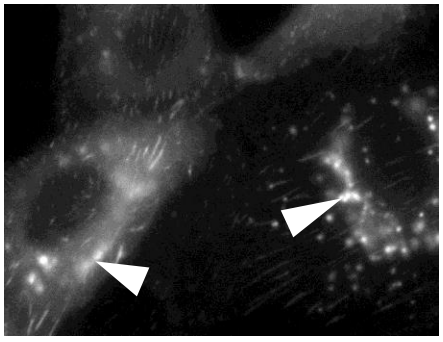

c) Immunostaining for vinculin shows no bright areas that disrupt the image.

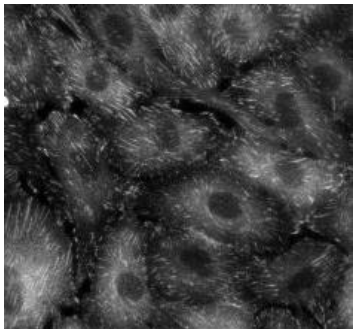

Results

Transduction of BAECs

To allow for real-time imaging of cell-cell junctions in living endothelial cells, the mCherry lentivirus was transduced onto the BAECs. Transduction is the insertion of genomic material into a mammalian cell through the use of a virus.[6] The mCherry lentivirus was used, providing a red color to bind to vinculin, a focal adhesion protein. Vinculin tightens junctions as they mature and prevents these junctions from opening.[7] Real time observation of vinculin would allow the junctions of the cell to be observed as they respond to the newly stiffened environment created by the photo cross-linked gel.

However, following transduction of the virus, the BAECs grew at a very slow rate, taking about twice as long to become confluent. While characteristic vinculin focal adhesions were seen in the endothelial cells (Figure 2a), the mCherry also bound to other material in the cell, causing bright aggregate spots throughout the cell and making the vinculin focal adhesions difficult to identify (Figure 2b).

We postulated the reason for these complications may stem from the vinculin sequence being of chicken origin and being transduced into bovine cells.

Interface of Soft and Stiff

One area of interest is the junction where soft and stiff substrates meet. The behavior of endothelial cells at this interface is significant due to the presence of differing stiffness *in vivo* due to disease. In order to examine the behavior of endothelial cells at the intersection of soft and stiff environments, we used an ultraviolet light blocking film as previously described. Only half of the gel was exposed to UV light and allowed to crosslink and become stiffer, while the other half remained unstiffened.

However, as the side of the gel that was exposed to UV light became stiffer, the gel swelled less due to increased crosslinking. Because of this, a large topographical difference occurred at the interface where the gel transitioned from soft to stiff. The different planes (Figure 3) make it very difficult to observe the behavior of the cells on the soft-stiff interface. Even more importantly, the topographical difference introduces another variable, as a difference in height may also alter endothelial cell behavior.

While the MeHA gel is useful for studying the endothelial cell response to a dynamically stiffening environment, the topological difference seen after photo crosslinking makes the application of the MeHA gel to examine the interface where soft and stiff environments meet somewhat limited.

Figure 3: The interface of soft and stiff was difficult to image because of the difference in topography. The gel that was exposed to no UV (a), the interface (b), and the gel that was exposed to UV (c) are all pictured. The difference in topology was up to 80 microns. The green color is actin, the blue is the nucleus, and the red is VE-cadherin.

a)

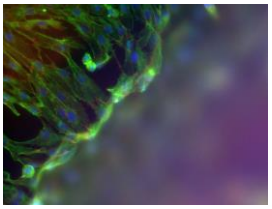

b)

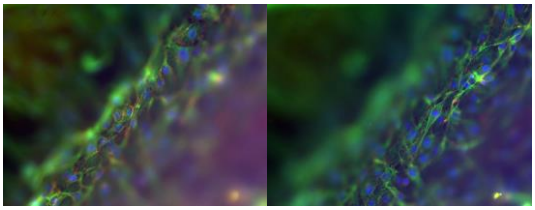

c)

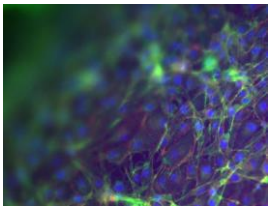

Conclusions and Future Directions

The use of a MeHA gel has allowed the dynamic stiffening of the intimal layer of the artery to be imitated and the response of the endothelial cells to be observed. After the stiffening of the gel by the use of ultraviolet light, the BAECs have increased area and increased junction width[1].

While the transduction of a virus into the BAECs was not useful for imaging in real time, useful information was gained concerning cell behavior and the response to new genetic material entering the genome. Using a lower amount of the mCherry lentivirus while transducing the BAECs may prevent the formation of vinculin aggregates because a decreased amount of the fluorescently tagged vinculin will be expressed.

The interface of soft and stiff was able to be imaged, but the MeHA gel does not allow the reaction of cells at the interface of a soft and stiff environment to be observed due to the dramatic topological difference present at the junction. The use of MeHA gels in the context of variable topography can lead to new applications, but for an examination of the stiffness interface, the process must be modified to prevent the large topographical changes in the substrate height we observed.

Regardless, the novel findings about endothelial cell behavior using MeHA hydrogels may lead to advancements in preventing endothelial barrier disruption caused by matrix stiffening. The tissues, including the arteries, naturally stiffen as the body ages, but the response to this stiffening, the spreading of the cells and the compromising of the cell-cell junction integrity leading to increased permeability, may be intercepted and delayed if the

response of the cells to their stiffening environment can be slowed and minimized.

Acknowledgments

Experiments were performed in the lab of Dr. Cynthia Reinhart-King. The work was supervised by PhD candidate Marsha Lampi, often in conjunction with undergraduate student, John Pollack.

This work was supported by the Cornell Center for Materials Research with funding from the Research Experience for Undergraduates program (DMR-1062059 and DMR-1120296).

References

1. Guvendiren M, Burdick J a. Stiffening hydrogels to probe short- and long-term cellular responses to dynamic mechanics. *Nat Commun*. 2012;3:792. doi:10.1038/ncomms1792.

2. Lusis A. Atherosclerosis. *Nature*. 2000;407(6801):233-241. doi:10.1038/35025203.Atherosclerosis.

3. Stroka K. Effects of Morphology vs. Cell-Cell Interactions on Endothelial Cell Stiffness. *Changes*. 2012;29(6):997-1003. doi:10.1016/j.biotechadv.2011.08.021.Secreted.

4. Huynh J, Nishimura N, Rana K, et al. Age-Related Intimal Stiffening Enhances Endothelial Permeability and Leukocyte Transmigration. *Sci Transl Med*. 2011;3(112):112ra122-112ra122. doi:10.1126/scitranslmed.3002761.

5. Libby P. Inflammation in atherosclerosis. *Nature*. 2002;420(6917):868-874. doi:10.1038/nature01323.

6. Thierauf A, Perez G, Maloy AS. Generalized transduction. *Methods Mol Biol*. 2009;501:267-286. doi:10.1007/978-1-60327-164-6_23.

7. Huveneers S, Oldenburg J, Spanjaard E, et al. Vinculin associates with endothelial VE-cadherin junctions to control force-dependent remodeling. *J Cell Biol*. 2012;196(5):641-652. doi:10.1083/jcb.201108120.

Synthesis and Characterization of Vaporizable Polycarbonates and Polyurethanes as Potential Substrates for Transient Devices

Stephanie Liffland[1], Katherine Camera[2], Christopher K. Ober[3]

[1]*Department of Chemistry, The University of North Carolina at Chapel Hill, Chapel Hill, NC*
[2]*Department of Chemistry and Chemical Biology, Cornell University, Ithaca, NY*
[3]*Department of Materials Science and Engineering, Cornell University, Ithaca, NY*

Abstract

Transient materials are of great interest to many research fields, with applications in vaporizable electronics, medical implants, remote environmental sensors, and in any device with an element of time dependency. These materials are designed with the ability to decompose in a programmable manner, with degradation caused by a specific trigger. Polymers offer a diverse platform for the development of transient substrates because they can be synthesized with tunable characteristics for desired transient properties, such as high molecular weight and rapid thermal degradation. In this study, both polycarbonate and polyurethane (PU) systems are investigated as potential platforms for transient substrates with a thermally-triggered degradation. The coupling of Novomer 212-20 macro-diol with both bis(carbonylimidazolide) and terephthaloyl chloride coupling agents was investigated to synthesize a polycarbonate system. Despite variations in reaction conditions, high molecular weight was not achieved. A PU system was synthesized using Novomer 212-20 (as a macro-diol), a chain extender, and an isocyanate. The relationship between composition and thermal properties was investigated through systematic variation in mole ratio of macro-diol to chain extender during PU synthesis. The resulting PUs were characterized using gel permeation chromatography (GPC) and thermogravimetric analysis (TGA). GPC results show varying molecular weights from 2.7 – 11.0 kDa, with a weight dependence on macro-diol to chain extender ratio. The TGA results show the synthesized PUs have varying degradation temperatures from 184 to 239 °C. The degradation temperature was also found to be dependent on the macro-diol to chain extender ratio, with an increase in macro-diol content leading to an increase in degradation temperature. This PU system provides tunable molecular weight and thermal degradation, leaving less than 10% material remaining.

Introduction

The development of transient electronics, which have pre-engineered life spans, is of great interest to meet the evolving needs of modern consumers. Transient materials are designed with the ability to degrade in a matter that is both controlled and programmable, providing a level of operational control that was previously unattainable. Devices that are composed of materials with transient properties have unique applications as remote environmental sensors, medical

implants, and as technological components that have an element of time dependency.[1] The further development of these transient materials is critical for the advancement of this technology and its eventual integration into modern manufacturing.

Polymeric materials provide beneficial properties as substrates for transient electronic devices. Polymers, which are long chain macromolecules comprised of repeating subunits, have tunable characteristics that make them ideal for numerous applications, including coatings, adhesives, and encapsulants. The tunable nature of polymer synthesis and the extensive number of polymers able to be synthesized makes them an ideal candidate for transient materials.

For controlled transience to be attained and a polymeric material to be considered as a potential device substrate, it must demonstrate several specific properties: i) having a high young's modulus to achieve stiff materials and prevent substrate deformation, ii) displaying a high molecular weight to allow the formation of thick, stable films, and most importantly iii) undergoing rapid depolymerization upon the onset of a specific trigger that destroys the substrate and renders the device unusable. These properties are necessary to achieve stable substrates that can withstand the rigors of usage but that also display programmable transience.

Past work has set about achieving these properties through a variety of polymer composite systems that employ various triggering mechanisms. White et al. has demonstrated successful material transience through the use a cyclic poly(pthalaldehyde) (cPPA) substrate with a photo-acid generator (PAG) additive. The system employs UV light as a triggering mechanism to activate the depolymerization of the substrate via chain unzipping and decomposition of the device.[1] Other systems utilize different triggers, relying on chemical, mechanical, or thermal triggers to activate degradation.[2-4]

We have chosen to pursue a thermal triggering method to achieve transience, focusing on the designed synthesis of two potential substrate materials: i) a polycarbonate or ii) a polyurethane system, both with an acid additive in the form of a thermal-acid generator (TAG) to catalyze degradation via chain scission. Polycarbonates can be designed and synthesized with a variety of structures, allowing for a tunable range of systems to help meet process and device needs.[5] These polycarbonates can be designed with small organic components bridging the carbonate groups so when they degrade they release small, volatile organics and carbon dioxide, allowing for complete transience of the polymer. Control over synthesis allows for the formation of a polymer in which there is a tertiary carbon next to the carbonate group within the polymer backbone, helping to facilitate thermal degradation. [6]

Polyurethanes (PUs) are another promising system due to their tunable thermal stability and low heat resistance. [7] The thermal stability of PUs can be tuned to fit the needs of a transient material by varying aspects of the synthesis method, including the ratio of hard segments and soft segments (i.e. NCO:OH ratio) within the polymer backbone, concentration of catalysts used, selection of raw material components, and reaction temperature. [8] By controlling these aspects during the polymerization, varying PUs can be systematically studied to determine and

achieve favorable film formation and subsequent thermal degradation.

In this study we will investigate multiple polycarbonate and PU systems to determine which has the most promising properties for transient packaging. Characterization of these polymers, including NMR and GPC to confirm polymer formation, as well as thermal analysis using TGA, will be conducted. To achieve desired transient packaging properties, our polymers should have molecular weights above 15 kDa, be able to form films on the order of 100 – 300 μm, and have thermal degradation (either catalyzed by acid or uncatalyzed) below 200 °C.

Experimental

i) Synthesis of bis(carbonylimidazolide) of 2,5-dimethyl-2, 5-hexanediol [6] [Scheme 1a]

A solution of 2,5-dimethyl-2, 5-hexanediol (20.0 g, 0.137 mol) dissolved in 200 mL of dry THF was allowed to slowly stir under Nitrogen atmosphere for 10 minutes. Nitrogen gas was then bubbled into the solution for 10 minutes, while stirring continued. The bubbler was then removed and the solution treated with 1 g of potassium metal. The reaction mixture was then allowed to reflux at 80 °C for two hours, or until all of the potassium metal had fully reacted. The solution was then cooled to 30 °C and transferred, under nitrogen, dropwise via cannula to a secondary flask prepared with a stirring solution of 1,1'-carbonyldiimidazole (44.3 g, 0.274 mol) in 100 mL dry THF. After transfer was complete, the solution was heated to 65 °C for 1 hour. A small amount of water was added to the reaction mixture, followed by ~150 mL ethyl acetate. The resulting solution was then washed with distilled water three times. The washed organic layer was dried over a short plug of silica gel and sodium sulfate and rinsed with ethyl acetate. The ethyl acetate was then removed via rotary evaporation to yield 43.4 g of product (95% yield). The resulting powder was dried in the vacuum oven at room temperature for 1 hour and stored in the freezer.

ii) CVPC Polymerization [6] [Scheme 1b]

A mixture of the bis(carbonylimidazolide) monomer (12.0 g, 0.036 mol) and 1,4-cyclohexanediol (4.17 g, 0.036 mol) was added to a flask and flushed with Nitrogen for 1 h. The reaction mixture was then dissolved in 35 mL DCM, and treated with 18-crown-6 (0.720 g, 0.0027 mol) and powdered potassium carbonate (23.9 g, 0.173 mol). The solution was heated to 65°C and allowed to reflux overnight while stirring vigorously to ensure high conversion. The reaction mixture was then removed from the heat and filtered to remove any remaining potassium carbonate. The resulting filtrate was collected and concentrated via rotary evaporation. Final recovery of the polymer was accomplished by precipitation of the concentrated solution in methanol while stirring vigorously. The precipitate was filtered and allowed to dry in the vacuum oven at room temperature overnight.

iii) Bis(carbonylimidazolide) and Novomer 212-20 coupling [Scheme 1c]

The polymerization was carried out as described for the preparation of CVPC, using Novomer 212-20 in place of 1,4-cyclohexanediol. Upon workup, the concentrated solution did not precipitate well into methanol. No visible precipitate formed, so 100 mL of distilled water was added to the solution and the mixture was left to sit overnight in an ice bath without

a) Bis(carbonylimidazolide) of 2,5-dimethyl-2, 5-hexanediol monomer

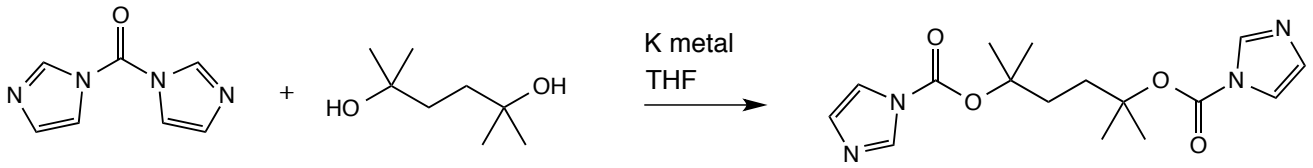

b) CVPC

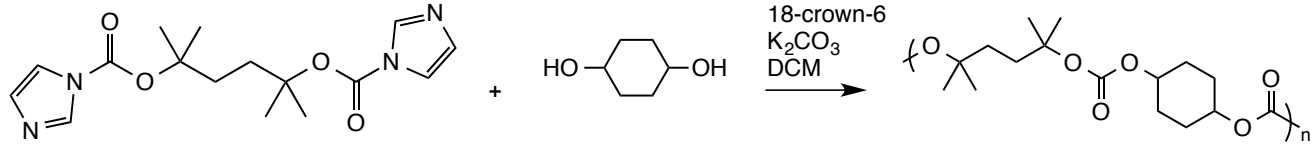

c) Bis(carbonylimidazolide) and Novomer 212-20 coupled polymer

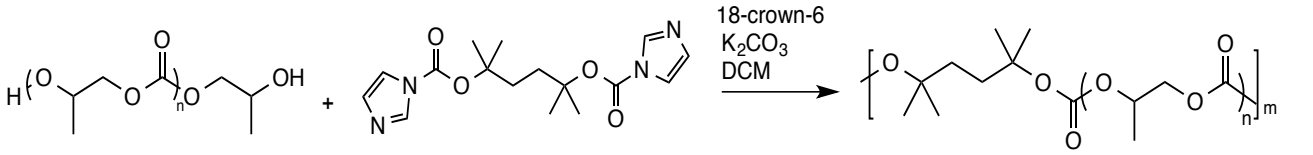

d) Terepthaloyl chloride and Novomer 212-20 coupled polymer

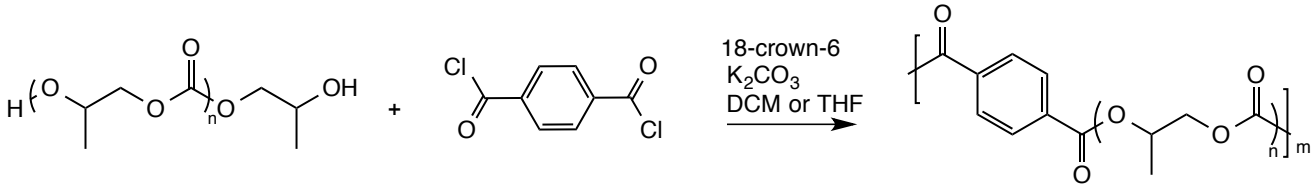

e) Polyurethane

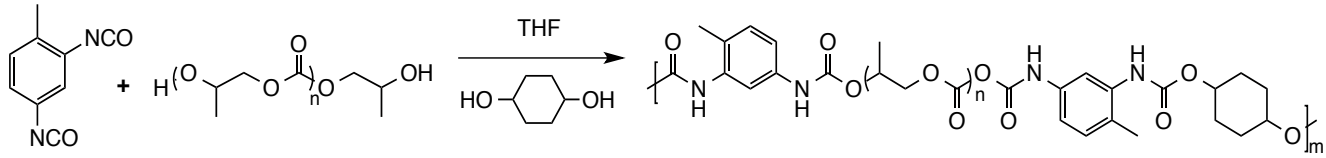

Scheme 1. Reaction schemes for synthesis of bis(carbonylimidazolide) of 2,5-dimethyl-2, 5-hexanediol, CVPC, coupled Novomer 212-20 macro-diol, and polyurethanes.

stirring. There was no visible precipitate after 24 h. In an attempt to remove the solvents the solution was rotovapped. The resulting concentrated product was amber in color with a small amount of precipitate. The precipitate was characterized by NMR.

iv) Terephthaloyl Chloride and Novomer 212-20 Coupling reaction [Scheme 1d]

A solution of Novomer 212-20 (4.017g, 0.002 mol) dissolved in 30 mL of dry THF was allowed to stir for 10 min at room temperature. The reaction mixture was then treated with triethylamine (TEA) (0.614 mL,

0.0044 mol) and allowed to stir vigorously for 3 hours. A solution of terephthaloyl chloride (TCl) [0.408 g, 0.002 mol] was dissolved in 3 mL dry THF and drawn into a 5 mL syringe. A portion of the TCl/THF solution (75%) was added to the reaction mixture and left to stir overnight. The remaining 25% of the TCl/THF solution was added slowly to the reaction mixture over 8 hours. Once addition of the TCl/THF solution was complete the reaction mixture was allowed to stir vigorously overnight. The resulting solution was concentrated via rotary evaporation, and final recover of the polymer accomplished via precipitation in methanol. The collected polymer was then dried in the vacuum oven overnight.

v) Terephthaloyl Chloride and Novomer 212-20 Coupling reaction [Scheme 1d]

The polymerization was attempted as described for coupling reaction (iv), using NaH (0.111 g, 0.0044 mol) in place of TEA. Upon workup, the concentrated solution was precipitated into methanol, generating a fine, white powder in solution. Attempts to filter out the precipitate were unsuccessful. To aid in aggregation of the precipitate 200 mL of distilled water were added to the mixture, which was allowed to stir for 3 h before sitting overnight without stirring. The precipitate was too fine for filtration, so the solution was removed via rotary evaporation. The remaining solid was then placed in the vacuum oven overnight at 50°C. The resulting precipitate was analyzed via GPC and NMR.

vi) Terephthaloyl Chloride and Novomer 212-20 Coupling reaction [Scheme 1d]

The polymerization was attempted as described for coupling reaction (iv), using potassium carbonate (0.619 g, 0.045 mol) in place of TEA. Upon workup, the concentrated solution did not precipitate out in methanol. Rotary evaporation was then used in an attempt to remove remaining solvent, leaving a viscous liquid.

vii) Terephthaloyl Chloride and Novomer 212-20 Coupling reaction [Scheme 1d]

The polymerization was attempted as described for coupling reaction [iv (I)], using potassium carbonate (0.619 g, 0.045 mol) in place of TEA and changing the solvent to DCM in place of dry THF. Upon workup, the concentrated solution did not precipitate out in methanol. Rotary evaporation was then used in an attempt to remove remaining solvent, leaving behind a viscous liquid.

viii) Synthesis of Polyurethane via the pre-polymer method [Scheme 1e]

The preparation of the PUs was performed in a two-step process. The Novomer 212-20 was first degassed and dried in a flask under vacuum at 70 °C for 2 h. Under a nitrogen atmosphere, TDI (was added at an NCO/OH molar ratio of 2:1 and the reaction mixture dissolved in 35 mL dry THF. The solution was then heated to 80°C while stirring, and left to reflux for 2.5 hours to form the pre-polymer. A solution of 1,4-cyclohexanediol in dry THF was then added to the reaction mixture, and after 30 min the reaction was stopped. PU films were formed by casting the resulting solution in Teflon molds and allowing them to dry at ambient temperature overnight. The films were then placed under vacuum at ambient temperature for 6 h to remove any remaining solvent.

Characterization and Measurements

Gel Permeation chromatography (GPC)

The weight average molecular weight (M_w) and number average molecular weight (M_n) of synthesized samples was determined by

Table 1. Reaction conditions for Novomer 212-20 coupling.

Run no.	Monomer	Novomer	Base	Solvent	Results
1	BIS	212-20	K_2CO_3	DCM	No Coupling
2	TCI	212-20	K_2CO_3	THF	No Precipitation
3	TCI	212-20	K_2CO_3	DCM	No Precipitation
4	TCI	212-20	NaH	THF	No Coupling
5	TCI	212-20	TEA	THF	Partial Coupling

GPC. Analysis was performed on a Waters Ambient Temperature GPC equipped with a Waters 410 differential refractive indexer and a Waters 486 UV-Vis detector. The instrument was calibrated with Polystyrene standards using THF as the solvent.

Thermogravimetric analysis (TGA)

A TA Instruments Q500 instrument was used to analyze sample degradation properties. All samples were measured from ambient temperature to 600 °C at a heating rate of 10 °Cmin^{-1} in an air atmosphere flowing at 60 mLmin^{-1}.

Results and Discussion

CVPC

CVPC was successfully synthesized via the method shown in Scheme 1b, and was then characterized using GPC and TGA. The TGA analysis of CVPC is shown in Figure 1. Degradation of CVPC occurs over the temperature range of 180 to 236 °C, showing complete degradation of the polymeric material. The onset and 50% degradation temperatures (T_d) were determined to be 181 and 222 °C respectively. The steep curve from 100 to 0 wt.% of the weight% vs. temperature plot indicates rapid thermal degradation of the polymer into volatile components, leaving no residual material. While this rapid degradation fulfills the necessary characteristics for a transient substrate, the temperature range of this degradation falls slightly above the desired range. Acid catalysts can be explored to catalyze degradation and lower to 50% T_d.

The GPC data, shown in Figure 2, indicates the average M_W of CVPC as approximately 2 kDa. This molecular weight is below the necessary threshold to promote stable film formation, leading to brittle films. The mechanistic conditions of the condensation reaction scheme make it difficult to increase the molecular weight above a specific point. However, further conditions can be investigated to try to make CVPC a viable substrate material.

Coupling of Novomer 212-20

Multiple reactions conditions were systematically studied in an attempt to achieve a significant increase in molecular weight of Novomer 212-20, which can be

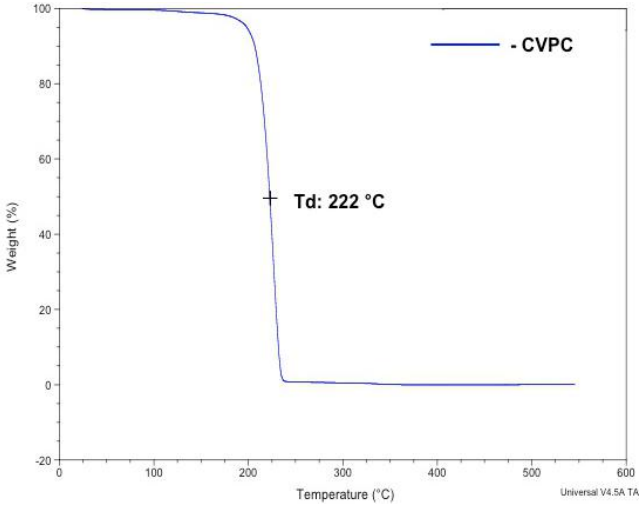

Figure 1. TGA plot of CVPC.

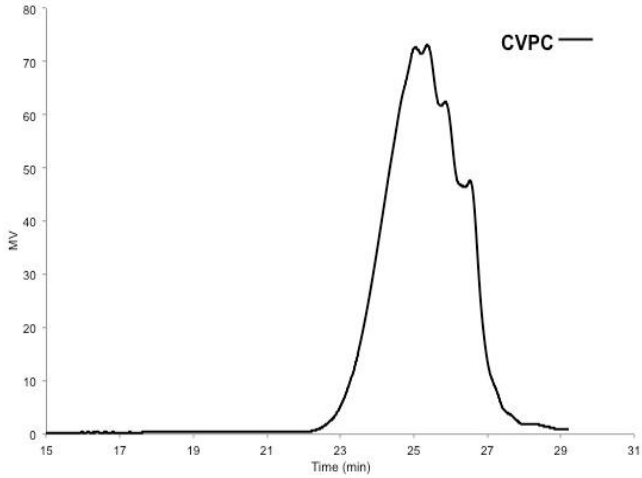

Figure 2. GPC plot of CVPC.

seen in Table 1. Unfortunately, significant increase in the molecular weight of the Novomer 212-20 diol via a coupling reaction was not achieved. The base, solvent, and coupling agent (monomer) were varied. The reactions resulted in either very little precipitation of a material or no precipitation at all. In Table 1, no precipitation indicates that a viscous liquid remained after purification attempts, and NMR showed these liquids to be starting materials. No coupling indicated that a small amount of precipitate was isolated during purification, but NMR revealed these to be starting materials. In Table 1, run 5 with TEA as the base, there was partial coupling of an isolated polymer. Figure 3 shows the GPC characterization, where the molecular weight of a fraction of the polymer was doubled to 4 kDa. This slight increase in M_w is likely due to a dimerization of some Novomer 212-20, but significant molecular weight increase was not achieved. Further investigation of reaction conditions with TEA can be tested in order to try to increase the molecular weight.

Polyurethanes

A variety of PUs were successfully synthesized via the method shown in Scheme 1e. The reaction conditions used and properties of each synthesized PU can be seen in Table 2. By varying the mole ratio of Novomer 212-20 (macro-diol) and 1,4-cycyloheanediol (chain extender), the effect of PU composition on thermal properties of the material could be investigated

The resulting PUs had M_n ranging from 2.7 kDa to 11 kDa and M_w ranging from 2.7 to 57.2 kDa as can be seen in Table 2. The trial which contained a 1:1 ratio of diol to chain extender was not soluble in THF and was therefore unable to be analyzed via GPC. Plots for the remaining PU samples are represented in Figure 4. The samples containing a 1.25:0.75 and 1.5:0.5 mole ratio of diol to chain extender display a broad overall peak composed of four smaller peaks. The

Table 2. Reaction conditions for PU synthesis.

Run no.	Diol: chain extender (mole ratio)	Novomer	Reaction		Polyurethane		
			Temp. (°C)	Time (h)	M_n [a] (kDa)	M_w [b] (kDa)	T_d [c] (°C)
1.	1:1	212-20	80	3	--	--	184
2.	1.25:0.75	212-20	80	3	11.0	57.2	195
3.	1.5:0.5	212-20	80	3	10.2	39.0	198
4.	2:0	212-20	80	3	2.7	2.7	239

a. Number average molecular weight
b. Weight average molecular weight
c. 50% degradation temperature

broad nature and multiple sub-peaks of the GPC plot lead to the discrepancy between M_n and M_w for the PU samples. The peaks of lower M_p lead to a lowering in the overall M_n and the peaks with higher M_p bring up the M_w widening the disparity between the two calculated values.

Unlike the samples containing both the macro-diol and chain extender, the plot for the sample containing a 2:0 ratio of macro-diol to chain extender displays only one distinct peak with a M_n of approximately 2.7 kDa. The uniformity of chain length and lower M_n is likely due to the lack of chain extender, eliminating reaction between the short pre-polymer chains. Further investigation of reaction conditions and chain extenders used may aid in increasing overall molecular weight and improving the homogeneity of the PU systems.

The calculated M_n for the three PUs show a trend within the system. The PU samples containing the greatest amount of chain extender (1.25:0.75) displayed the highest calculated M_n at 11 kDa. By increasing the ratio of macro-diol to chain extender to 1.5:0.5, the resulting PU displayed a lower M_n at 10.2 kDa. The final PU, with a ratio of 2:0 diol to chain extender, had a significantly lower M_n of 2.7 kDa. This trend suggests PUs containing a higher mole ratio of chain extender display a higher overall molecular weight.

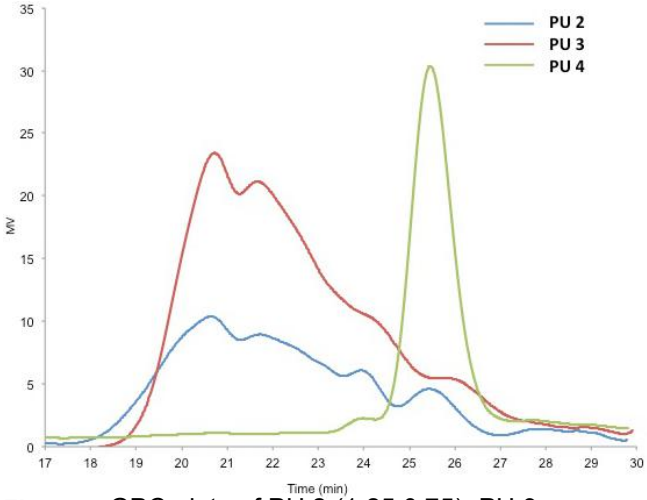

Figure 4. GPC plots of PU 2 (1.25:0.75), PU 3 (1.5:0.5), and PU 4 (2:0).

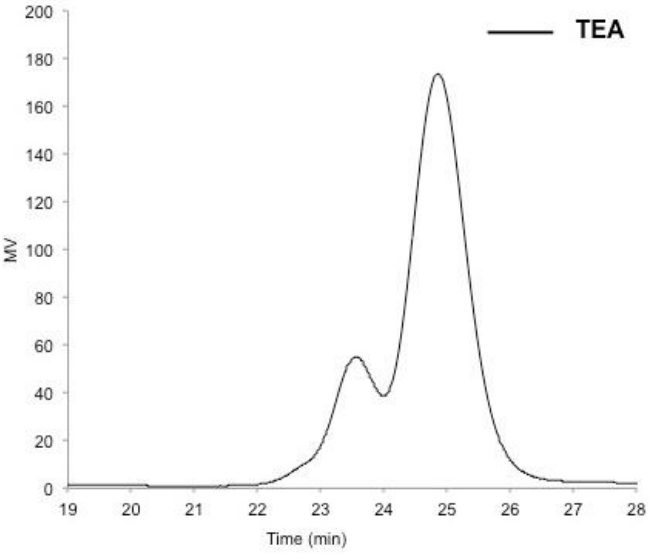

Figure 3. GPC plot of Novomer 212-20 coupling using TEA as base and THF as solvent.

The change in mole ratio of PU composition also affected the solubility of the polymers. As composition moved away from the 1:1 mole ratio, the synthesized PUs became more soluble in selected solvents, including THF and DMF, making processing easier than with the 1:1 mole ratio PU.

Thermal stability and thermal degradation of the PU systems were investigated using TGA. The TG curves of the varying samples are represented in Figure 5, and the 50% T_d are listed in Table 2. The thermal analysis of the PU system shows a distinct trend in overall thermal stability with changing mole ration of macro-diol to chain extender. A comparison of the 50% T_d of the synthesized PUs shows a range of degradation temperatures from 184 to 239 °C. A 1:1 mole ratio of macro-diol to chain extender displayed the lowest onset and 50% T_d of 154 and 184 °C respectively. By increasing

Table 3. M_p values for GPC plots of PU 2, PU 3, & PU 4.

Run no.	Diol: chain extender (mole ratio)	Peak M_p (kDa)			
		1	2	3	4
PU 1	1:1	--	--	--	--
PU 2	1.25:0.75	69.0	20.4	5.6	2.6
PU 3	1.5:0.5	60.7	20.6	4.8	1.9
PU 4	2:0	2.7	--	--	--

the ratio of macro-diol to chain extender to 1.25:0.75, the resulting PU displayed both higher onset and 50% T_d of 167 and 194 °C. This trend continues in the remaining PUs, with samples containing a higher mole ratio of macro-diol to chain extender displaying higher onset and 50% T_ds.

The PUs display an initial steep degradation curve, with 80% of degradation occurring over a 30 °C temperature range. As can be seen in the Weight % versus Temperature plot in Figure 5, the PUs display a secondary degradation event with approximately 20 wt.% of the sample remaining. This secondary degradation occurs over a larger temperature range, approximately 80 °C and plateaus slightly above 0 wt.%, indicating that sample degradation leaves minimal residual material. While complete sample degradation extends over a larger temperature range than desired for a transient substrate.

Thermal degradation of the PU systems in the presence of a thermal acid generator (TAG), 2,4,5-trichlorobenzosulfonic acid, was investigated via TGA to determine if an acid catalysts could be used to lower the T_d. The TG curves of the various samples are represented in Figure 6. The acid catalyzed degradation curves do not exhibit the same trend as seen in the uncatalyzed samples. For the PU systems containing both chain extender and macro-diol, the addition of the acid catalyst slightly lowers the onset T_d, but significantly extends the degradation temperature range, widening the slope of the TG plot. This degradation behavior is not seen in the PU containing no chain extender with a mole ratio of 2:0 of macro-diol to chain extender. While the onset T_d is similar to the other acid catalyzed PU systems, the 50% T_d is significantly lower at 182 °C compared to the other catalyzed systems which range from 222 to 241 °C. While these degradation temperatures fall slightly above the desired range, the investigation into different potential acid catalysts may aid in achieving a T_d within the desired range.

These preliminary findings indicate that adjusting the ratio of macro-diol: chain extender may allow for systems with tunable thermal properties. Further variations on the mole ratio and investigation into other chain extenders, along with the use of an effective acid catalyst may lower the T_d and allow for further thermal control.

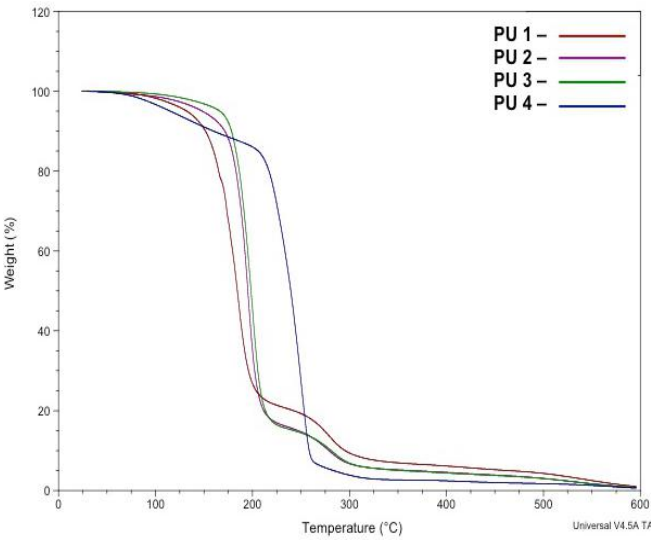

Figure 5. TGA plots of PU 1, PU 2, PU3, and PU 4.

Conclusions

We were able to successfully synthesize CVPC, a vaporizable polycarbonate and a series of PUs in the investigation of a potential transient substrate material. While these two reactions were successful, we were unable to achieve coupling of the Novomer 212-20 diol despite variation in base, solvent, and coupling agent (monomer) used. The resulting CVPC displayed an M_n of approximately 2 kDa and PUs had M_n ranging from 2 kDa to 11 kDa. The calculated M_n for the three PUs analyzed indicate a trend within the system with PU samples containing the greatest amount of chain extender displaying the highest M_n. Thermal analysis of the CVPC displayed a T_d of 222 °C and a steep degradation curve spanning 100 to 0 wt.%, indicating rapid degradation with no residual material left behind. By varying the mole ratio of macro-diol to chain extender during the PU synthesis, a system with tunable thermal properties was achieved. PU T_d was found to be between 184 and 239°C, with samples containing a higher mole ratio of macro-diol to chain extender displaying higher onset and 50% T_d. The PUs displayed T_ds lower than that of CVPC, but had a slower overall degradation. TGA curves for the PUs illustrated a two-step degradation process, while CVPC had a one-step degradation process.

Both the CVPC and PUs synthesized display favorable properties for transient materials, such as the rapid degradation of the CVPC and the high M_w of the PUs. However, each system requires further study to act as a viable substrate for transient devices. Due to the difficulty in increasing the M_w of CVPC given the nature of the polycondensation reaction, the higher M_w PU system provides the better option for a potential substrate material. However, to achieve favorable transience from a thermal trigger, the T_d must be lowered and degradation made more rapid. Further study and screening of potential acid catalysts can be attempted to significantly lower the T_d to the desired range and accelerate total degradation of the material. The higher M_w of the PUs presents the potential for favorable film formation. Investigation of film forming properties as well as testing of tensile strength and young's modulus will provide necessary information for viability of the material as a transient substrate. In addition, it will be beneficial to further explore the use of amine bases for the coupling of the Novomer 212-20, given the partial coupling of the trial using TEA. Additional adjustment of reaction condition may also be attempted to induce successful coupling.

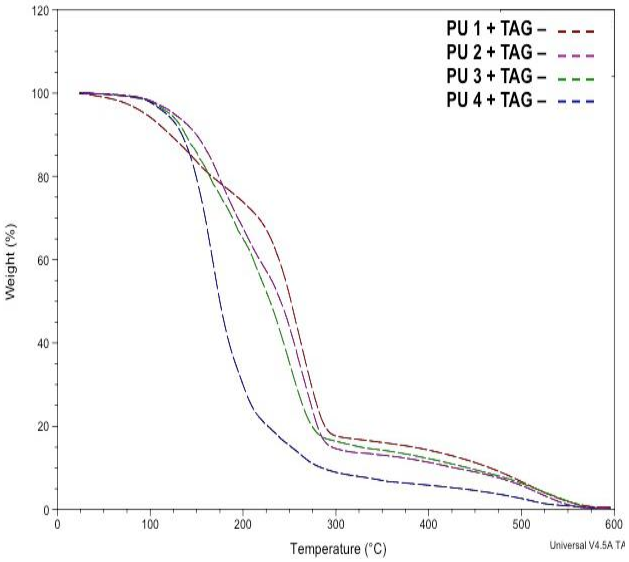

Figure 6. TGA plot of PU and acid catalyst (TAG) composites: PU 1 +TAG, PU 2 + TAG, PU 3 + TAG, and PU 4 + TAG.

Overall, these preliminary findings indicate that a viable transient substrate may be possible through the use of a PU and thermal-acid generator system. Results show that a tunable system in both M_w and

thermal properties can be achieved by varying polymer composition. Further development and investigation of polymer materials is important for the advancement and integration of transient devices.

Acknowledgments

This material is based on work supported by the NSF MRSEC Program (DMR-1120296) and the Defense Advanced Research Projects Agency.

References

(1) Hernandez, H. L.; Kang, S.-K.; Lee, O. P.; Hwang, S.-W.; Kaitz, J. a; Inci, B.; Park, C. W.; Chung, S.; Sottos, N. R.; Moore, J. S.; Rogers, J. a; White, S. R. *Adv. Mater.* **2014**, *26* (45), 7637–7642.

(2) Peterson, G. I.; Boydston, A. J. *Macromol. Rapid Commun.* **2014**, *35* (18), 1611–1614.

(3) Dilauro, A. M.; Robbins, J. S.; Phillips, S. T. *Macromolecules* **2013**, *46* (8), 2963–2968.

(4) Diesendruck, C. E.; Peterson, G. I.; Kulik, H. J.; Kaitz, J. a; Mar, B. D.; May, P. a; White, S. R.; Martínez, T. J.; Boydston, A. J.; Moore, J. S. *Nat. Chem.* **2014**, *6* (7), 623–628.

(5) Bendler, J.T.; *Handbook of Polycarbonate Science and Technology,* **1999,** CRC Press.

(6) Fréchet, J. M. J.; Houlihan, F. M.; Bouchard, F.; Kryczka, B.; Wilson, C. G. *J. Chem. Soc. Chem. Commun.* **1985**, No. 21, 1514.

(7) Petrovic, Z. S.; Zavargo, Z.; Flynn, J. H.; Macknight, W. J. *J. Appl. Polym. Sci.* **1994**, *51* (6), 1087–1095.

(8) Chattopadhyay, D. K.; Webster, D. C. *Progress in Polymer Science (Oxford)*. **2009**, 3*4* (10), 1068–1133.

Towards determining the oxidation mechanism of glucose using TiO_2 Nanoparticles Photoanode

Angel Ortiz, Justin Sambur, Peng Chen

Department of Chemistry and Chemical Biology, Cornell University.

Introduction:

With the recent problems of global warming and squandering of resources of the planet researchers have started to find different pathways for energy production. Among different strategies, semiconductor photocatalysis has been a subject of intense research since 1970[1]. Water splitting is said to be the "coal of the future" as Jules Vernes states; there is tremendous interest in the application of semiconductor electrodes for the photolysis of water[2]. This approach potentially provides an efficient, environmental way; to produce hydrogen an ideal chemical fuel[4]. Solar light driven reactions are also important for decontamination of water, and chemical synthesis. When semiconductors are excited by photons with energy equal to or higher than their band gap energy level, electrons are promoted from the valence band (VB) to conducting band (CB). For a model semiconductor like TiO_2, the reaction is expressed as[5]:

$$TiO_2 \xrightarrow{hv} e^-_{TiO_2} + h^+_{TiO_2}$$

A schematic energy level diagram for photocatalytic hydrogen production using TiO_2 is shown in Figure 1. The energy requirements for hydrogen production is as follows; the conduction band should be more negative than the H_2/H^+ redox potential production and the valence band should be more positive than the water oxidation potential (H_2O/O_2)[5] .

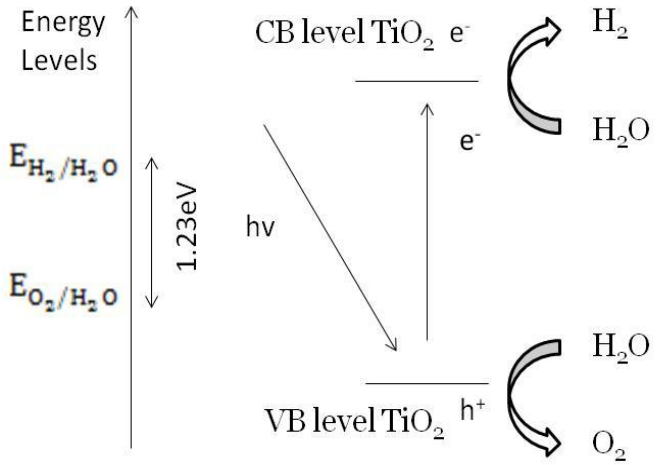

Figure 1. Energy level diagram of TiO_2 photocatalytic water-splitting[5].

Aside from solar hydrogen production, semiconductor photocatalysis can be used to oxidize many organic compounds (i.e., contaminants in groundwater). The oxidation mechanism of these compounds is not well understood. Some authors propose that molecules can be oxidized via a so-called direct mechanism or an indirect mechanism. This model is based on the fact that the photooxidation or these organic molecules will compete with the photooxidation of water molecules. In the indirect hole transfer mechanism the hole from the electrode first oxidizes water molecules to produce reactive intermediates (i.e., hydroxyl radical species $OH^{\bullet}$) that then oxidize organic molecule. On the other hand, holes from the semiconductor directly oxidize organic molecules in the direct mechanism. Salvador et al.[1] proposed a mechanistic model and predicted scaling relationships between observed reaction rates and incident light intensity and applied electrochemical potential. Using this model and scaling relationships, the oxidization mechanism of organic compounds like methanol and formic acid has been determined[1]. For glucose, the oxidation mechanism is unknown and the goal of this study is to elucidate this oxidation mechanism. St. John et al[3] showed that glucose oxidation and concurrent H_2 evolution occurs photoelectrochemically with metalized semiconductor powder, but the fundamental knowledge of the oxidation mechanism is not explained in this work.

Experimental Section:

Indium-doped tin oxide (ITO)-coated glass electrodes were treated with a solution of H_2O:NH_4OH:H_2O_2 for 30 minutes to make it more hydrophilic. TiO_2 nanoparticles (NPs) were prepared by dissolving 1g of Titanium Oxide, Aeroxide P25 (ACROS ORGANICS, A0328198) in 2mL solution of H_2O: EtOH 1:1. TiO_2 NPs were deposited on the ITO via spin coating technique. The electrodes were annealed for 1 hour at 450 ^{o}C.

Solutions of glucose were prepared in 1M KCl, pH 8.3 borate buffer at different concentrations (0mM, 1mM, 5mM, 7.5mM, 10mM, 25mm, 50mM, 75mM, 100mM, 250mM, 500mM, 1000mM, 2000mM). All solutions were purged with N_2 during the experiment. Photoelectrochemical measurements were performed at room temperature, a single cell was use and the three electrodes were in the same solution; the reference electrode was a saturated Ag/AgKCl electrode and the counter electrode used in the experiment was a platinum wire. The potentiostat use for the measurements was a CHI1200A. A 375 nm light emitting diode (ThorLabs, LEDD1B) was used to illuminate the sample and a frequency generator was used to chop the light on and off every 5 seconds (~100 mHz chopping frequency). The current versus time (chronoamperometry) was measured for each concentration at different voltages (0.2V to −0.5V) and light intensities.

Results and Discussion:

This experiment was performed to resolve whether glucose is oxidized via an indirect mechanism, by $OH^{\bullet}$ radicals, or via a direct mechanism, in which the glucose will react directly with photogenerated holes. Figure 2 shows a chopped linear sweep voltammogram of P25 nanoparticles dispersed on ITO in blank electrolyte. The photocurrent onset potential occurs at

approximately -0.6 V and steadily increases with increasingly positive potentials. We then measured the photocurrent versus potential at 5 different light intensities varied over an order of magnitude and 11 different glucose concentrations.

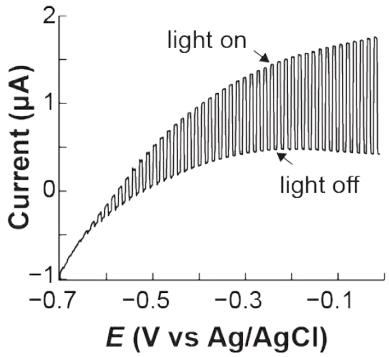

Figure 2. Current vs Potential, chopped light under monochromatic illumination at 375nm. An increase of current is observed at positive potentials.

Figure 3 shows a sub-set of this three-dimensional data: the red circles in each panel represent photocurrent versus light intensity at different applied potentials at a fixed glucose concentration. The photocurrent is linearly proportional to the incident power (blue lines represent linear fits to the data with R^2 values > 0.95), in agreement with Salvador and co-workers[1].

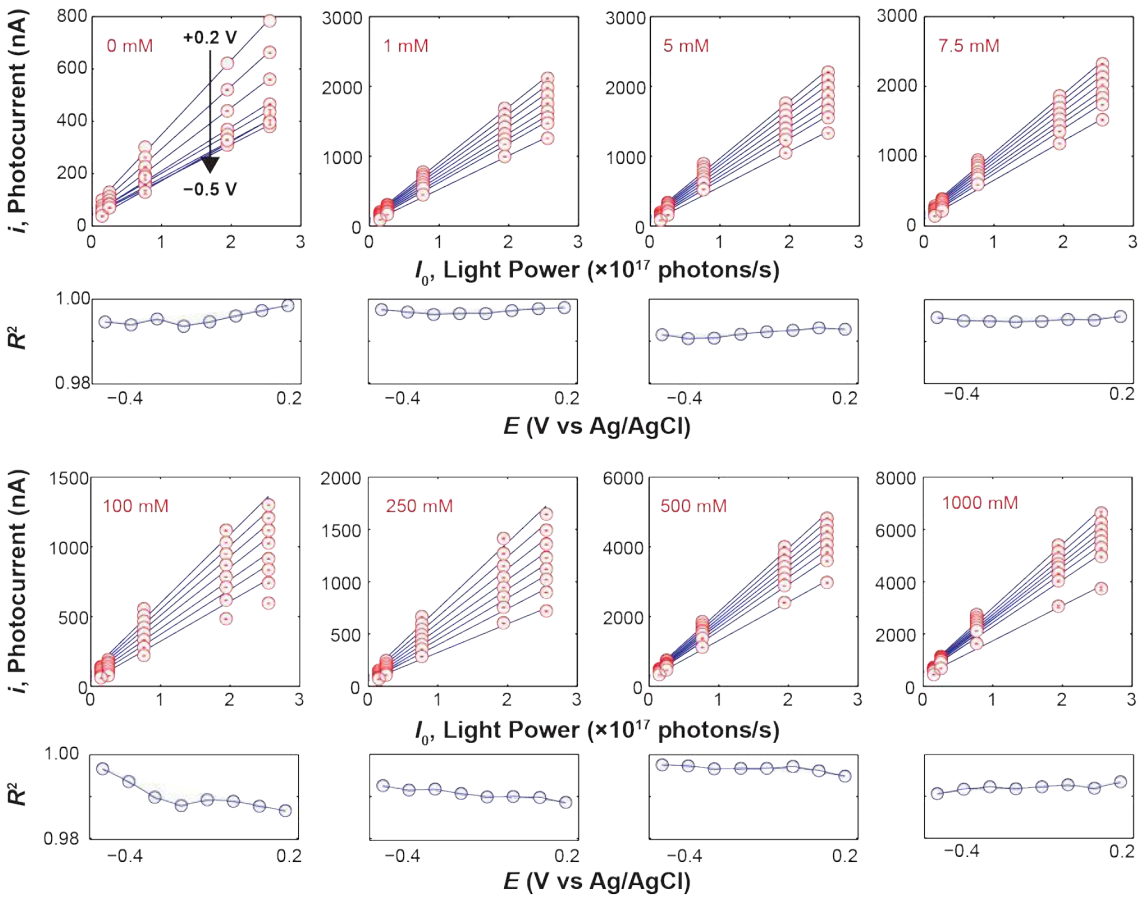

Figure 3. Photocurrent versus light intensity plots. An increase in Photocurrent is observed as the light intensity power in a linear behavior. Also at positive potentials the photocurrent increases and the linearity of the fit reports higher R^2 values.

Figure 4 shows a sub-set of the three dimensional data, similar to figure 3, in which the photocurrent versus glucose concentration at different light intensities and fixed potential (0 mV). A saturation behavior is observed at low glucose concentrations (figure 4a); in agreement with Salvador's work with methanol and formic and acid[1], but at higher concentrations there is a decrease in photocurrent. Following Salvador and co-workers, we fit the initial slope of photocurrent versus glucose concentration (Figure 4a) and plot this slope versus light intensity in Figure 5. Figure 5 shows that the slope (m) is linearly proportional to light intensity, which according to Salvador and co-workers, indicates that glucose oxidation follows a direct mechanism in which the hole interacts directly with the organic molecule. Figure 5 also shows the goodness of fit from the slope versus light intensity data fitting greater than 0.99. Aside from proving that glucose follows a direct mechanism, we also show that the mechanism holds over a wide range of potentials, whereas Salvador's original work was performed at fixed positive potentials.

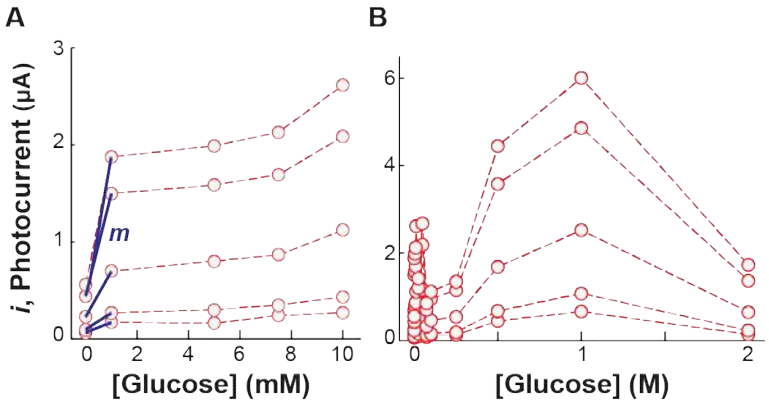

Figure 4. Photocurrent vs glucose concentration at different light powers. We fit the initial slope of photocurrent versus concentration.

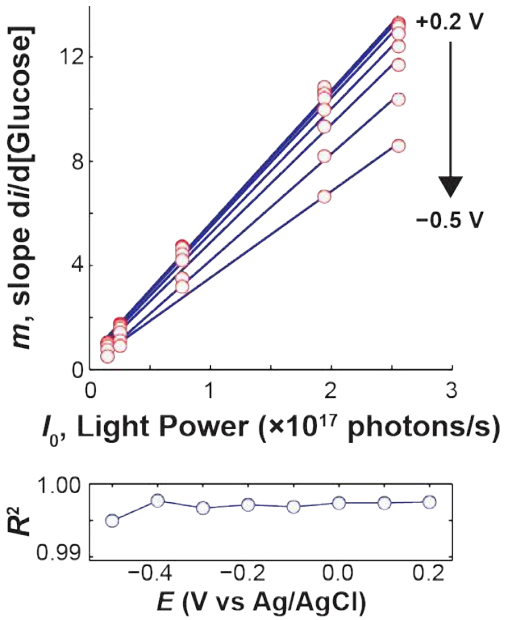

Figures 5. Plot the slope (m) versus light intensity. The slope is linearly proportional to light intensity, which according to Salvador and co-workers, indicates that glucose oxidation follows a direct mechanism. The R^2 plots the goodness of fit vs potential and gives a linearity of over 0.99.

Conclusion:

Photoelectrochemical oxidation of organic molecules dissolved in water represents a useful approach to clean waste water, but the oxidation mechanism is generally unknown. We studied glucose oxidation by TiO_2 nanoparticle electrodes as a function of light intensity, applied potential and glucose concentration. By examining the initial slope in photocurrent increase versus glucose concentration at different light intensities, we conclude that glucose oxidation follows the direct mechanism, as proposed by Salvador and co-workers. Further work is still needed to gather more data points at low glucose concentration.

References:

[1] Lana Villareal, T.; Gómez, R.; Neumann-Spallart, M.; Alonso-Vante N.; Salvador P., Semiconductor Photooxidation of Pollutants Dissolved in Watr: A kinetic Model for Distinguishing between Direct and indirect Interfacial Hole Transfer. I. photoelectrochemical Experiments with polycrystalline Anatase Electrodes under Current Doubling and Anatase of Recombination. *J. Phys. Chem B 2004, 108.*

[2] Frank, S. N.; Bard, A. J., Semiconductor Electrodes. 12. Photoassisted Oxidations and Photoelectrosynthesis at Polycrystalline Titanium Dioxide Electrodes. *Journal of the American Chemical Society* **1977**, *99*, 4667-4675.

[3] St. John, M.; Furgala, Alan.; Sammells, A. Hydrogenation by Photocatalytic Oxidation of Glucose by Platinized n-TiO_2 Powder. *J. Phys. Chem* **1983,** 87, 801-805.

[4] Hoffmann, M. R.; Martin, S. T.; Choi, W.; Bahnemann, D. W., Environmental Applications of Semiconductor Photocatalysis. *Chemical Reviews* **1995**, *95*, 69-96.

[5] Meng, N.; K.H. Leung, M.; Y.C. Leung, D.; Sumathy K,. A review and recent developments in photocatalytic water-plitting using TiO2 for hydrogen production. *Renew Sust Energ Rev* **2007,** 401-425.

Understanding the Role of Cell Signaling in the Proliferation of Dictyostelium discoideum

Brendan Rappazzo[1], and Carl Franck[2]

[1]Department of Bioengineering, University of Maryland, College Park, MD 20740
[2]Laboratory of Atomic and Solid State Physics, Cornell University, Ithaca, NY 14853

Fundamentally, there is a great deal yet to understand about why cells proliferate. Specifically how they influence one another via signaling schemes to encourage growth. Many cells exhibit a growth phenomenon called lag-log phase growth. In which, when first introduced to new media the cells will grow slowly (the lag phase), then at some critical density or point in time they will switch to exponential growth, (the log phase). A better understanding of this behavior could have many applications to fundamental biology and medicine. In order to better research this transition and apply theories of possible signaling schemes, it is helpful to have an apparatus, which without disturbing the sample, can give both a live time cell count number and a distribution of cell sizes. The organism measured by this machine is *Dictyostelium discoideum*. The machine (the Snowflake Apparatus) initially provided an accurate cell count but not an accurate size distribution. It was modified optically and the collected data was reviewed to better understand how by setting proper threshold parameters, a better signal to noise ratio could be achieved. With the new techniques applied the same accurate cell growth curve was observed but now with an interesting cell size distribution plot. The plot seems to show a shift from small cells to bigger cells, which may potentially be clusters. The accuracy of the machine to distinguish sizes needs to be confirmed in future studies, but this preliminary improvement reveals that cells forming clusters may be an integral process for cells switching to exponential growth. This improved apparatus can be confirmed to be reading cell clusters by introducing a chemical to break apart the clusters and then by observing the distribution shift back to smaller cell sizes. The apparatus could then be an important component in research examining theories of cell proliferation.

I. INTRODUCTION

The proliferation of cells is a fundamental aspect of cell biology, yet a non-invasive method that can report live data for cells grown in suspension does not exist. The current methods of measuring cell growth often involves removing some of the biomass, not only making the sample prone to infection, but also jeopardizing the natural growth cycle of the cells.[1] The development of a non-invasive cell counter would greatly improve the way cells growth curves could be measured and lend for a much better understanding of how cells proliferate. Specifically, it could lead to insights in the lag-log transitions of cell proliferation. When cells are first introduced into a new environment, they will at first grow slowly, it is only when a certain critical density is reached that they will transition into exponential growth.[2] *Dictyostelium discoideum,* a NIH model organism, is an ameboid protozoan and provides an ideal test subject to study the transition from lag phase to log phase.[3] However, current methods show a great variation in the growth curve of *D. discoideum,* both in the lag and log phases. This

variation makes it difficult to apply theory to cell proliferation because the data points are sparse.[4]

The purpose of this study was to improve and calibrate a light scattering system that measures cell density in live time. Additionally to use this system to better understand the lag-log transition of *D. discoideum*. This behavior has also been observed in tumor growth and may lead to a better understanding of the mechanisms responsible for this phenomenon.[5]

II. MATERIALS AND METHODS

The collection and processing of data for this project was done in two separate parts. The collection was done by what is called the "Snowflake Apparatus." The reason for this name is that in principle it works the same way one's headlights do on a snowy night. Normally only the path in front of the car is illuminated, but when a snowflake crosses the path of the headlights it reflects light back, and the driver in principle could count the snowflake as it passes by. Similarly the Snowflake apparatus shines a laser into a suspended culture of *D. discoideum* and when a cell crosses the light it counts the event. Specifically it turns the count into an electrical pulse with the two key parameters; pulse width and pulse height. Pulse height simply being how bright the particle or cell is while pulse width is how long the particle stays in the view frame of the detector. Both of these have biological meaning which will be discussed later. The complete arrangement of the apparatus is a laser shown through a focusing lens which then passes through the suspension sample in a test tube. The test tube also contains a magnetic stir bar to keep the system well mixed throughout the testing. Then in a forward scattering position another lens is placed to magnify the signal. The lens used is from a DSLR camera. The magnified signal is then collected by the detector. The signal is sent to a computer which is running *Pulse Recorder and Analyser* (PRA) which was programmed by Dr. Dolleiser of the University of Sydney.[6] The program processes and collects pulses utilizing the computer's on-board sound card. The speed at which the Snowflake Apparatus collects data is well within the speed at which PRA can collect data. With PRA a pulse height threshold parameter is used to try and filter out lower level noise. The signals are collected at ten minute intervals and every ten minutes a file is created which stores the data of each pulse.

From PRA a binary file is created with the file type .pls. This binary file is then used by an R computer program. The program uses a control file, which should provide a background of the sample when no cells or particles have been added. The program then reads in the test files and looks at every pulse and collects the ones that meet user defined parameters for upper and lower limits on pulse height and pulse width. After going through all of the pulses in a single file it builds histogram data for the test file and subtracts from it the control data. It then plots both the pulse height distribution and pulse width distribution for the individual file. Then it updates a global variable to store the total number of counted pulses and adds a column to a global matrix which stores the normalized pulse height distribution. The former is used to plot the growth curve when all of the files have been analyzed and the latter is used to show how the height distribution develops in time. Both of these plots are created once the program has gone through all of the test files. The program can be modified to not do a background subtraction, which sometimes is beneficial to see the raw signal.

III. RESULTS AND DISCUSSION

The original setup of the apparatus was used to produce a growth curve. This yielded a growth curve that appeared to have the lag-log transition. From further examination of a semi log plot the transition was evident. However, when the distribution of pulse height was plotted versus time there was no apparent distribution transition.

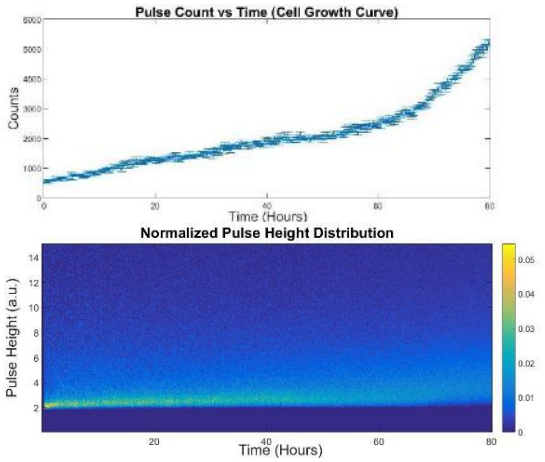

Figure 1: Pictured top is the counted pulse versus the time in hours with error bars. Although a small transition can be seen, it is not obvious. Pictured bottom is the pulse height distribution of that same run, plotted versus time. The pulse height distribution does not appear to change throughout the run, despite the increase in cell number and cell growth curve.

That is until the PRA system itself became saturated with pulses. Because of this perceived lack of ability for the apparatus to resolve cell size it was deemed necessary to alter the optics of the apparatus in such a way that would yield the highest resolution possible. To do this several different configurations of the optics were tried. First, a scattering angle of 90 degrees was picked, this angle is desirable because it eliminates the most noise being detected. However, it also makes the incoming signal significantly weaker, so it is more difficult to filter out the counts and get a consistent cell growth curve. When tested the growth curve did not show any kind of regular shape, and the measurements, even within hour ranges, varied extremely. The consistency and strength of the signal was determined by looking at the counts versus time as well as by observing the pulses on an oscilloscope.

Because of the poor results from all configurations that were not forward scattering, a sharp forward scattering configuration was picked as the optical setup. For one it provided by eye, high amplitude pulses that were distinguishable from the noise. Additionally the counts at close time ranges were statistically consistent with one another. To better improve the data that could be extracted from the machine, cuts on the pulse width were considered. The motivation behind the idea was the following. Within the sample being examined, there are cells as well as many other particles, whether it be cell debris or just normal dust. The machine is going to read in both cell signals and this noise signal as long as they meet a certain brightness threshold. Now for the cells the interpretation for seeing a brighter or higher in amplitude pulse simply means the cell is bigger. But these extra dust particles are presumably made of a different material and could generate a signal above the set threshold despite being much smaller or bigger. So the issue becomes how can the machine be better targeted to pick out just cell signals? In the post processing of the signal it is trivial to isolate signals of a certain range of both pulse height and pulse width. So the idea was to run a sample of 10 micron diameter colloids in distilled water in the system, then use, by trial and error, cuts on the pulse width that would provide the best resolution (narrowest peak in the pulse height distribution) for the colloids. The colloids were used as a control in this case for two main reasons. First is that they have a very precise size so they provide the best testing ground for the machine to resolve size. It is known that in reality the size distribution would be a very tall and narrow peak and one can use cuts to try and replicate that peak as best as possible. Secondly, the colloids are a similar size to the cells that will be analyzed, so it can be assumed they will mix through the system in a similar manner. This is important because the pulse width's physical meaning is simply how long the particle stays in the view of the detector. This to a large extent is determined by the hydrodynamics of the system, in this case meaning the mixing generated by the stir bar. So because of their similar size it is assumed that the colloids and cells will mix similarly in the solution. That on average they should

spend roughly the same time in the view of the detector, meaning that they will share the same range of pulse widths. It can be imagined that a different sized particle, say smaller, would have a higher velocity and would thus occupy a lower pulse width range.

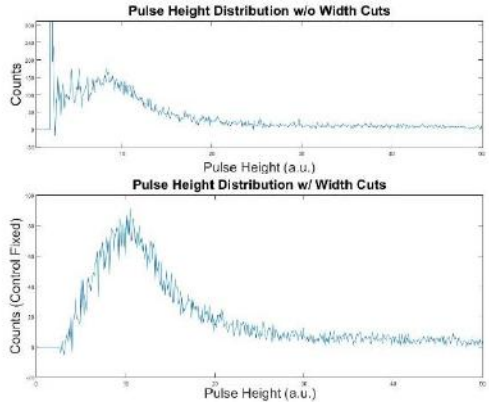

Figure 2: Pictured top is the resulting pulse height distribution when all pulse widths are considered for 10 micron diameter colloids. Both images are finely binned histograms of pulse heights. Pictured bottom is the same colloids run's pulse height distribution but with width cuts.

So by changing the optics to get a better magnification of the sample and to improve the scattering angle to get a stronger signal the machine was given the best positioning to collect the most reliable data. Then by thinking about the problem and using colloids it was possible to select portions of the data where it was believed a true cell signal should be coming from. With these new tools, another low density cell sample was run. The results exhibited the same cell growth curve which again demonstrated a lag-log transition. Most importantly though, on a normalized heat map distribution, it showed a shift from the lower perceived cell sizes to larger cell sizes and potentially clusters.

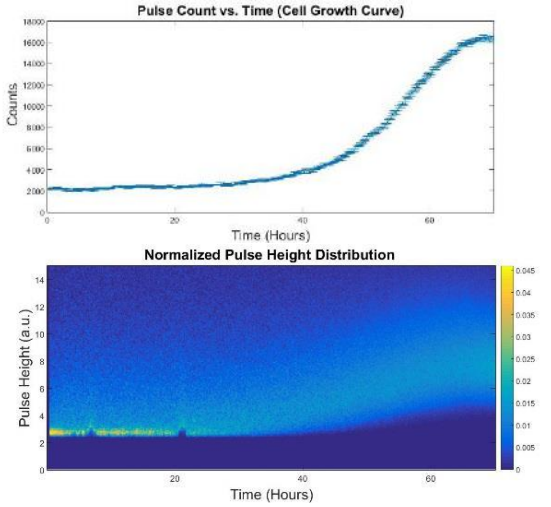

Figure 3: Pictured top is pulse counts versus time starting on a low density cell sample, with the new optics and width cuts. Here a transition from linear to exponential growth can be seen. Pictured bottom is the pulse height distribution for the same run. Here a shift to a higher pulse height distribution can be seen.

The reason it is thought that clusters appear is because there is a complete departure from the small cell sizes in the distribution in the log phase. Moreover this shift of the distribution to larger cell sizes occurs at the same time as the shift from the lag to log phase. This provides an exciting view into what might actually cause the cells to shift from their slow lag phase growth to the exponential log phase growth. This possibility is deserving of future exploration.

IV. CONCLUSION AND FUTURE DIRECTIONS

In a fundamental way not much is currently understood about the specific mechanisms which trigger cell proliferation. Currently a non-invasive apparatus that can measure live time cell growth curves does not exist. The creation of such a machine could give important insights regarding when cells enter the exponential growth phase, which may allow for specific investigations into the cell signaling mechanisms responsible for this. This paper provides a brief overview of the efforts used to

improve the design and calibrate a light scattering/imaging apparatus that provides live data. It appears the effort was a success as not only is the lag log transitions of cell growth clearly expressed in the cell counting mechanism of the machine, but additionally the machine appears to be resolving a change in cell size. This success is a result of the alteration of the optics utilized as well as a method introduced to selectively make cuts on the data to get a better signal to noise ratio.

Moreover this change in cell size seems to happen at the same time that the transition to exponential growth occurs. Additionally the distribution shift is completely away from the small cell region which potentially indicates that the cells are forming clusters. The further exploration of this idea could confirm the idea that faster growth happens when cells form clusters and excrete a growth signal.

Moving forward the machine could be improved by introducing a signal amplifier. This is suggested because it appears that the lower end of the cellular size distribution is being cut off by PRA's set threshold. While below the threshold it is very hard to distinguish between actual signal and noise. So in order to better isolate the signal from noise, especially on the lower end, an amplifier could be introduced. This would give a clearer view into the size fluctuations throughout growth. Furthermore to test the cluster theory a chemical called EDTA could be introduced to the suspension while the cells appear to be in clusters. The EDTA is an agent which destroys cell to cell adhesion and would cause the cells to fall apart if they were in clusters. What that means for the machine is that if cells size is really being observed, and they are in clusters, when the EDTA is introduced the distribution would be shifted back to smaller cell sizes. This simple experiment would reveal two major aspects for this work if successful. First that the machine is indeed resolving cell size and that the transition of cell growth is heavily reliant on the forming of clusters.

V. ACKNOWLEDGEMENT

This work was supported by the Cornell Center for Materials Research with funding from the Research Experience for Undergraduates program (DMR-1063059 and DMR-1120296). I would like to thank Carl Franck for being my mentor this summer and for all the great coffee.

---

[1]Mustafa, Natali R., Ward De Winter, Frank Van Iren, and Robert Verpoorte. "Initiation, Growth and Cryopreservation of Plant Cell Suspension Cultures." Nat Protoc Nature Protocols 6.6 (2011): 715-42. Web.

[2]Torrey, John G., Jakob Reinert, and Nancy Merkel. "Mitosis in Suspension Cultures of Higher Plant Cells in a Synthetic Medium." American Journal of Botany 49.4 (1962): 420-25. Print.

[3]Chisholm RL, Gaudet P, Just EM, Pilcher KE, Fey P, Merchant SN, Kibbe WA. (2006). dictyBase, the model organism database for Dictyostelium discoideum. Nucleic Acids Res. 34 (Database issue): D423-7.

[4]Franck, Carl, Wui Ip, Albert Bae, Nathan Franck, Elijah Bogart, and Thanhbinh Thi Le. "Contact-mediated Cell-assisted Cell Proliferation in a Model Eukaryotic Single-cell Organism: An Explanation for the Lag Phase in Shaken Cell Culture." Physical Review E 77.4 (2008): n. pag. Web

[5]Zhang, Ming, Chandra Das, and Hernan Vasquez. "Predicting Tumor Cell Repopulation After Response: Mathematical Modeling of Cancer Cell Growth." Anticancer Research 26 (2006): 2933-936. Web.

[6]http://www.physics.usyd.edu.au/~marek/pra/index.html

Transport Study of Redox Active TMPD Through Alkaline Anion Exchange Membrane Ionomer Films

Ana Estefanía Rivera, Johary Rivera-Meléndez, and Héctor D. Abruña*

Department of Chemistry, University of Puerto Rico, Rio Piedras Campus, San Juan, PR

Department of Chemistry and Chemical Biology, Cornell University, Ithaca, New York 14853-1301, United States

Introduction

Increasing energy demands, due to the growing global population, have increased the need for alternative energy sources. Currently, the majority of energy is derived from fossil fuels, which has brought us to environmental catastrophe.[1] An attractive alternative energy conversion device is fuel cells which convert chemical energy of H_2 directly into electrical energy.[2] Fuel cells can be characterized into five mayor types depending on the electrolyte: alkaline, proton-exchange membrane, solid oxide, phosphoric acid and molten carbonate.[3]

Alkaline fuel cells offer distinct advantages, such as the higher oxygen reduction reaction kinetics, which enhances its performance. This, in term, enables the use of less noble metal catalyst, lowering cost.[3] One of the main drawbacks of alkaline fuel cells is the precipitation of metal carbonates produced by the interaction of the alkaline electrolyte with the CO_2 in the air and mobile cations such as K^+. In essence, CO_2 in the air is converted to CO_3^{2-}, and upon subsequent reaction with K^+ forms K_2CO_3 which precipitates.[3] This reaction consumes hydroxide anions, which lowers the conductivity of the electrolyte. In addition, the precipitated salt restricts access and transpot to the electrode surface. To address these issues, a solid polymer electrolyte can be employed in place of the liquid electrolyte.[3]

In an alkaline fuel cell, the polymer membrane works as a barrier between the anode and cathode as well as an ion-conducting medium that facilitates the transfer of hydroxide from the cathode to the anode.[2] An alkaline anion exchange membrane (AAEM) has the cationic sites covalently immobilized in the polymer backbone. Therefore, there will be some carbonate formation due to the reaction of the hydroxide and carbon dioxide, but because there are no mobile cations, salt precipitation is precluded.[3]

An ideal AAEM should have great mechanical stability, high base stability and good hydroxide ion conductivity.[4] Herein, a tetrakis(dialkylamino)phosphonium cations affixed to a polyethylene backbone AAEM,

used to study the transport of redox active molecules.[4] Previous ex-situ characterization of this material has demonstrated it has mechanical and base stability and its solvent processable. By using different solvents, n-propanol or methanol, we can obtain either a soluble ionomer solution or a solid membrane, respectively. Having the same material in these two different forms allows the material to be used in catalyst-ionomer inks for fuel cell electrode assembly preparation.[4] Furthermore, the soluble ionomer solution can be used to conduct electrochemical studies, such as the transport of redox active molecules through the ionomer film itself. As a redox active probe we employed N,N,N′,N′-tetramethyl-p-phenylenediamine (TMPD), which exhibits two reversible one-electron processes at 0.1 and 0.4 V (vs Ag/AgCl). Rotating disk electrode (RDE) voltammetry was used to achieve a better understanding of the physical transport processes of these ionomer films.

Materials and Methods

Materials

Sodium hydroxide (NaOH, 99.0%) and sodium carbonate ($NaCO_3$, 99.0%) for the ion exchange process, were purchased from Sigma-Aldrich. N,N,N’,N′-tetramethyl-p-phenylenediamine (TMPD, Aldrich, 99.0%), n-propanol (Aldrich), and sodium chloride (NaCl, Macron, 98.0%) were used as recieved. All solutions were prepared using high purity deionized water (18 MΩ cm Barnstead Nanopure Model No. 7148). For deaerating the solutions, high purity nitrogen and argon gases were purchased from Airgas.

Ion exchange and ionomer solution

The phosphonium-functionalized solid polymer (chloride form) was placed in a beaker with a stir a bar. The polymer was submerged in 1.0 M NaOH for 20 minutes with constant stirring. After 20 minutes, the solution was replaced with fresh solution. The procedure was repeated a total of three times. To remove all traces of NaOH, the polymer, now in the hydroxide form, was rinsed with nanopure water following the same procedure as above. Since exposing the polymer, in the hydroxide form, to the carbon dioxide in air will cause carbonation of the polymer, for storage purposes the hydroxide was replaced with carbonate. Thus, the latter procedure was repeated with 1.0 M Na_2CO_3. After being rinsed with nanopure water, the polymer was left to dry overnight in a vacuum oven.

The ionomer solution was prepared by dissolving the polymer in 2-propanol with constant stirring at 60 ^{o}C for three hours. Finally, the solution was filtered using glass wool.

Preparation of solutions

Solutions were made maintaining a constant concentration of TMPD of 1.0 mM while varying the concentration of the electrolyte. The concentrations of NaCl used were 0.1, 0.5, and 1M.

Membrane deposition

Glassy carbon electrodes (3mm) were modified via drop casting using an aliquot of 2.0 µL of the ionomer solution. It was left standing until dry. For the RDE glassy carbon electrode (5mm), the RDE set up was turned upside down. 10µL of the ionomer solution were deposited on the electrode surface and left rotating at 500 RPM for 4 minutes. Before use, the modified electrodes were soaked in 1.0 M NaOH solution for an hour. A profilometer was used to determine the membrane thickness, which was of the order of 250 nm.

Cyclic Voltammetry

Electrochemical experiments were conducted in a standard three-electrode cell configuration with a glassy carbon working electrode, Ag/AgCl reference electrode and a Pt counter electrode. The working electrodes were polished using 1.0 µm, 0.3 µm, and 0.1µm alumina slurry, and then sonicated in acetone prior to film deposition. Cyclic voltammetry was performed using a CV-27 potentiostat and a homemade software developed under Labview®.

Determination of diffusion coefficients

RDE is a technique where the working electrode is rotated to induce a flux of analyte to the electrode. By varying the rotation rate one can study the diffusion of redox active molecules through the ionomer film. Using the mass transport limited current and the Levich equation, we can obtain the diffusion coefficient, which tells us the rate at which electroactive molecules arrive at the electrode surface.

Results and discussion

The cyclic voltammetric response for TMPD at the modified electrode, with 0.1 M concentration of supporting electrolyte, showed a significantly higher degree of irreversibility when compared to the response at the bare glassy carbon electrode. When comparing the anodic and cathodic currents, a smaller cathodic peak current was evident. A potential explanation is that $TMPD^{+}$ is electrostatically repelled by the cationic sites in the polymer backbone. However, when the concentration of the supporting electrolyte is increased to 1.0 M,

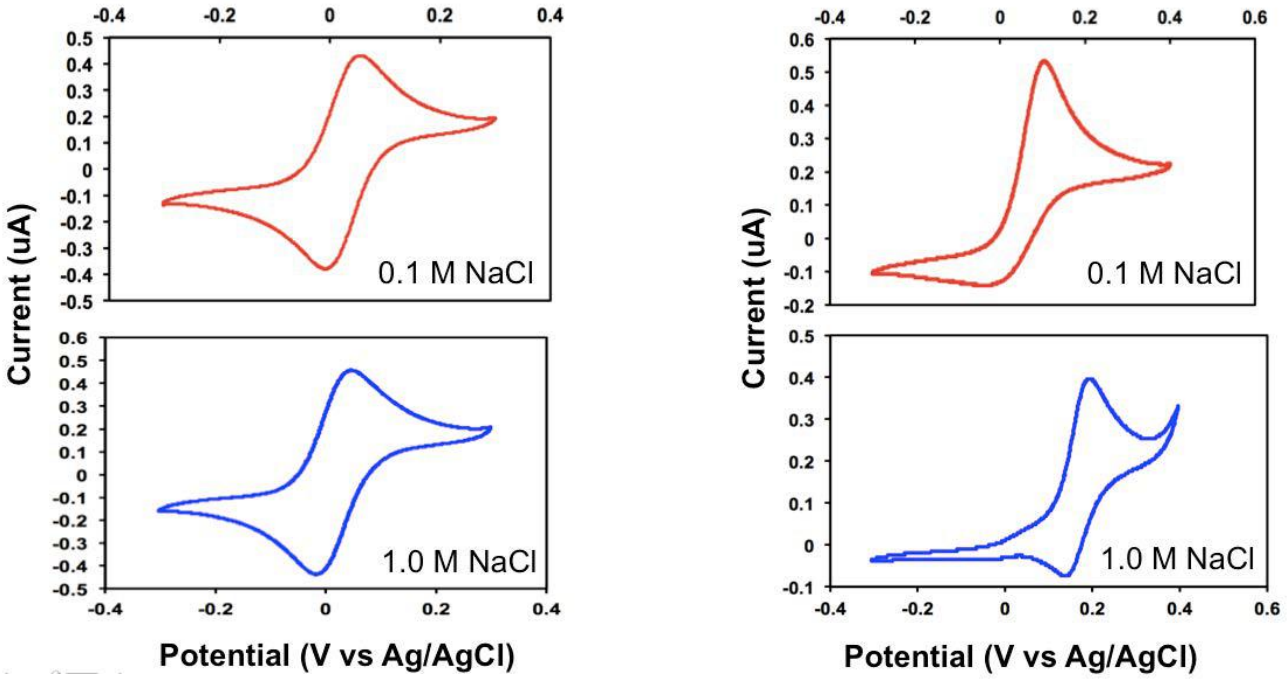

Figure 1: Cyclic voltammetry of 1 mM TMPD in NaCl supporting electrolyte (a) 3 mm bare electrode and (b) 250 nm film ionomer modified glassy carbon electrode at a scan rate of 20 mV/s.

the cathodic peak reappears. We believe this arises as a result of the decrease of the Debye length, making it easier to screen the charges.

RDE voltammograms showed a decrease in diffusion coefficient from the bare electrode to the ionomer film modified electrode. See Figure 2 and 3. A tenable explanation could be the shielding effect of the ionomer film to the electrode surface or the interaction of TMPD with the cationic site of the ionomer film. Moreover, when we increased the concentration of the supporting electrolyte, the diffusion rate of the TMPD decreased. (See Table 1). Preliminarily, this is attributed to the increase in viscosity of the solution.

Conclusion

In conclusion, the redox reaction of TMPD at an ionomer film modified electrode showed a significantly higher degree of irreversibility vis-á-vis the bare electrode. Repulsive interactions by the fixed cationic groups are likely responsible. The RDE and the cyclic voltammetric studies employing the redox probe molecule of TMPD were important in gaining an understanding of the functional and transport aspects of ionomer materials.

Table 1: Diffusion coefficients obtained using the Levich equation.

	$D_{o\ (Bare)}$ (cm^2/s)	$D_{o\ (modified)}$ (cm^2/s)
0.1 M NaCl	2.4×10^{-6}	1.7×10^{-6}
0.5 M NaCl	1.9×10^{-6}	1.1×10^{-6}

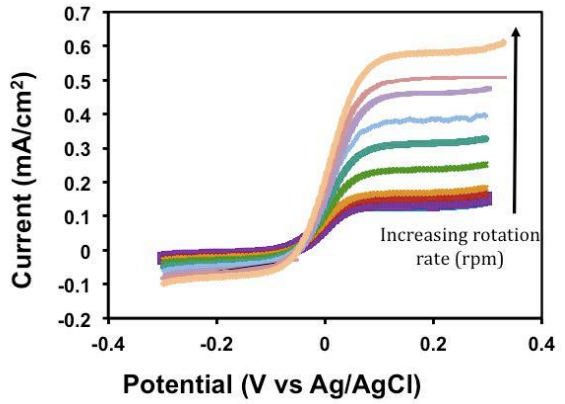

Figure 2: RDE of 1mM TMPD in 0.1 M NaCl at the bare glassy carbon electrode at 10 mV/s.

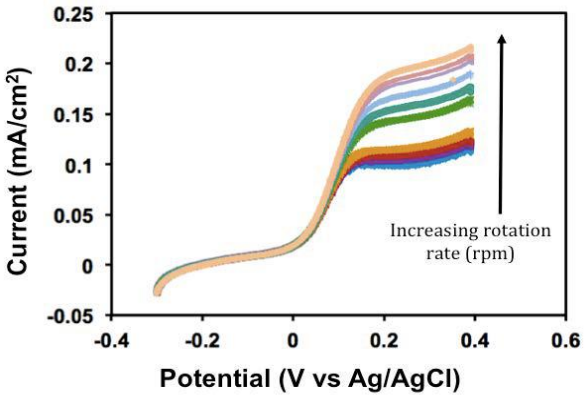

Figure 3: RDE of 1mM TMPD in 0.1 M NaCl at the 250 nm film ionomer modified glassy carbon electrode at 10 mV/s.

Acknowledgements

This work was supported [optional: in part] by the Cornell Center for Materials Research with funding from the NSF MRSEC program (DMR-1120296).

References

(1) Abruña, H.D., *J. Chem. Educ.* **2013**, *90*, 1411−1413

(2) Kostali IV, H. A.; Clark, T. J.; Robertson, N. J.; Mutolo, P. F.; Longo, J. M.; Abruña, H. D. *Macromolecules* **2010**, *43*, 7147-7150.

(3) G.Merle, et al., Anion exchange membranes for alkaline fuel cells: A review, *J. Membr. Sci.* (2011), doi: 10.1016/j.memsci.2011.04.043

(4) Noonan, K. J. T.,Hugar, K. M., Kostalik IV, H. A., Lobkovsky, E. B., Abruña, H. D., Coates, G. W., *J. Am. Chem. Soc.* 2012, 134, 18161−18164.

Fabrication of surface functional nanofiber membranes for use as biosensors

Laura Saunders, Edurne Gonzalez, Larissa Shepherd and Margaret Frey
Department of Fiber Science and Apparel Design, Cornell University, Ithaca, New York 14853-1301, USA

Introduction

Electrospinning is a well-established technique widely used to form non-woven nanofibers with diameter ranging from 10 micrometers to 10 nanometers.[1] The main advantage of electrospinning, compared to other techniques used to create nanofibers, is that it is both inexpensive and simple. Electrospun nanofibers are attractive candidates for their use as biosensors due to their high porosity and high surface area to volume ratio that provides a large contact area for reaction between the sensing material and the analyte. When constructing a biosensor, two important concepts must be taken into account; first, the sensing substrate, in our case the nanofiber, needs to be able to interact with biological molecules. Secondly, as most of biological samples are aqueous, nanofibers must be hydrophilic in order to enhance the contact between the detection site and the analyte, but also they have to be non-water-soluble, to avoid their degradation in the aqueous phase. The higher the wettability of the nanofiber, the greater the improvement in the material's function as a biosensor.[2] Surface wetting is also a significant factor in material biocompatibility.[3]

Poly(lactic acid) (PLA) is a popular choice for electrospinning, as it is easily spun and is compatible with biological systems.[2] Streptavidin-biotin assembly has been used extensively for the creation of biosensors.[4,5] Li et al. were able to successfully incorporate biotin up to 18 weight total percent (wt %) into PLA nanofibers.[6,7] They showed that the fibers retained the smooth morphology once biotin had been incorporated.[7] Importantly, they showed that biotin was available at the surface of the PLA fibers. They also showed that streptavidin immobilized on the membrane surface could capture biotinylated antibodies.[6]

However, PLA is a highly hydrophobic polymer, making the wettability of the PLA-biotin complex membrane difficult. To increase the hydrophilicity of the polymer, Poly(ethylene glycol) (PEG) can be added to PLA.[8-10] PEG is a biocompatible and highly hydrophilic polymer. A blend of PLA homopolymer and PLA-*b*-PEG block polymer nanofibers exhibit increased surface wettability in water.[9,10] Researchers in our group have demonstrated that the optimum ratio of PLA-b-PEG to produce non-water-soluble nanofabrics with the maximum ability to absorb water to be at 12 wt% PEG. The optimum block length was found to be PLA(1000)-*b*-PEG(5000).[9] At this ratio and block length, wettability was at a maximum.

This work is a combination of the previous ones; biotin has been incorporated into PLA fibers (up to 18 wt %) but, in this case, PLA-*b*-PEG block polymer were also used as additives to increase the hydrophilicity to the final fiber. Thus, the effect of the presence of PLA-*b*-PEG block polymers in the phase separation of biotin to the fiber surface was studied.

Fibers obtained in this work were functional, hydrophilic and non-water-soluble, desirable features for a potential biosensor.

Materials and Method

Materials

Needle Deflect point 20g × 3.2 in. was purchased from Fisher Scientific Company. Copolymers PLA(730)-*b*-PEG(5000) were synthesized by ring opening polymerization of lactide (Sigma-Aldrich) in the presence of poly(ethylene glycol) methyl ether (Mn: 5000 g/mol, Sigma-Aldrich), using stannous octoate (Sigma-Aldrich) as catalyst. 99.8% Anhydrous N,N-dimethylformamide (DMF), Phosphate buffered saline (PBS) and Tween 20 were all purchased from Sigma-Aldrich. PLA 4043D (MW 5 153,315 g/mol, PDI 5 1.81) was purchased from NatureWorks. Pierce™ Biotin HABA/Avidin Quantitation Kit was purchased from ThermoScientific.

Preparation of Electrospinning Solutions

In this work, two different electrospinning solutions were prepared; some containing high molecular weight PLA and varying weight percentages of biotin, and others containing high molecular weight PLA, PLA(730)-*b*-PEG(5000) block copolymers and varying weight percentages of biotin. The solvent used was DMF. All initial solutions contained a total of 22 wt % of PLA and 0, 5, 10 and 18 wt % of biotin with respect to the total amount of polymer. In the case where PLA(730)-*b*-PEG(5000) block copolymers were used, the amount of added block copolymer was adjusted to obtain a final fiber with a composition of 12 wt % of PEG, as per previous work by Buttaro et al.[9] Before electrospinning, we dissolved all the components in DMF with heat until a homogeneous dissolution was obtained (around two hours).

Electrospinning

The same electrospinning set up and procedure as the ones previously reported by Buttaro et al.[9] were used in this work. A voltage supply (Gamma high Voltage Research) was used to apply 15 kV to the needle and a grounded copper collector was placed 10 cm away from the needle tip. The solution feed rate was maintained at 10 µL/min using a programmable PHS Ultrasyringe pump (Harvard Apparatus). During electrospinning, a shielded heating unit preheated to 70 ± 5^{o}C controlled the syringe temperature. A heat gun (Master Appliances Corp.) was used to keep the needle temperature at 70 ± 5^{o}C. The temperature at the needle was verified every 30 minutes using a digital thermometer (Fisher Scientific Company).

Scanning Electron Microscopy (SEM)

SEM imaging was used to study the morphology of the fibers. Samples were left uncoated during imaging. Images were taken at 1 kV voltage using a LEICA 440 SEM. Utilizing ImageJ^{TM} software on the SEM images, average diameters of the fibers were determined. For each sample, 50 measurements were taken from three separate images at 7000x-10000x magnification.

Colorimetric assay

A colorimetric assay was performed to quantify the amount of surface available biotin on the fibers.[6] The method measures change in absorbance at 500 nm as avidin is removed from a 4'-hydroxyazobenzene-2-carboxylic acid (HABA) /Avidin solution, i.e. bound to the biotin at the fiber surface. A Lambda 35 UV/Vis Spectrophotometer from

Perkin Elmer was used. Experiments were performed using a Pierce™ Biotin Quantitation Kit from ThermoScientific. Reconstitution of the HABA/Avidin solution was performed as per the manufacturer protocol. First, the absorbance of the HABA/Avidin solution in PBS Buffer was measured at 500nm. Then, a sample of fiber was placed into the cuvette and shaken for three minutes and the absorbance of the solution was measured again. The absorbance measurement was repeated until the obtained value was stable. The available biotin was calculated using the equation:

$$Available\ Biotin = (A^0{}_{500} - A_{500})\left(\frac{MW_{Biotin}V}{\varepsilon bW}\right)$$

$A^0{}_{500}$: Absorbance of the solution prior to the addition of nanofiber
A_{500}: Absorbance of the solution after reaction with nanofiber
MW_{Biotin}: Molecular weight of the Biotin (g/mol)
V: Volume of the solution (mL)
ε: 3.4×10^{10} $(M*cm)^{-1}$
b: Path length (cm)
W: Mass of nanofiber sample (g)

Water resistance

The water resistance test was performed to test the fibers' degradation in water. PLA and PLA/PLA-*b*-PEG fibers with 0 and 18 wt % of biotin were immersed in water. One sample set was immersed for 1 day and the other for 1 week. The fibers were weighed before being immersed and after being removed and dried (overnight in vacuum). Another colorimetric assay was performed on the fibers after being immersed in water to assess the amount of biotin retained by the fiber.

Experimental

Analysis of Fiber Morphology (SEM)

Figures 1 and 2 show SEM images of the PLA and PLA/PLA-*b*-PEG fibers with 0, 5, 10, and 18 wt % of biotin. Fibers containing no PLA-*b*-PEG show a smooth, uniform morphology. No clear trend was observed in the average diameters as the amount of biotin added to the PLA fibers increased (Figure 3). PLA fibers with no biotin had an average diameter of 1.06 ± 0.11 μm while PLA fibers containing 18 wt % of biotin solutions had a diameter of 0.75 ± 0.09 μm (Figure 3). PLA/PLA-*b*-PEG fibers (Figure 2) showed a rougher morphology, especially the samples with 5 and 10 wt % of Biotin. The diameters of these fibers are significantly lower than the ones of the PLA fibers (Figure 3). Again, no clear difference or trend was observed in the fiber diameter with the addition of biotin. PLA/PLA-*b*-PEG fibers with no biotin had a diameter of 0.41 ± 0.11 μm while the fibers containing 18 wt % of biotin had a diameter of 0.32 ± 0.08 μm.

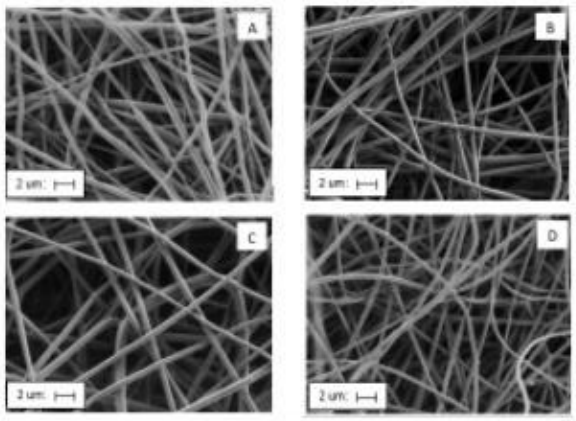

Figure 1. Comparison of SEM images. (A) Pure PLA (B) PLA + 5 wt% Biotin (C) PLA + 10 wt% Biotin (D) PLA + 18 wt% Biotin

In blends of PLA and PEG, PEG has been shown to plasticize the melt; when added to PLA, it lowered the melt viscosity by increasing the free volume.[10]

This effect was evident in the fibers containing PLA-*b*-PEG, as their diameters were significantly lower compared to pure PLA fibers (Figure 3). Similar results were observed by Buttaro et al.[6]

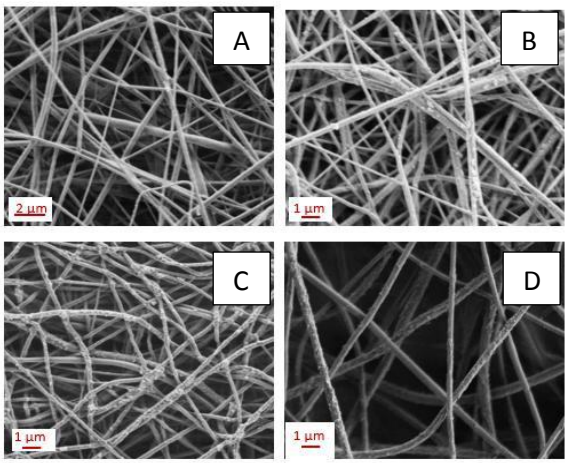

Figure 2. Comparison of SEM images. (A) Pure PLA/PLA-*b*-PEG (B) PLA/PLA-*b*-PEG + 5 wt% Biotin (C) PLA/PLA-*b*-PEG +10 wt% Biotin (D) PLA/PLA-*b*-PEG + 18 wt% Biotin

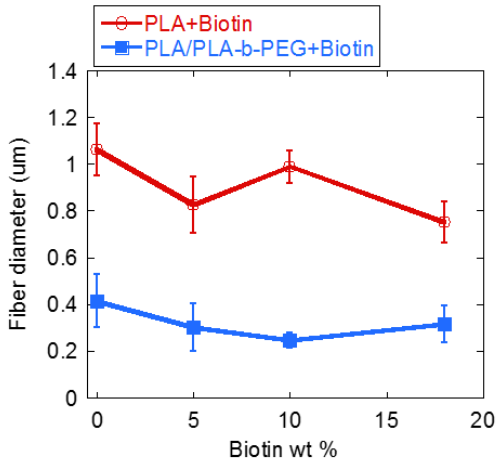

Figure 3. Comparison of fiber diameter versus overall amount of biotin in the fiber

Measurement of Surface Available Biotin

The amount of biotin available at the fiber surface was quantified using a HABA/Avidin colorimetric assay.[6] HABA binds avidin to produce an orange colored complex, which absorbs light at 500 nm. When a fiber mat containing biotin is added to a solution containing HABA/avidin complex, avidin is removed from the complex and binds with the available biotin due to its higher affinity, causing a decrease in the absorbance. Figure 4 shows the drastic color change of the HABA/Avidin complex solution before and after adding the fiber mat.

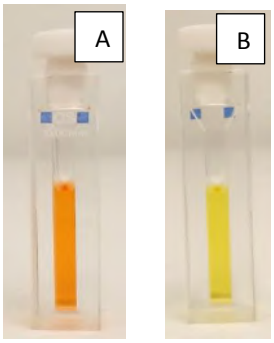

Figure 4. Comparison of the HABA/avidin solution before (A) and after (B) the fiber mat containing biotin is added.

Results of the colorimetric assays are shown in Figure 5. In the case of the PLA fibers, similar results to the ones observed by Li et al.[6] were obtained. No change in the absorbance was observed in the control sample (containing no biotin) indicating that no avidin was removed from the HABA/avidin complex when the control fiber mat was added. The increase of the surface available biotin was not linear regarding the concentration of biotin in the spinning dope. Slight amount of surface available biotin was measured in PLA fibers containing and overall concentration 5 and 10 wt % of biotin (0.75±0.18 mg biotin/g fiber and 0.50±0.05 mg biotin/g fiber respectively). When 18 wt % of biotin was added to the spinning dope, the surface available biotin in the fiber surface jumped to 17.7±5.2 mg biotin/g fiber.

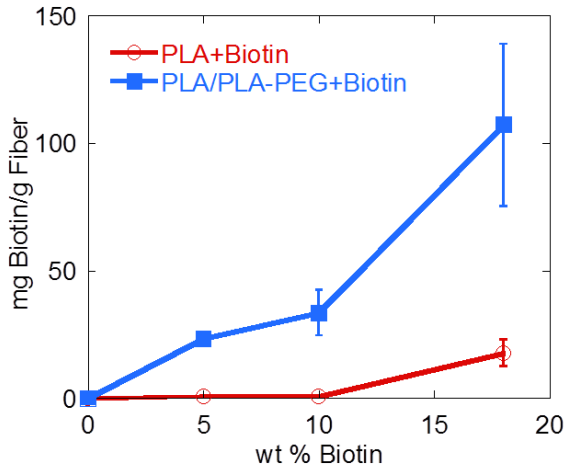

Figure 5. Colorimetry assay results. Surface available biotin is measured in mg Biotin/g fiber and plotted against the overall amount of biotin in the fiber.

In the case of PLA/PLA-*b*-PEG fibers, the surface available biotin was significantly higher than in PLA fibers. Again, non-proportional relation was observed between the overall biotin concentration and the surface available biotin. 23.4±2.1 mg biotin/g fiber and 33.5±8.9 mg biotin/g fiber were measured in fibers containing 5 and 10 wt % of biotin respectively, and a jump to 107.2±31.8 mg biotin/g fiber was observed in the fiber congaing 18 wt % of Biotin (Figure 4). The trend in the data to increase slowly at lower weight percent and then rapidly at 18 wt % is consistent with the findings of Li et al.[4] However, the results presented here exhibit higher surface available biotin than the data that Li et al.[4] gathered. This trend may be explained by the increase of phase separation of biotin at higher concentrations. Biotin is a polar molecule that experiences phase separation from the solvent, DMF, at room temperature. During the electrospinning process, the jet cools below 70°C, causing phase separation. Additionally, the electric force applied to the spinning solution could attract the highly polar portion of the biotin molecule, bringing it to the surface of the non-conductive PLA fiber.[6]

Water Resistance Test

The water resistance test was developed to test the fibers' ability to resist degradation and to retain surface available biotin after being immersed in water. PLA and PLA/PLA-b-PEG fiber mats containing 18 wt % of biotin were immersed in water in two trials. The first trial was removed from the water after one day; the second was removed after one week. The surface available biotin was then measured, again using the colorimetric assay. The resulting amounts of surface available biotin are shown in Figure 6. The fibers' resistance to degradation was measured by the change in weight they experienced after being submerged in water. The resulting weight loss is shown in Figure 7.

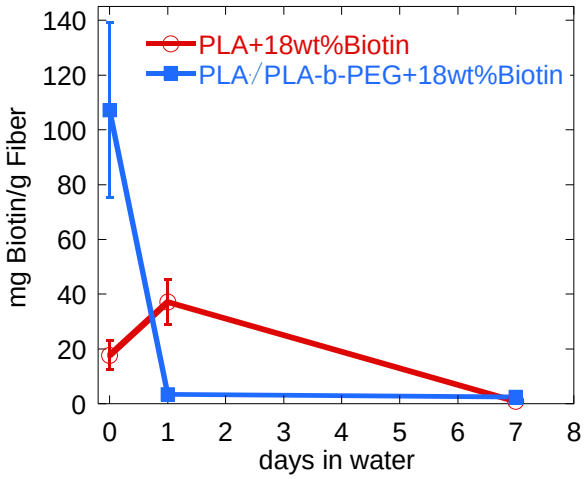

Figure 6. Comparison of surface available biotin in fibers containing 18 wt% biotin over time immersed in water.

A loss of biotin or PLA-b-PEG block copolymer or both, may account for weight differences (high molecular weight PLA is expected to be unaffected by water). From Figure 6, it is clear that the PLA/PLA-*b*-PEG fibers with 18 wt % of biotin are the ones that lost most of weight, 26 ± 0.6 % over the course of a week. The same fiber soaked during one day lost 20.7 ± 2.1 % of its

original weight. The PLA/PLA-*b*-PEG fibers containing no biotin show a smaller change in weight, 1.0 ± 0.9% over a day and 9.4 ± 3.7% over a week. These results indicate that after one day in water the fibers mainly lose biotin and after one week, they lose both the biotin and the PLA-*b*-PEG block copolymer. This assertion is verified by data from Figure 4, which shows that the PLA/PLA-*b*-PEG fiber with 18 wt % of biotin decreased its surface available biotin to 3.4±1.0 mg biotin/g fiber and 2.5±1.0 mg biotin/g fiber after being immersed in water during one day and one week respectively.

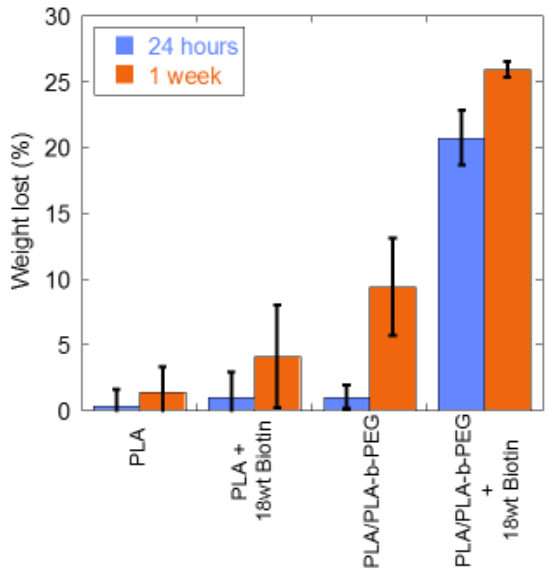

Figure 7. Weight loss of fiber mats after 1 day and at 1 week of being immersed in water.

Conclusions

When biotin is incorporated to PLA fibers, it is evident from the results that the addition of PLA-*b*-PEG block copolymers enhances the phase separation of biotin towards the fiber surface while decreasing the fiber diameter. PLA/PLA-*b*-PEG fibers containing 18 wt % of biotin presented the highest amount of available biotin at the surface. All fibers, however, experienced degradation in water testing, losing both PLA-b-PEG block copolymer and surface available biotin.

Future Work

In the future, our group plans to continue researching functional biosensors in the hopes of developing a system for the detection and filtration of pollutants in aqueous systems. Such a system would make use of the large contact area of the nanofibers discussed in this paper.

Acknowledgements

This work made use of the Cornell Center for Materials Research Shared Facilities, which are supported through the NSF MRSEC program (DMR-1120296).

References

1. Cramariuc, B. et al. Fiber diameter in electrospinning process. Journal of Electrostatics 71, 189–198 (2013).
2. Ikada, Y. & Tsuji, H. Biodegradable polyesters for medical and ecological applications. Macromolecular Rapid Communications 21, 117–132 (2000).
3. Menzies, K. L. & Jones, L. The Impact of Contact Angle on the Biocompatibility of Biomaterials. Optometry and Vision Science (2010).
4. Baeumner, A. J. Biosensors for environmental pollutants and food contaminants. Analytical and Bioanalytical Chemistry 377, 434–445 (2003).
5. Edwards, K. A., Clancy, H. A. & Baeumner, A. J. Bacillus anthracis: toxicology, epidemiology and current rapid-detection methods. Analytical and Bioanalytical Chemistry 384, 73–84 (2005).

6. Li, D., Frey, M. W., Vynias, D. & Baeumner, A. J. Availability of biotin incorporated in electrospun PLA fibers for streptavidin binding. Polymer 48, 6340–6347 (2007).
7. Li, D., Frey, M. W., Vynias, D. & Baeumner, A. J. Availability of biotin incorporated in electrospun PLA fibers for streptavidin binding. Polymer 48, 6340–6347 (2007).
8. Kiss, É., Bertóti, I. & Vargha-Butler, E. I. XPS and Wettability Characterization of Modified Poly(lactic acid) and Poly(lactic/glycolic acid) Films. Journal of Colloid and Interface Science 245, 91–98 (2002).
9. Buttaro, L. M., Drufva, E. & Frey, M. W. Phase separation to create hydrophilic yet non-water soluble PLA/PLA-b-PEG fibers via electrospinning. Journal of Applied Polymer Science 131, (2014).
10. Hendrick, E. & Frey, M. Journal of Engineered Fibers and Fabrics 9, 153–164 (2014).

Design, Assembly, and Characterization of SQUID Testing Platform

Rekha Schnepf

PI: Katja Nowack

Graduate Mentors: Jihoon Kim,

David Low, Kevin Nangoi,

and Brian Schaefer

(Dated: August 6, 2015)

Abstract

Superconducting quantum interference devices (SQUIDs) are highly sensitive magnetic field probes. In order to use a SQUID it is important to ensure that the device and connected wires are at a cold enough temperature. We conducted Johnson-Nyquist noise experiments in an effort to determine if the wires within the cryostat are thermalizing to 4K. We cooled two resistors in the cryostat and measuring the noise at the various temperatures. We determined that the wires are only reaching around 68K and that there is parasitic capacitance of about 600 pF in a parallel circuit with the resistors. Future efforts will be focused on thermalizing the wires and removing the parasitic capacitance.

INTRODUCTION

Magnetic field imaging is a useful method of studying complex systems and novel materials. One method of taking highly sensitive magnetic field measurements is to use a superconducting quantum interference device (SQUID). SQUIDs are intrinsically sensitive to magnetic flux and thus can be used to make some of the world's best tools for measuring magnetic field [1].

A SQUID consists of two Josephson junctions in parallel. Each Josephson junctions obeys the Josephson equations:

$$I = I_0 \sin \delta \tag{1}$$

$$V = \frac{\hbar}{2e} \frac{d\delta}{dt} \tag{2}$$

where δ is a phase difference across the Josephson junction, I is current flowing through the junction, V is voltage, and $\hbar$ is Planck's constant. When the junctions are in parallel, flux threading through the loop induces a phase difference over the junctions which creates a current by equation 1 and a voltage across the device by equation 2. The IV characteristics of this device for integer values, $\Phi_a = n\Phi_0$, and half-integer values, $\Phi_a = (n + 1/2)\Phi_0$, of applied flux is shown in figure 1. If we current bias the device at I_b, the voltage across the SQUID varries as a function flux in units of ϕ_0 as shown in figure 2 [2]. It is important to keep the device at the optimal I_b and applied flux to maintain the device in its most sensitive regime.

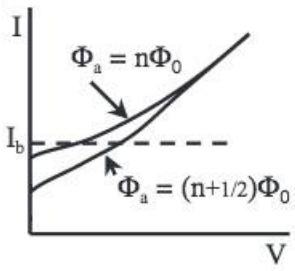

FIG. 1. Plot of integer and half-integer values of applied flux, panel adapted from [2].

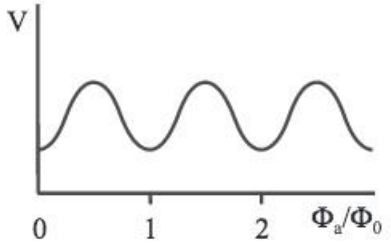

FIG. 2. Voltage vs. flux for a constant bias current, panel adapted from [2].

While it is possible to use a bare SQUID loop for magnetic imaging, a number of im-

provements that provide enhanced sensitivity and capabilities are shown in figure 3. To eliminate the flux from a uniform background magnetic field, we introduce a symmetric counter wound section of the SQUID loop formed by a twist in the center. To keep the SQUID in its most flux sensitive regime, a modulation coil is placed near the SQUID loop to maintain optimal constant flux. An integrated field coil, located near the pickup loop, is capable of applying a local magnetic field to the sample. Together, this gives us a magnetic sensor with micrometer precision and a flux noise floor of $\sim 0.25\mu\Phi_0/\sqrt{\text{Hz}}$ [1].

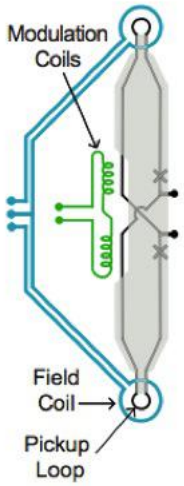

FIG. 3. SQUID schematic [1].

The SQUID sits in a sample chamber that is cooled using a Cryostat, as shown in Figure 4. A thin film niobium (Nb) SQUID is used, which becomes superconducting at under 9 K, thus it is critical to ensure that the sample chamber and resulting wires are thermalized. One method to determine the temperature of wires within the chamber is to place a resistor within the chamber and measure its Johnson-Nyquist noise. Johnson-Nyquist noise is an inherent voltage fluctuation in any resistive material. The Johnson-Nyquist root mean square noise voltage across any resistance R at temperature T in a frequency range B is [3]:

$$V_j = \sqrt{4k_B TRB} \tag{3}$$

where k is the Boltzmann constant. If the voltage noise and resistance of the resistor are known the temperature can be found using equation 3. Our goal was to design and implement Johnson-Nyquist noise measurements to determine the temperature of wires in the sample chamber.

FIG. 4. Image of the sample chamber and Cryostat.

EXPERIMENTAL METHODS

Measurement Setup

The testing setup for both the Johnson-Nyquist noise measurements consists of placing the resistor in the sample chamber. The resistor was then connected to wires that travel out from the chamber to a breakout box. The SQUID testing setup also consisted of placing the SQUIDs in the sample chamber and connecting them to wires that travel out to the breakout box. However, in order to test the SQUIDs, the SQUIDs need to be mounted onto a chip carrier that sits in a chip carrier socket that is soldered to a PCB. An image of a SQUID on the PCB and a schematic of the SQUID testing set-up is shown in figures 5 and 6.

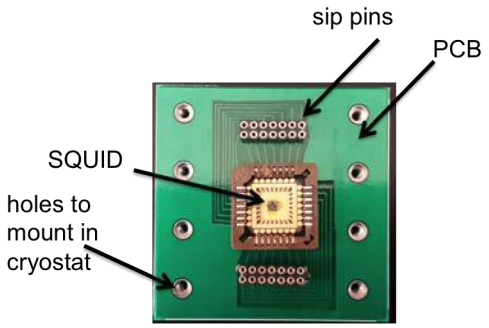

FIG. 5. Image of a SQUID on the PCB board. Wirebonding is used to connect the SQUID to the pads of the chip carrier.

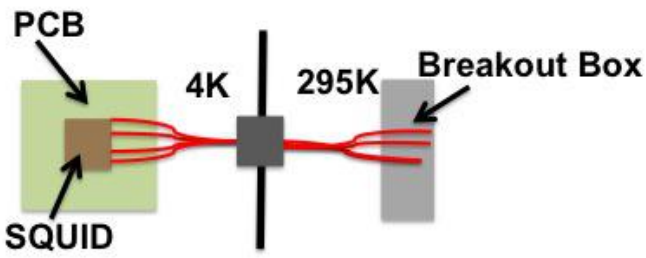

FIG. 6. Schematic of the SQUID testing set-up, depicting the wires traveling from the SQUID in the chamber at 4K to the outside at 295K.

I designed and ordered a breakout box from Protocase Designer for use during these measurements. The breakout box design is shown in figure 7. However, the first box received from Protocase was not conductive, which is necessary to ensure that all of the connectors are grounded properly. So we used a Aivon breakout box was used instead for the measurements.

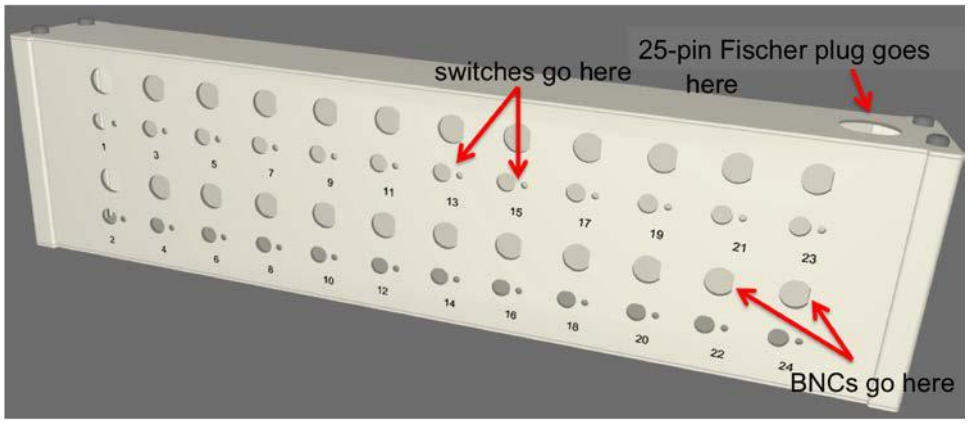

FIG. 7. Image of the breakout box design created using Protocase Designer. Arrows are indicating where the BNC connectors, switches and 25-pin Fischer plug would be mounted.

Johnson-Nyquist Noise

The first step in using Johnson-Nyquist noise to determine the temperature of the wires within the sample chamber was to successfully measure the Johnson-Nyquist noise from a resistor outside of the chamber at room temperature. To accomplish this, six resistors of with resistances ranging from .98 to 42.25 kOhm were chosen and soldered into shielded boxes with BNC connectors on the sides. BNC cables were then connected onto either side of the box on one end and connected to a model 5113 preamplifier on the other end. The input of the preamplifier was then set to DC mode with the inputs differentially coupled. A passband was set from 3 kHz to 300 kHz and the output of the preamplifier was connected to the SR760 spectrum analyzer. For each set of resistors measured, the predicted value of the voltage noise, found using equation 3, was calculated and compared to the found value. The measurements were taken by choosing a frequency bandwidth $2KHz$ where there were no unusual peaks or distortions from the SR760 spectrum analyzer and the voltage was after 1000 averages. The voltage noise measured from the resistor was larger than the predicted noise. We realized that in order to improve the accuracy of the measurements the background noise of the spectrum analyzer and preamplifier should be subtracted. The background noise of the spectrum analyzer and preamplifier was found by measuring the preamplifier with shorted inputs. The background was subtracted using the following equation:

$$V_{corrected} = \sqrt{V_{measured}^2 - V_{background}^2} \tag{4}$$

The improved results once the background noise was taken into consideration is shown in figure 9.

Once we determined that the voltage noise could be accurately measured the next step was to try measuring it with resistors inside the sample chamber at various temperatures. A 2.47 kΩ and a 10.06 kΩ resistor were soldered to a PCB board which was thermally anchored to the cryostat's cold plate. The voltage noise of the two resistors was then measured at nine different temperatures, ranging from 5 K to 110 K. The background noise was subtracted for each measurement. A plot of the data is shown in figure 10.

Next we tried measuring the voltage noise with resistors inside the sample chamber at various temperatures. We performed voltage noise measurements with resistors positioned within the chamber in two ways: 1) soldered on to the PCB board and 2) soldered directly to the sip pins that would otherwise have been connected to the PCB board. The resistor

on the PCB board would be in thermal contact with the platform of the chamber and should therefore thermalize more easily. The resistor that is free standing should have a harder time thermalizing and give a representation of the temperature of the wires in the system. The two positions for the resistors within the chamber are shown in 8. A resistor that had a resistance of 12.2 kOhm at room temperature (10 kOhm after being cooled to 4 K) was placed in the free standing position and a resistor of 10.06 kOhm was soldered to the PCB board. We measured at seven different temperatures ranging from 4 K to 180 K with a frequency bandwidth of $5kHz$ and the background noise was subtracted for each measurement. The results of the measurements are shown in 11.

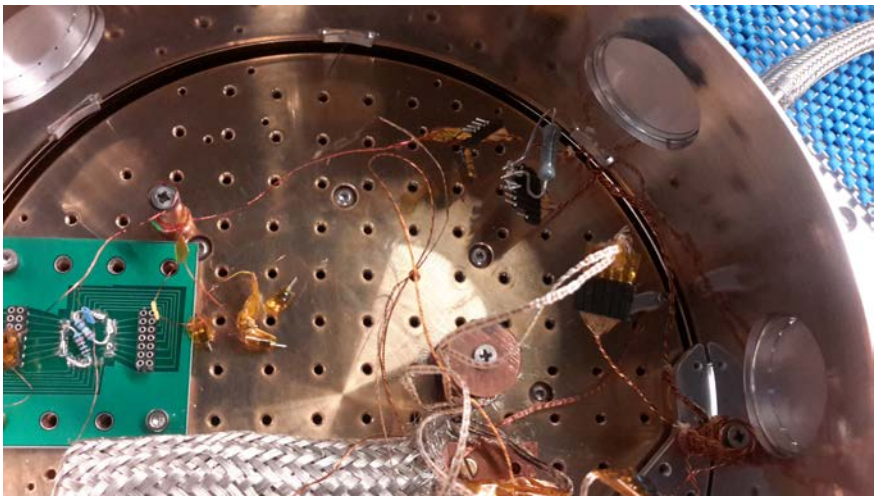

FIG. 8. Image of the resistors inside the chamber. On the left, two resistors are shown soldered to the PCB board, however only one was used in the measurements. On the right, a resistor can be seen soldered directly to zip pins.

RESULTS AND ANALYSIS

The measurements completed with multiple resistors at room temperature indicated that after subtracting the background noise we could indeed accurately predict the voltage noise of a resistor given the temperature and resistance. The only large deviation from the predicted path occurred with the largest resistor measured, 40 kΩ, where the measured noise was below the predicted value. However, this can be explained since with the larger resistance the impedance deviates more from the resistance. These results are shown in figure 9.

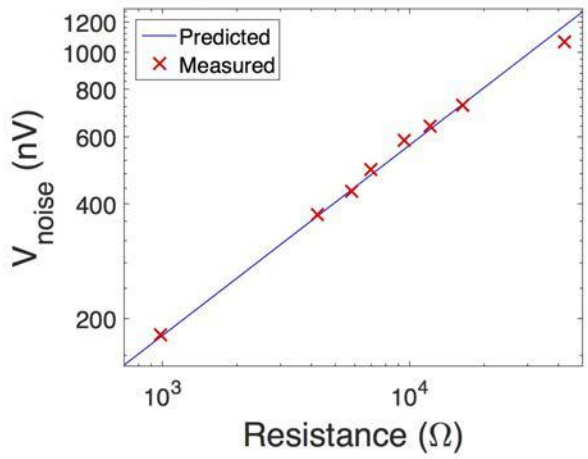

FIG. 9. Plot showing the measured voltage noise over a 2 kHz bandwidth. The graph indicates that the measured voltage noise of the resistors was larger than the predicted values. As can be seen in the graph when the background noise was subtracted the voltage noise matched up more closely with the predicted values. The largest resistor deviates some from the predicted path, probably due to its impedance deviating more from the resistance

After measuring the Johnson-Nyquist voltage noise of two resistors on a PCB board in the sample chamber at different temperatures we were able to conclude that the noise followed the predicted path. These results, shown in figure 10, provided confidence that the voltage noise could be used to determine the temperature of the wires in the system.

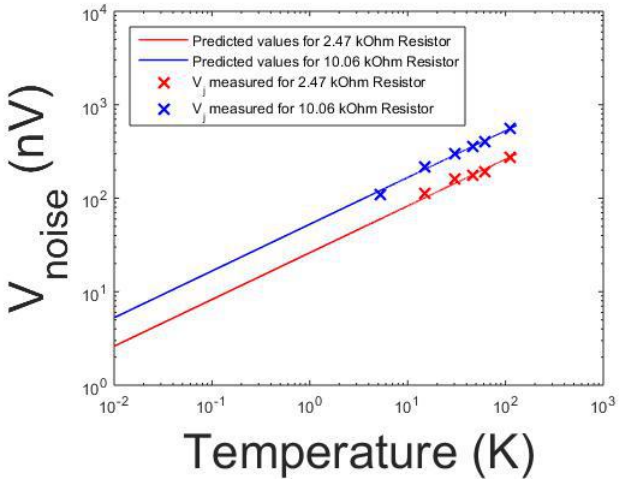

FIG. 10. Plot indicating that the measured voltage noise of the resistors on the PCB board in the chamber followed the predicted pattern.

The measurements for the floating resistor and resistor on the PCB showed noise levels much lower than the predicted values for a 10KΩ resistor, shown in 11. These results were unexpected, if the measured noise had been higher than the predicted values this could have been easily explained as there being extra noise sources. However, these results must have arisen from another problem. We investigated the possibility of it being caused by a form of parasitic capacitance.

Impedance in a parallel circuits add using the following rule:

$$Z_{parallel} = \left(\frac{1}{Z_1} + \frac{1}{Z_2}\right)^{-1} \tag{5}$$

From equation 5 it can be seen that a very small Z_2 can greatly affect the value of $Z_{parallel}$.

The impedance of a capacitor is characterized using:

$$Z_c = \frac{1}{iC\omega} \tag{6}$$

where ω is the frequency and C is the capacitance. Plugging equation 6 into equation 5 and setting $Z_1 = R$ results in:

$$Z = \left(\frac{1}{R} + iC\omega\right)^{-1} = \frac{R}{1 + iCR\omega} \tag{7}$$

$$|Z| = \frac{R}{\sqrt{1 + \omega^2 C^2 R^2}} \tag{8}$$

Then solving for the capacitance:

$$C = \frac{1}{R\omega}\sqrt{\frac{R^2}{|Z|^2} - 1} = \frac{1}{2\pi f R}\sqrt{\frac{R^2}{|Z|^2} - 1} \tag{9}$$

Now using equation 9 we tried to determine what values C could be. First, by manually adjusting the value of R in equation 3 we determined that a better fit to our data occurred when $|Z| \sim 7.5k\Omega$, shown in figure 11. Then plugging $|Z| = 7.5k\Omega$, $R = 10k\Omega$ and $f = 44kHz$ (the middle of the bandwidth used) into equation 9 we discover that $C \sim 600pF$. One factor that may have caused the parasitic capacitance was a change in the wiring between the measurements of the two resistors on the PCB and the floating resistor and resistor on the PCB. For the first measurement twisted pairs were connected from the 30 gauge wire in the cryostat to the sip pins by the resistor. Essentially, either end of the resistor was connected to a twisted pair. In the second set of measurements, with the floating resistor

and resistor on the PCB, a change in the wires was made by twisting the twisted pairs together, it is possible that this caused the parasitic capacitance.

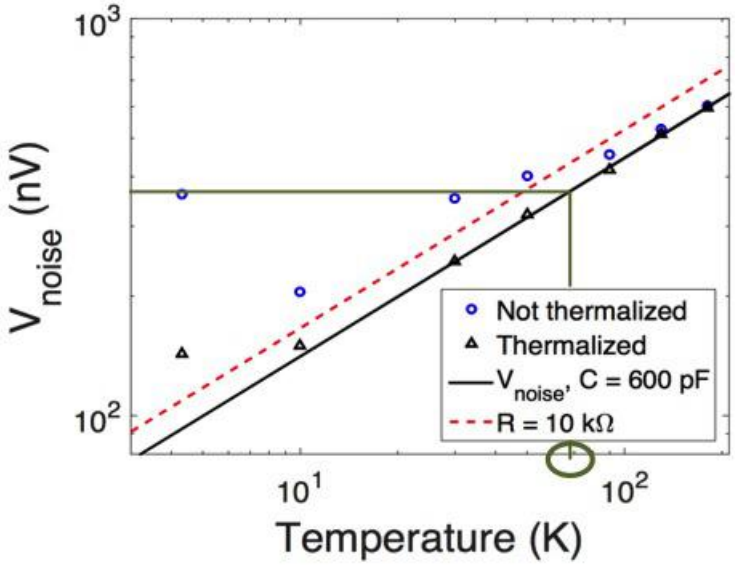

FIG. 11. Graph of the measured voltage noise over a 5 kHz bandwidth starting at 23.5 kHz from the floating resistor (non-thermalized) and resistor on the PCB (thermalized). It can be seen that the measured noise from the thermalized resistor was below the predicted curve for the 10 kΩ resistor. However, once a capacitance of 600 pF was taken into consideration the data matched the predicted values. It is also shown that the non-thermalized resistors may have only been reaching ∼68K.

In addition to discovering the parasitic capacitance of 600 pF, from figure 11, we also learned that the floating resistor thermalized only to ∼68 K. This can be gleaned from the fact that the voltage noise at 4 K and 30 K was about the same. The fact that the floating resistor only reached 68 K indicates that the wires in the chamber are also probably only thermalizing to 68 K. In addition, the second data point at 10 K is likely the result of human error during testing and can be disregarded.

CONCLUSION

We conducted various experiments with the voltage noise of resistors in an effort to determine the temperature of wires within the sample chamber of the montana system.

From these experiments we learned that the wires in the sample chamber are only reaching around 68 K. We also discovered that there is a parasitic capacitance in a parallel circuit with the resistors. We were able to approximate the parasitic capacitance to 600 pF. Future efforts that will be pursued by the group include determining what is causing the parasitic capacitance and how to thermalize the wires to 4 K. This will include future measurements with the floating resistor connected to wires that are thermally anchored in a more thorough way.

ACKNOWLEDGMENTS

I would like to thank Katja Nowack, Jihoon Kim, David Low, Kevin Nangoi, and Brian Schaefer for guiding and teaching me throughout the summer. I would also like to thank CCMR and the NSF for organizing and funding the REU program.

REFERENCES

[1] M. Huber and et. al. Gradiometric micro-squid susceptometer for scanning measurements of mesoscopic samples. *Review of Scientific Instruments*, 79, May 2008.

[2] John Clarke and Alex I Braginski, editors. *The SQUID Handbook*. Wiley-VCH, 2004.

[3] Keith Ruddick. *Physics 4052 Lab Manual: Noise Measurements*. University of Minnesota, 2013.

Variation of Nanoparticle Concentration to Determine Ideal Absorption Thickness

Chasen Shaw, Ben Treml, Kevin Whitham, and Tobias Hanrath
CCMR, Cornell University, 142 Sciences Dr, Ithaca, NY 14850
(Dated: August 5, 2015)

A 114 μM solution of PbS nanoparticles of diameter 3.5 nm and hexane was diluted using different dilution factors to find the ideal concentration. A different solution of 248.8 μM with nanoparticles of diameter 3.4 nm was used to make films to measure the degree of error from scattering.

I. BACKGROUND

The crucial idea behind quantum dots is that the wavelength they can absorb is inversely proportional to their size. This phenomenon is of use to the materials sciences, particularly in solar power, because most known materials only absorb a certain part of the spectrum. Quantum dots allow scientists to control what parts of the spectrum are absorbed in the material.

The science of how this occurs comes down to the size of the nanoparticles. Excitons are the critical part of solar cells, made up of an electron and a hole. When an electron is excited from the valence band to the conduction band, it creates a photovoltage. A photocurrent can be made by connecting the valence band and conduction band, with the electrons flowing through some sort of wire to travel into the valence band. Excitons are the size of one Bohr radius, but quantum dots are even smaller, restricting the possible energy levels of electrons. This situation can thus be modeled as a particle in a box, the quantum dot acting as a sort of potential well. As the volume of the well is reduced, the energy of the states increase, as shown by the following equation:

$$E_n = \frac{n^2\hbar^2\pi^2}{2mL^2} \tag{1}$$

These nanoparticles can be made under varying conditions depending on whether cation exchange is intended or not. Cation exchange is a process wherein PbSe quantum dots are made, then Pb^{2+} cations in the core are exchanged with Cd^{2+} to yield higher photoluminescence quantum yield in the near-IR as well as many other advantages. If cation exchange is not intended, the nanoparticles can be made under a Schlenk line with nitrogen flow to prevent oxidation. When considering cation exchange, synthesis is usually done in a glovebox kept in nitrogen atmosphere.

The standard procedure for the PbSe quantum dots starts by degassing a mixture of lead acetate trihydrate, oleic acid, trioctylphophine, and diphenylether at 120°C for 2 hours. The gas resulting from the process is evacuated and replaced with nitrogen and cooled down to room temperature. The solution is then mixed with Se in trioctylphophine and fast injected into a flask of diphenylether kept under nitrogen atmosphere and a temperature of 190°C. This mixture was kept at 155°C for 20 min and then it's fluorescence was decreased using a 1:2 mixture of methanol and butanol. It was then purified with two cycles of precipitation in methanol, centrifugation, and redispersion in toluene [1].

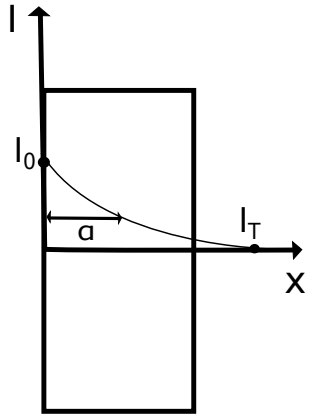

FIG. 1: Incoming intensity decreases by $I = A_0 exp(-\frac{x}{\alpha})$.

II. METHOD

Even though the size of quantum dots can be controlled, this can only be done during synthesis, but the thickness of the films and their absorbance can be controlled by decreasing the concentration of quantum dots in solution. Given this, a minimum thickness of the film would be the diameter of one quantum dot. While it is intuitive that a thin film would be undesirable, it minimizes the energy absorbed and electrons captured, making the film too thick is also problematic. The reason for this is penetration depth, where the intensity of the light passing through the material is described by the equation:

$$I = A_0 exp(-\frac{x}{\alpha}) \tag{2}$$

Where α is defined as the penetration depth, or the distance it takes for the intensity to decrease by 33% (see Fig. 1). For this reason, the intensity can never reach zero, but if the film is too thick the intensity will be so small that instruments may not be able to pick it up. This leads to error and discrepancy when graphs of wavelength vs. absorbance are compared to wavelength

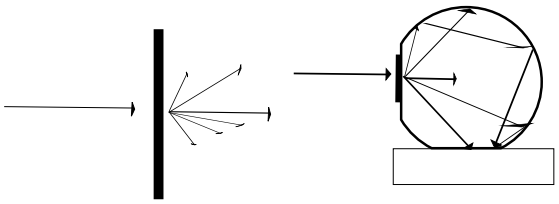

(a) Scattering (b) Integrating Sphere

FIG. 2: Scattering vs. an Integrating Sphere.

vs transmission graphs. The Beer-Lambert Law relates the two, $T = 10^{-A}$, but the two decrease differently so one instrument could measure zero where there is really just a number approximate to zero.

For this reason, it was important to make 7 sample vials to determine what the ideal concentration for the films should be. To do this, a sample of solid PbS was diluted with 500 μL of hexane to break it down into a form that could be used, hexane being used since it evaporates quickly. To measure the resulting concentration, 50 μL of the solution were placed into a different vial and the hexane was allowed to evaporate for a few minutes. After about 10 minutes or so, the nanoparticles were diluted with 3 mL of tetrachloroethylene (TCE). TCE was used for a similar reason to hexane, it was a liquid medium with which to suspend the nanoparticles so their absorbance peaks can be measured. TCE is better than hexane, because hexane has peaks between 1350 nm and 2800 nm in wavelength, while TCE has negligible absorbance. This mixture was then transferred into a quartz vial, quartz being used since it does not interact with light. The absorbance vs. wavelength was measured from 400 to 2800 nanometers on a Cary 500 UV-Vis Spectrometer. A similar process was done seven more times, but with 10 μL of PbS. This was done to find an ideal thickness for the films.

Another important process is the production of films for solar cells, which has a number of methods but the simplest is just letting it disperse for an hour. This is done by taking 3 mL of ethylene glycol and inserting it into a teflon well, and then injecting 75 μL of PbS, suspended in hexane, onto the ethylene glycol. The teflon does not interact with the ethylene glycol so it is free to move, and the ethylene glycol does not interact with the PbS, so it is free to disperse. Once the PbS is injected onto the ethylene glycol, there is about 30 seconds before the solvent evaporates, keeping the nanoparticles from dispersing. To stop this, the teflon well must be covered within 30 seconds to trap in the solvent and keep it from evaporating. Once this is done, the nanoparticles need to be allowed to disperse for an hour. After an hour, a glass plate is carefully dipped into the teflon well then the ethylene glycol is cleaned off. At this point, the absorbance of the film is measured by the UV-Vis Spectrometer.

One field of study here is scattering of light from the films. When an incoming beam of light goes through the film, the light coming out may not come out straight, it could come out at an angle. If you assume the light comes out straight, there is a degree of error from the scattering. To measure the level of error, three different films were made from solution at the same concentration. The absorbance of the films was measured with the UV-Vis Spectrometer, but the % transmission was also measured using an integrating sphere attachment to the spectrometer. The integrating sphere is essentially just a white sphere that adds together all the scattered light beams to account for the error due to scattering (see Fig. 2). An average and standard deviation were taken from the results to find the error due to scattering.

III. RESULTS

The concentration can be found from the Beer-Lambert Law, $A = \epsilon_{400}cl$, where A is the absorbance, c is the concentration, l is the length of the quartz vial used to measure concentration, and ϵ is a variable that changes with the diameter of the particle. The first thing needed is the wavelength of the peak on the wavelength vs. wavelength graph for the solution. Then you need to used the equation for the energy of one photon to convert from units of nm to eV, $E = \frac{hc}{\lambda}$. This can then be used to solve for the diameter of one nanoparticle.

$$E = 0.041 + \frac{1}{0.0252d^2 + 0.283d} \tag{3}$$

This can be used to solve for ϵ_{400} with the equation $\epsilon_{400} = (0.0233 \pm 0.0001)d^3 cm^{-1}/\mu M$ [2]. This can be inserted into $A = \epsilon_{400}cl$ to solve for concentration.

The solution was diluted in seven different vials to show the change in absorbance with concentration. Each of the vials were scanned by the spectrometer, then the data placed into IGOR, where the Multipeak fitting function was used to calculate the wavelength of the peak on the wavelength vs. absorbance graph (see Fig. 3).
A negative concentration was found for the solution. This was due to interference from hexane that had not fully evaporated in the process of making the solution. Essentially the peak for hexane was higher than the peak for the nanoparticles, but the program only focused on the nanoparticles, but used hexane's peak as a reference. This problem was solved by truncating the graph from 400-2800 nm to 400-1350 nm. Due to human error, only the concentrations of the middle four samples were correct. However, this does still prove the connection between concentration and the absorbance of a sample (see Fig. 4).

The thickness of the films can be calculated using the Beer-Lambert Law, $A = \epsilon_{400}cl$, where is found from spectrometer measurements, c is the concentration of solution and ϵ_{400} can be found from the diameter of one nanoparticle, 3.5 nm. The first part of solving this equation is

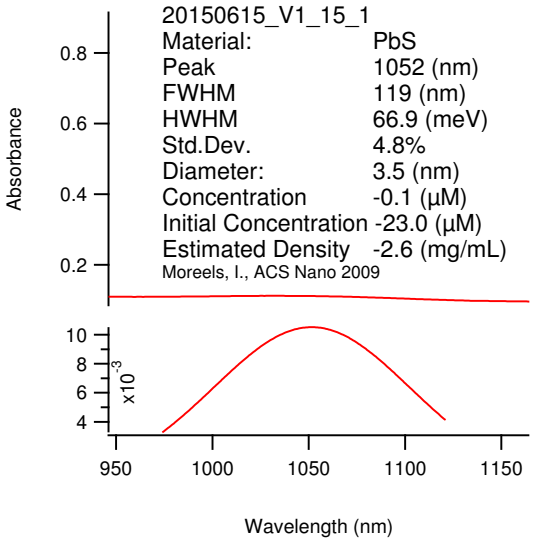

FIG. 3: A negative concentration.

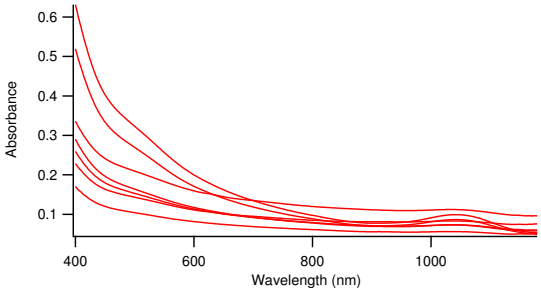

FIG. 4: Wavelength vs. absorbance for seven different concentrations.

visualizing the arrangement of nanoparticles on a slide (see Fig. 5). They're all tightly spaced cylinders in a rectangular volume. Finding the density of particles can be done by imagining one solid with hexagons for bases and rectangles for sides. The center of each sphere is a vertex of this solid. This structure of hexagonally close-packed spheres has a sphere-to-gap ratio of 0.74. The volume of 1 nanocrystal is $V_{NC} = \frac{4}{3}\pi r^3$, where r is the radius of one nanocrystal.

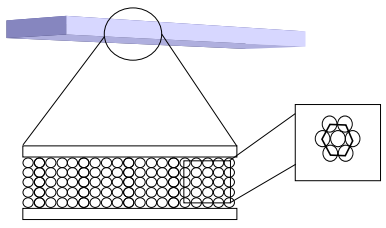

FIG. 5: A basic depiction of hexagonally close-packed spheres.

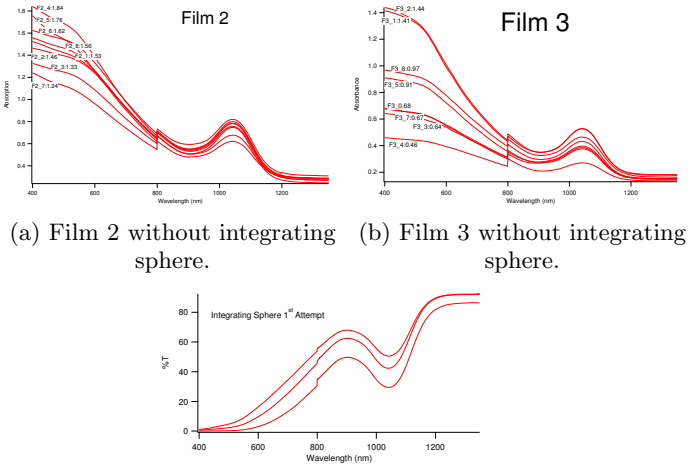

(a) Film 2 without integrating sphere.

(b) Film 3 without integrating sphere.

(c) All three films with integrating sphere.

FIG. 6: Parallel slides and Integrating sphere.

$$\frac{{V_{NC}}^{total}}{V} = 0.74 = \frac{V_{NC} \cdot \#NC}{V} \tag{4}$$

Assuming a volume 1 cm^3, the equation can be rearranged to yield.

$$\frac{{V_{NC}}^{total}}{V_{NC}} = \frac{\#NC}{1cm^3} \tag{5}$$

This can be converted to mol/cm^3 using Avogadro's number and used with the Beer-Lambert law, $A = \epsilon_{400} cl$, solving for the thickness l.

In order to proper investigate the significance of scattering in the error of the measurements, the absorbance of the samples was measured with and without an integrating sphere. Given that the error in the samples seemed unreasonable given the possibility of scattering, it was hypothesized that the slides were not homogenous enough (see Fig. 6).

The main barriers to making the slides homogenous are; there are 30 seconds to cover the film before it constricts, and the net air current inside of the fume hood. The film needs to be covered within 30 seconds to trap the solution in the teflon trough it is contained in and thus keep the solvent from evaporating. Without the solvent, the nanoparticles cannot disperse and make a film. If the film is allowed to be blown upward within the trough, it will collect at the edges and slowly disperse inward instead of outward. This second problem is solved by covering the film even faster than 30 seconds to keep the air pushing the solution to the edge (see Fig. 7).

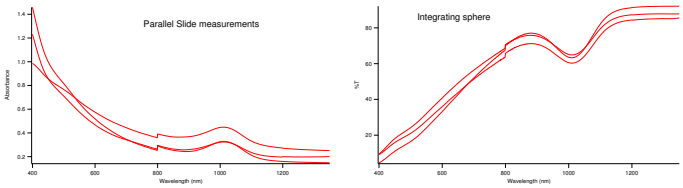

(a) New parallel slide measurements

(b) New Integrating Sphere measurements

FIG. 7: Scattering vs. an Integrating Sphere.

IV. CONCLUSION

Estimates of the values of the graphs of the parallel slides and the integrating sphere yield standard deviations of 0.255 and 0.488 respectively. If scattering were the only source of error, or even a significant source of error, the integrating sphere would have the lowest standard deviation but it has the larger one of the two. This argues that the actual source of error is not the scattering. Given problems in the measurement technique, it seems most likely that the slides were contaminated in the process of inserting them into the spectrometer. Further experiments could be done to increase homogeny and improve upon the technique.

It's not completely understood what makes nanoparticles rush into the center when making films. While solvent evaporation makes sense, there are a variety of factors to consider such as the interaction between ethylene glycol and the various molecular forces at work. An experiment to verify the involvement of solvent evaporation would involve covering the teflon trough with a parafilm punctured with holes to allow solvent to evaporate. Increasing the number of holes would help to quantify just how much solvent is needed to prevent particles from rushing toward the center. If the solvent's evaporation does have an effect on the dispersion of nanoparticles, there should be a relationship between the number of holes and the homogeny of the films. The homogeny of the films can be quantified by scanning the films in the spectrometer at different positions in the slot.

V. ACKNOWLEDGEMENTS

I would like to thank the Research Experience for Undergraduates program (DMR-1063059 and DMR-1120296) for their financial contribution to the REU.

[1] M. Casavola *et al.*, Chemistry of Materials , 294 (2011).
[2] I. Moreels *et al.*, ACS nano , 3023 (2009).

Cryo-STEM Tomographic Reconstruction of Mesoporous Silica Nanoparticles

Joseph C. Szabo*
Physics Department, Case Western Reserve University

Katherine A. Spoth
School of Applied and Engineering Physics, Cornell University

Lena F. Kourkoutis
School of Applied and Engineering Physics, Cornell University and
Kavli Institute for Nanoscale Science, Cornell University

(Dated: August 5, 2015)

Mesoporous silica nanoparticles show great potential for applications in energy and nanomedicine because of their tunable pore structure and large surface area. We have recently shown that one type of these particles dramatically changes shape upon exposure to water in its environment, which could allow molecules to be expelled from the pores. It is important to know more about the three-dimensional pore structures in order to further these materials' applicability. We examined their porous structure in hopes to gain insight into what mechanisms drive the shape change and deformation of the pore lattice. To view the 3-dimensional lattice structure, the particle samples were imaged using cryo-STEM tomography. At a temperature of -140°C, the particles were kept cold to preserve structure. Tomography was done using an array of 2-D tilt series data, and the data was used to reconstruct the particle with an iterative reconstruction algorithm. From the reconstructed 3-D data we observe that the pore structure is 3.6 nm with a resolution of at least 2.3 nm.

I. INTRODUCTION

Mesoporous silica nanoparticles (MSN's) are highly porous biocompatible materials with high catalytic and medical value due to their interior pore lattice structure that gives the particle a high surface area.Having such large surface area allows the particle to store and transport chemicalswith applications ranging from site specific drug treatment to chemical contrast imaging. This broad range of applications derives from the variable size pores that are tuned during synthesis. The pore structure may range from a few nanometers to tens of nanometers, which allows for the filtration of a wide array of materials. Much research has been done on the application of MSN's; one such study examines their shape change when exposed to humidity [1], shown in Figure 1. The focus of this work is to understand what the initial structure is like in order to determine how it changes when exposed to humidity. This information is a key requirement for advances in hybrid silica nanoparticles, where different molecules may be released once the structure collapses. Electron microscopy allows us to investigate the three-dimensional nanoscale structure of these materials.

In our research, we use electron microscopy to visualize MSN's and detail the pore lattice structure. We do so by observing the silica particles in a cryogenic state. Traditional methods of electron microscopy require drying of a sample for imaging in the high vacuum of the microscope, usually in the humid environment of the laboratory. This is not suitable for capturing the interconnected pore structure because, as seen in Figure 1, the pores deform when in atmosphere [1]. In order to take high resolution images and preserve the natural structure of the silica nanoparticles, we place snap-frozen samples in a cryo-holder and then freeze dry them under the microscope vacuum. This preserves the particle structure and allows us to use electron microscopy for analysis. Observing these particles' structure using scanning transmission electron microscopy (STEM) we can tomographically reconstruct the 3-dimensional particle. Analyzing the reconstruction will elucidate the full physical characteristics of the particle and how they relate to its shape deformation.

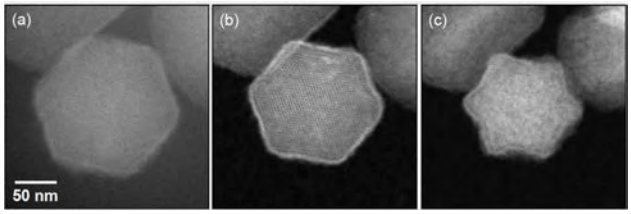

FIG. 1: STEM images of mesoporous silica particle in vitrified solution (a); freeze dried under the microscope vacuum, showing a small amount of shrinkage but no shape deformation (b); and after exposure to humid air in the lab for 24 hours, causing anisotropic shrinkage of the particle and deformation of the pore lattice (c). [1]

* jcs154@case.edu

II. METHODS

We observed MSN's in a vitreous state using plunge freezing. The silica particles are initially in an 80% ethanol, 20% water solution. A 4μL droplet is deposited on a copper Quantifoil grid overlaid with holey carbon. Prior to deposition, the grid is placed in a plasma ozone chamber, and all extraneous particulates are removed from the grid. Before the silica is deposited on the sample, 5 nm gold nanoparticles are placed on the carbon film side of the grid. These fiducials are used to for alignment and will be discussed later in 3-dimensional reconstruction process. Once the fiducials are on the carbon grid, the silica nanoparticle solution is deposited.

To prevent the sample from being too thick after it is frozen, the droplet is blotted onto a piece of thin paper twice in roughly two 4 second sessions. Extracting some of the solution is necessary because a thick layer of amorphous ice would impede our ability to resolve the pore structure of the silica nanoparticle. The remainder of the nanoparticles and thin solution are dropped into a liquified ethane/propane mixture at -196°C. This mixture allows the substrate to be cooled from room temperature in milliseconds and prevents the formation of crystalline ice that could damage the sample as well as introduce unwanted features in the power spectrum [2, p. 22].

The grid is loaded into the electron microscope under liquid nitrogen using a Gatan single-tilt cryotransfer tomography holder. Before the sample is loaded, it is kept under nitrogen to prevent ice from accumulating and maintain the particles' natural form. Using a temperature controller connected to the tilt-holder, the silica particles are warmed to -100°C. At this temperature, the ice surrounding the sample sublimates in the vacuum of the electron microscope. The silica particles are cooled down to -140°C. Maintaining these low temperatures prevents the electron beam from damaging the sample too quickly to acquire data.

A simple illustration of electron tomography is shown in Figure 2: projection images are acquired at a variety of tilt angles, then reconstructed to provide details of the three-dimensional structure of a specimen. Projection images of the silica nanoparticles are taken using annular dark field (ADF) STEM, illustrated in Figure 3. Scattered electrons are collected on a ring detector as a focused electron probe is scanned across the sample, correlating to the intensity at each pixel. This provides resolution and contrast that allows for high differentiability of the porous matrix and fiducials [3]. To reconstruct the 3-D structure of the MSN's we use STEM imaging and the single-tilt holder to acquire a tilt series. By tilting through a variety of angles we collect projection images of all the structural information through the particle. Using this array of information we tomographically reconstruct a 3-dimensional silica particle.

Projection images were collected every 2 degrees from -74° to 74°. Each image was acquired by taking 8 scans

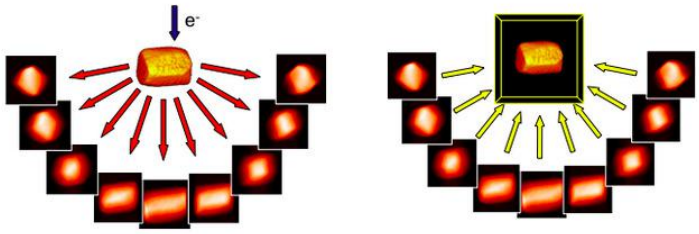

FIG. 2: Schematic illustrating the process of tomographic reconstruction. Data taken from various tilts provides information that can be used to recreate a 3D view of the sample.[4]

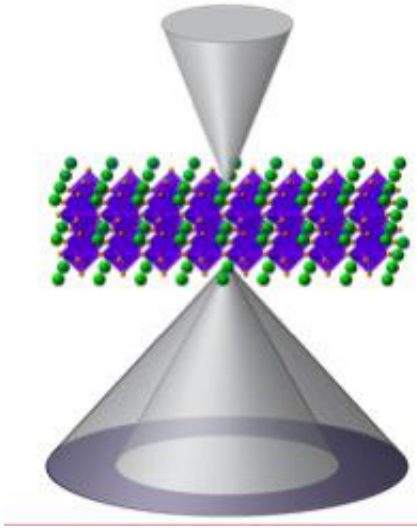

FIG. 3: Representation of how STEM imaging scans across the particle and collects scattered electrons on the ADF detector. [5]

that averaged data over one second. This was done to limit the amount of noise introduced by any slight thermal fluctuations that would impede longer averaging scans. These 8 projection images are cross correlated and then averaged to further increase the signal to noise post reconstruction.

The tomography data is aligned using the fiducial particles. These particles are bright compared to the sample thanks to the high Z-contrast in STEM imaging and allow us to easily identify fiducials in each tilt image. Taking one particle present in each tilt array, we can align the data. The axis of rotation and center of rotation are found by inspecting the continuity of the sinograms for the fiducial particles throughout the tilt series. To rebuild the 3D image, we run a multi-iteration SIRT to back project the data and eliminate errors in the reconstruction. We visualize the reconstruction in three dimensions using the analysis program Tomviz.

III. RESULTS AND DISCUSSION

The output of the reconstruction algorithm is a series of 2D slices through the sample, providing all the 3D structural information. Figure 4 shows a single slice of the reconstruction perpendicular to the internal face of the hexagonal pore lattice. Taking the power spectrum of the data reveals periodic structures in the image. As Figure 5 shows, there is a hexagonal pattern corresponding to the hexagonal pores, but the signal is noisy as seen by the blur around the peaks.

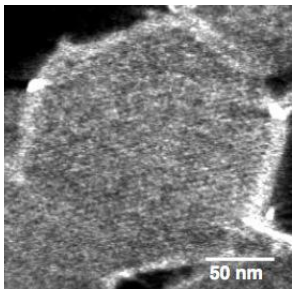

FIG. 4: Single slice of the reconstructed silica.

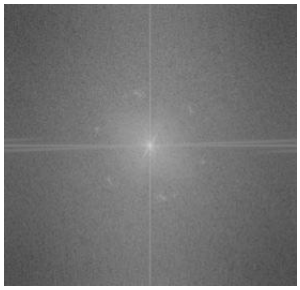

FIG. 5: Fast Fourier Transform of slice shown in Figure 4.

We create a secondary view of the pores by summing slices of the particle's interior. This enhances the contrast of the silica lattice, providing greater signal-to-noise ratio and demonstrating resolution beyond 2.3 nm. Figure 6 represents the summation of 100 slices, equivalent to 70 nm of the interior section of the particle. The reconstruction does not align the particle on axis, so prior to summing the data is rotated about X and Y in order to find the exact view where the particle's cross-section in the image is exactly perpendicular to the pore axis. This was done by estimating an approximate tilt and using MATLAB to generate a random array of X and Y rotations from 0 to 2 degrees and using the power spectrum to determine where the highest signal to noise ratio lies. Two iterations of this method were sufficient in enhancing the resolution as seen by the figures below. The S/N can be further improved by using a Hanning window, a decaying exponential from the center of the image such that when multiplied by the image it eliminates the sharp edges of the rectangular selection and any other extraneous artifacts and information. This limits the Fourier transform to just a porous section. Using this method we improve the resolution from 3-4 nm to 2.3 nm. The resolution is derived from radial distance of the peaks in the power spectrum noted in Figure 7.

The reconstruction and analysis of the data provides a clear view of the interior structure of the particle. Figure 8 shows that the interconnected pore lattice extends throughout the length of the particle. The image is created using a volume rendering that isolates only the provided pixel intensities. Though the image is obstructed by the surrounding particles and carbon film beneath, the pores visibly map through the whole particle.

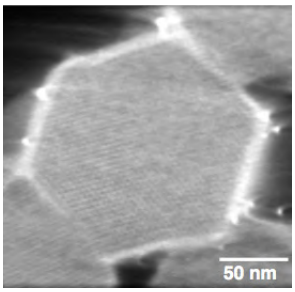

FIG. 6: Sum of 100 slices (70 nm thick) through tomographic reconstruction, showing improved S/N over the single slice in Figure 4.

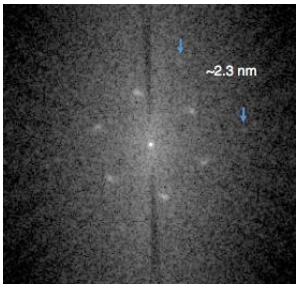

FIG. 7: Fast Fourier Transform of Figure 6, demonstrating information in the reconstruction beyond a spacing of 2.3 nm.

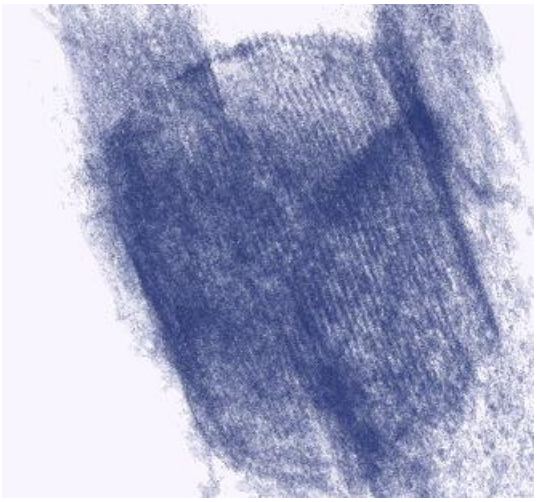

FIG. 8: 3-D Volume rendering of the silica nanoparticle in Tomviz

IV. CONCLUSION

The 3-dimensional analysis of the mesoporous silica nanoparticles shows that there is a continuous pore lattice structure that extends throughout the length of the sample. Using STEM tomography we were able to visualize the interior features of the particle, and by summing perpendicular views of the interior slices we acquire high resolution information about the three-dimensional pore structure. We measured the pore spacing to be approximately 3.6 nm and achieved a resolution of at least 2.3 nm.

Difficulties during the reconstruction and data acquisition limited the quality of the 3-D rendering. The drift of some fiducial particles during the acquisition introduced artifacts during the SIRT. Drift in gold fiducials on the

side of the particle as well as the carbon film in some cases measured as much as 5 nm. Since these particles are used for alignment, their drift makes it difficult to find the optimum conditions for alignment and creates artifacts in the reconstruction. Three different reconstructions were performed using varying values for the axis of rotation and shift. This was done to minimize the artifacts produced during reconstruction. The best data was found using a 35 iterations of a SIRT algorithm written in MATLAB.

We hoped to also collect information on a deformed particle after exposure to a humid environment and observe the effect on the pore lattice. Once the particle degraded, imaging with a similar beam intensity as used previously proved detrimental and caused the particle to degrade during observation. This prevents us from being able to collect tomographic data. Having recreated the lattice of the initial silica particle, future research should be done on how the pores changes when the particle deforms. It is not immediately clear what happens to the pores as the shape chanes, so a tomographic analysis should be done and compared to these results. This will provide a clear picture as to how the silica particle, triggered by humidity, could be utilized to release molecules from within the pores.

V. ACKNOWLEDGEMENTS

Support for this research was provided by the NSF MRSEC program (DMR-1120296). This work made use of the CCMR Shared Facilities which are supported through the NSF MRSEC program ((DMR-1120296). I'd like to thank my advisor Professor Lena Kourkoutis and my mentor Katherine Spoth for their help in completing this project. I would like to thank Dr. Robert Hovden for providing the programs to reconstruct the data as well as view the data using Tomviz. I would also like to thank the whole Kourkoutis Electron Microscopy group for all of their help and assistance during the REU program.

[1] Katherine A. Spoth, Yao Sun, Ulrich Wiesner, and Lena F. Kourkoutis. Cryo-stem reveals humidity-controlled shape change in silica nanoparticles. *Microscopy and Microanalysis*.

[2] Patrick Echlin. *Low-Temperature Microscopy and Analysis*. Springer US, 1992.

[3] M. Weyland and P.A. Midgley. 3d electron microscopy in the physical sciences: the development of z-contrast and eftem tomography. *Ultramicroscopy*, 96:413–431, 2003.

[4] 2015. URL `http://muller.research.engineering.cornell.edu/tomography`.

[5] Pengzi Liu, Robert Hovden, and Lena F. Kourkoutis. Stacking sequence of 1t-tantalum disulfide (tas2). 2015.

3-D Matrix Microstructure, Composition, and Media Synergistically Affect Endothelial Cell Vasculogenesis

Ankush Thakur[1], Michael G. McCoy[2], Claudia Fischbach[2,3]

[1]Department of Biomedical Engineering, The City College of New York, The City University of New York, New York City, NY, 10031

[2]Department of Biomedical Engineering, Cornell University, Ithaca, NY 14853

[3]Kavli Institute at Cornell for Nanoscale Science, Cornell University, Ithaca, NY 14853

Abstract

Deregulated tumor microenvironments have synergistic effects on tumor growth, progression, and metastasis, and is hallmarked by high vascular ingrowth. This up-regulated tumor vasculature may be responding to biochemical, structural, and mechanical cues from the extracellular matrix (ECM) of the tumor microenvironment. Endothelial cell vascular formation was studied in collagen gels casted in different conditions that adjusted microstructure, microarchitecture, composition, and media types. Results indicated that cell media has a profound effect on endothelial cell growth and vascular formation, with media higher in growth factors eliciting the most vascular formation. Collagen gels cast to create longer and thicker fibers, and containing EHS induce the greatest vasculature formation. These results suggest microenvironments high in growth factors, with specific microstructure and microarchitecture, and specific ECM components synergistically induce vascular invasion.

1. Introduction

Current tissue engineering techniques seek to regenerate, replace, or enhance the function of diseased and damaged tissues.[1] Furthermore, recent advances in understanding biomaterial interactions, cellular metabolism, and microenvironmental cues permit the use of tissue substitutes for studying disease pathology. Specifically, the dysregulation of the tumor microenvironment is important to replicate and study, as many different microenvironmental cues have synergistic effects in regulating tumor growth, progression, and metastasis.[2] Indeed, a hallmark of tumor progression is vascular ingrowth and tortuosity, leading to disorganized and leaky blood vessels that permit the diffusion of nutrients and oxygen as well as eventually serving as routes of metastasis.[3] Recent studies suggest that tumor vasculature may be responding to a host of biochemical, structural, and mechanical cues that are mediated by the ECM of the tumor microenvironment.

The primary component of the tissue microenvironment is the ECM, where microenvironmental changes are the most prominent. The ECM serves as the structural and biochemical ecosystem of the cell and is primarily composed of proteins such as the collagens, fibronectin, laminins, as well as a host of glycosaminoglycans and proteoglycans that serve to regulate cell behavior and function, as well as provide mechanical support. The ECM also interacts with biochemical signals such vascular endothelial growth factor (VEGF), a critical growth factor that mediates angiogenesis and vasculogenesis. By selectively sequestering and releasing VEGF, the ECM can serve as a spatiotemporal regulator of vascularization following trauma or proteolytic degradation.[4] Because the ECM plays such a protuberant role in neovascularization, studying the ECM is critical in understanding tumor-stroma relationships and how tumors are able to become vascularized.[1]

Glioblastoma Multiforme (GBM), a highly malignant grade-IV astrocytoma and primarily lethal brain tumor, is hallmarked by extensive vascularization and stromal ingrowth mediated by ECM remodeling.[5] As a model of brain microvasculature typically found within GBM tumors, human cerebral microvascular endothelial cells (hCMECs) were seeded into collagen gels and analyzed for vasculogenesis and angiogenesis.[6] Through controlling the fabrication of different matrix formulations that alter composition and structure, changing the media that was used on the cells, and changing the culture times, these data suggest methods in which hCMECs can be coaxed into undergoing vasculogenesis. Ultimately, the interactions between hCMECs, other cell types, and the matrix will provide insight into disease pathology and progression.

2. Methods and Materials

2.1 Cell culture

Immortalized human cerebral microvascular endothelial cells (hCMECs) were cultured to confluence with Endothelial Growth Media-2 (EGM-2) containing 2.5% Fetal Bovine Serum, several growth factors included in the EGM-2 bullet kit (Lonza), as well as 1% penicillin/streptomycin. The cells were cultured in T-75 cell culture flasks coated with bovine collagen type 1 at 26.35 mg/ml (BD, Biosciences) at 37℃, and 5% CO2.[7]

2.2 hCMECs Media studies

hCMECs were seeded on bovine collagen type 1 coated T-25 flasks at a density of 10^5 cells/mL. In order to test the effect of the M199 media on the hCMECs, the cells were cultured with EGM-2, M199, and a 1:1 mixture of the two media types. Media was changed every 2 days, and various images were taken using a brightfield microscope daily for a total of three days. The

images were analyzed for cell count, single cell aspect ratio, and cell circularity using ImageJ software.

2.3 hCMECs Collagen gels

The collagen gels were cast in poly(dimethylsiloxane) (PDMS) microwells, which were 250 um deep and had a radius of 2 mm. First, microwells molds made of SU-8 were fabricated using photolithography. Next, the PDMS microwells were manufactured by soft lithography using the molds created. These microwells were cut using an 8 mm biopsy punch and placed into a 24 well plate. The microwells were then surface activated to covalently bond to the collagen to prevent separation of the gels from the microwell. The microwells were plasma treated for 10 minutes, which was followed by adding 1% polyethylenimine (PEI, Aldrich Chemical) to each well for 30 minutes. Next the microwells were washed three times with sterile water for 5 minutes each. Lastly, 0.1% glutaraldehyde (GA, Fisher Scientific) was added to each well for 30 minutes, and the wells were washed again three times with sterile water.[7]

The gels consists of collagen type 1 isolated from rat tails at 1.5% [wt/vol] in 0.1% acetic acid, 10X media, cells in media, growth factor reduced Matrigel (depending on casting condition), and 1N NaOH to titrate to a pH of 7.2 to 7.4. The collagen is diluted to 0.6% [wt/vol] in the final gel, and it contains 10^6 cells/mL. hCMECs gels were made with EGM-2 media, M199 media, and a 1:1 mixture of the two. Once the gels were made, they were added to the microwells, and capped with flat PDMS caps, and they were allowed to crosslinked at 4℃ for the cold cast or 37℃ for the warm cast for one hour. Finally, the appropriate media was added to each well, and the caps were lifted. The media was changed every two days, and the gels were kept for up to 14 days at 37℃ and 5% CO2. [7]

2.4 Cell staining and imaging

The collagen gels cultures were fixed after 7 days with 0.4% paraformaldehyde for 30 minutes. Next the samples were blocked with bovine serum albumin (BSA) for 1 hour. Afterwards, extracellular Collagen IV was labeled using rabbit anti-human collagen IV antibody diluted by 1:100 overnight. Subsequently, the cells were permeabilized with triton X for 20 minutes. Lastly, the secondary antibody, donkey anti-rabbit (1:500 dilution) was added along with DAPI (1:5000 dilution) and phalloidin (1:100 dilution) to stain for the cell nuclei and cytoskeleton altogether for an hour and 30 minutes. The gels were kept in PBS until they were imaged.

2.5 Confocal immunofluorescence

A confocal microscope was used for imaging all samples collecting multiple Z-slices to form a 3 dimensional image. Images were analyzed for cell alignment using imageJ software. First, the image was flattened into a single image using a z-projection. Then the cells alignment was measured as an angle using the DAPI and phalloidin stain. Lastly, the absolute value of the deviation from the average cell angle was measured.

2.6 Live imaging

Collagen gels with hCMECs were created as described above in warm cast, and cold cast conditions, and with and without growth factor reduced EHS (in place of growth factor reduced Matrigel). They were allowed to prevascularize for 4 days. They were subsequently imaged under a live microscope in the same incubation conditions for 3 days. Images were collected at

4X magnification every 200 seconds plus imaging time. Images were analyzed with ImageJ for vascular branch length, and cell motility.

2.7 Statistical analysis

The data in all graphs is plotted with the standard deviation from the samples measured. Student t-tests were performed between groups indicated by brackets and statistical significance is indicated by *, **, or *** for P-values of less than 0.5, 0.01, and 0.001.

3. Results and Discussion

3.1 Media composition affects endothelial cell behavior in culture conditions

hCMECs are normally cultured in EGM-2, which includes several growth factors from the Lonza bullet kit including VEGF, hEGF, hFGF-B, and R3-IGF-1 which provides biochemical cues for the cells to grow rapidly and through the stages of vasculogenesis. M199 media is another endothelial cell media type also used by endothelial cells such as human umbilical cord vein endothelial cells (HUVECs). Studying the effect of using M199 media in place of EGM-2 on hCMECs was motivated by the similarities between the uses of the type media types, and the differences in growth factor supplements and fetal bovine serum (FBS) concentrations.

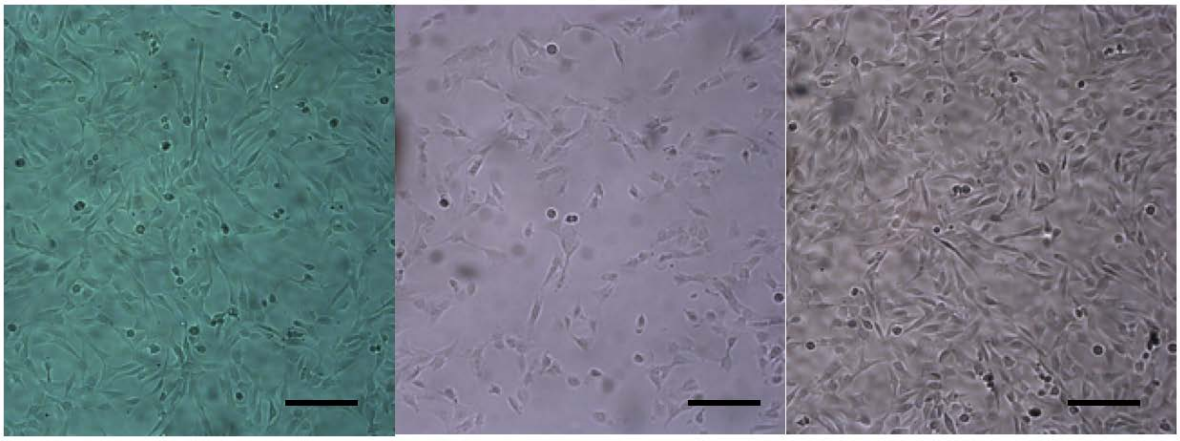

Figure 1: Bright-field images taken in each media type after three days of culturing. These images suggest that M199 media has the lowest proliferation, while the 1:1 has the highest proliferation.

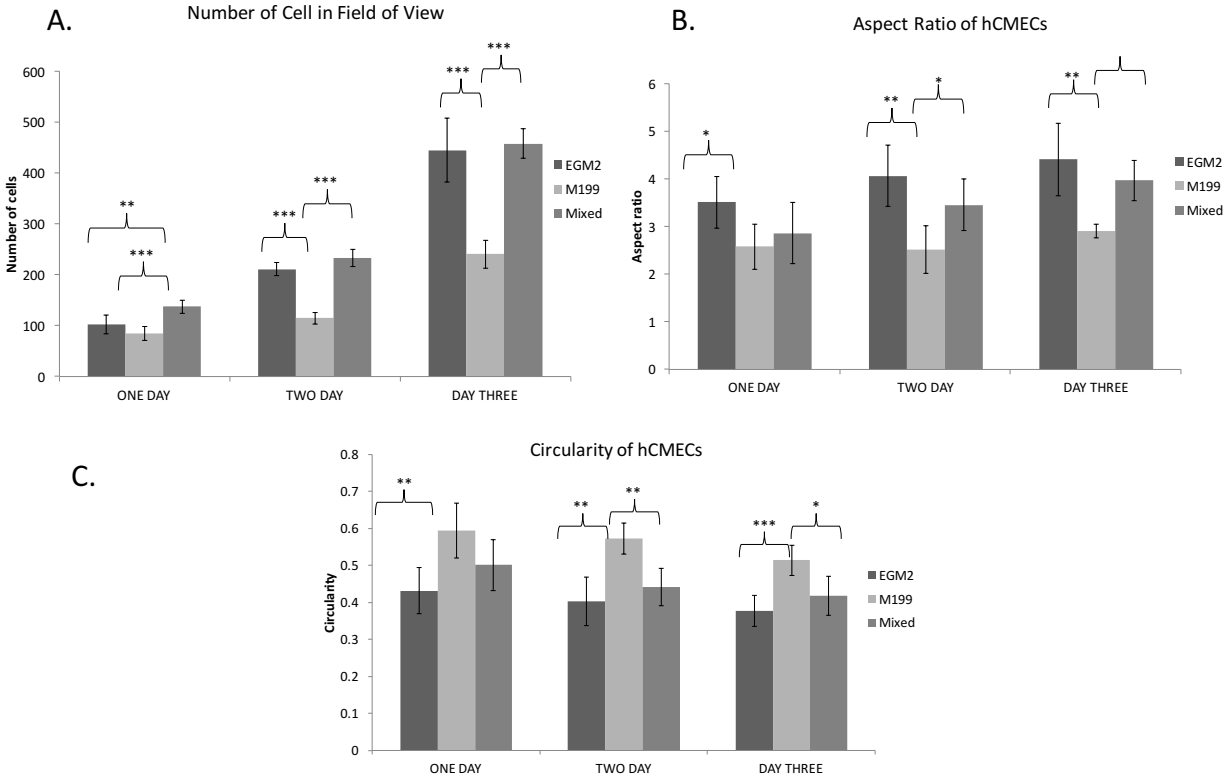

Figure 2: hCMEC cell number, aspect ratio, and circularity over three days in culture in three media types. a. The graph shows the cell number is highest for the 1:1 mixture, and lowest for the M199 media at all time points. b. The graph shows the aspect ratio decreases significantly with M199, and remains similar with the 1:1 mixture. c. The graph shows that circularity increases with M199 media and 1:1 mixture and EGM-2 remain similar.

In order to assess the effects of the different media types on hCMECs, the cells were cultured in EGM-2, M199, and a 1:1 mixture of the two on T-25 tissue culture flasks. Brightfield images from each taken after three days of culturing are shown on figure 1. The different media types had a dramatic impact on the cells, most markedly the differences in proliferation. This was confirmed when the average cell number per field of view was counted, which shows that the 1:1 mixture of the two media types has the highest proliferation, and the M199 media has the lowest (figure 2a). Furthermore, images seem to show differences in cell morphology, specifically the cell's aspect ratio and circularity, with the cells being most circular and having the lowest aspect ratio in the M199 media condition (figures 2b and 2c).

These stark differences likely result from the different growth factors and different levels of FBS in the media, with EGM-2 having various different growth factors, and M199 media having a high concentration of 20% FBS. Interestingly, the data shows that the best condition for growth, high cell aspect ratio, and low circularity is the 1:1 mixture. This likely means that the M199 media does not necessarily inhibit cell growth, induce low aspect ratio, or circularity, but that EGM-2 stimulates cell growth, high aspect ratio, and lower circularity. This can be seen in the 1:1 mixture, which exposes the cells to both higher concentrations of FBS and growth factors. High concentration of FBS in M199 media alone are unable to induce these responses from the cells, but manifest when combined with growth factors from the EGM-2 media.

3.2 Media composition affects endothelial cell behavior in 3-D collagen gels

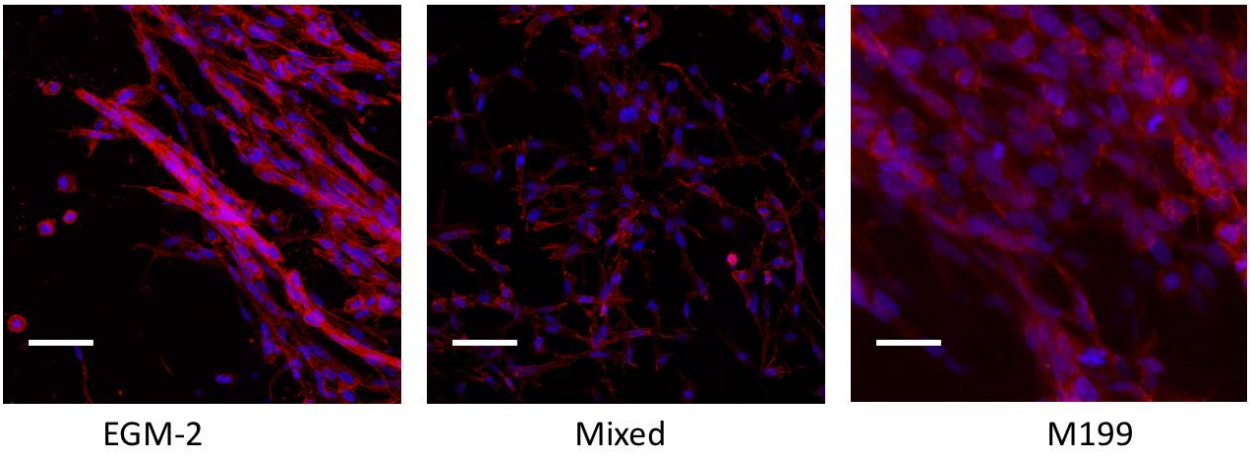

Figure 3: Z-Projection of confocal images of hCMECs in Matrigel inclusive cold cast collagen gels in different media types. Scale bars are 50 um.

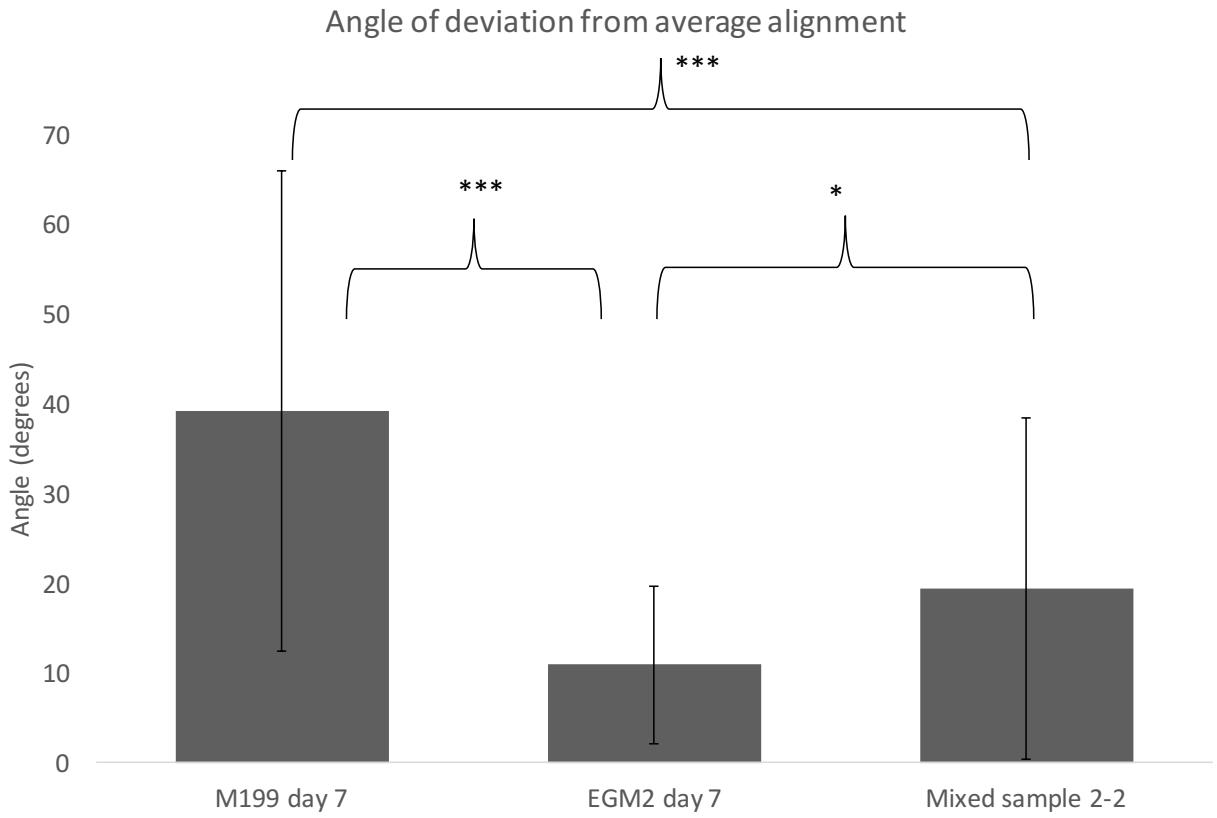

Figure 4: This graph shows the absolute value difference in cell alignment from the average cell orientation of hCMECs in collagen gels in different media types. Cells in EGM-2 are the most aligned and cells in M199 are the least aligned.

Previous studies in our lab demonstrated that the cold cast condition with Matrigel had the highest vascular potential for the hCMECs in the 3-D collagen gels.[7] Therefore, we used this condition as the baseline for the media studies because it is the best condition to promote vascular formation. Cold cast collagen gels with Matrigel were created with EGM-2 media, M199 media, and a 1:1 mixture. After 7 days, they were fixed, stained and imaged with a confocal microscope. Figure 3 shows images of each condition processed through ImageJ to create a z-projection, flattening the 3-D image. It can be clearly seen from the images that certain conditions have cells that are more aligned in one direction than others. This parameter was quantified as the mean absolute value difference between the average angle of the cells (figure 4). It is clear that the EGM-2 media and the 1:1 mixture have much more aligned cells than the M199 media.

Previous studies have shown that these cells align most in the cold cast with Matrigel condition.[7] However, it seems that the cells lose this ability if the media type is changed, and replaced with M199. Growth factors in EGM-2 such as VEGF, which are known to promote vasculogenesis are likely the cause for this change because they are in lower concentrations in M199. Additionally, because the hydrogels are fabricated using cell media, sequestration of growth factors may play a larger role in matrix remodeling in instances with higher growth factor concentrations.

3.3 Matrix composition and microarchitecture affect hCMEC vasculogenesis in situ

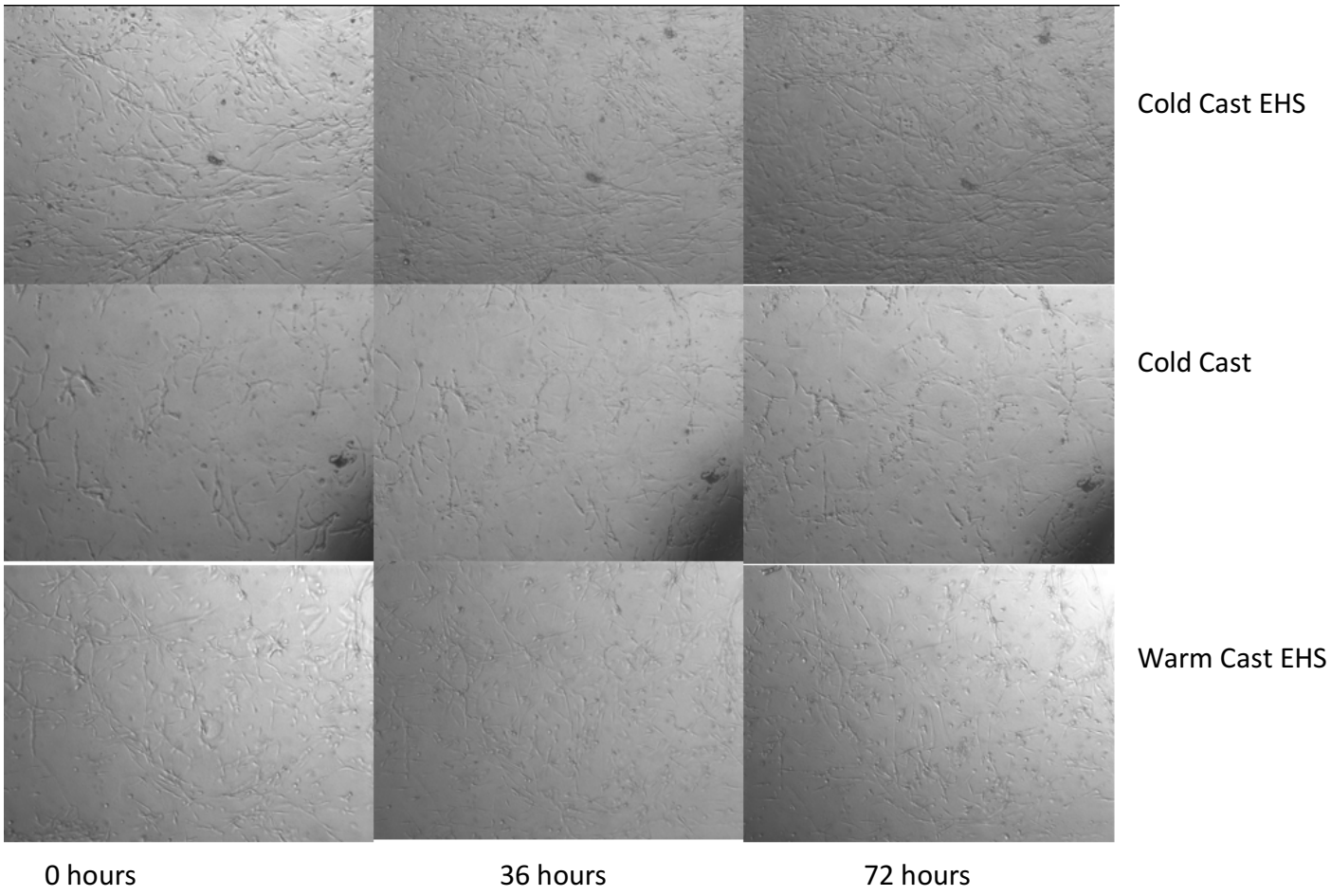

Figure 5: Select representative frames from living imaging studied of hCMECs on collagen gels from different casting conditions. Warm cast without EHS could not be imaged.

Previous studies have shown that collagen microstructure and microarchitecture can be changed by adjusting the casting conditions such as the inclusion and exclusion of Matrigel, or the changing casting temperature.[7] Specifically, the collagen fiber diameter and length was highest in the Matrigel, cold cast condition.[7] In order to further analyze the differences between vasculogenesis that occurs with these different casting conditions, collagen gels were imaged live in order to investigate the differences in vasculogenesis over time. Growth factor reduced EHS was used in place of growth factor reduced Matrigel in this study as a means of assessing if a more potent basement membrane substitute would have the same effects as Matrigel on vasculogenesis. Collagen gels with hCMECs with and without EHS, and both cold cast and warm cast were fabricated and cultured for 4 days and subsequently imaged for 72 hours. Live imaging data shows the cells are actively remodeling the matrix around them, as they burrowed

paths to move throughout the collagen gel. Additionally, select frames show that cells are forming vascular networks of branches, which grow and shrink over time (figure 5).

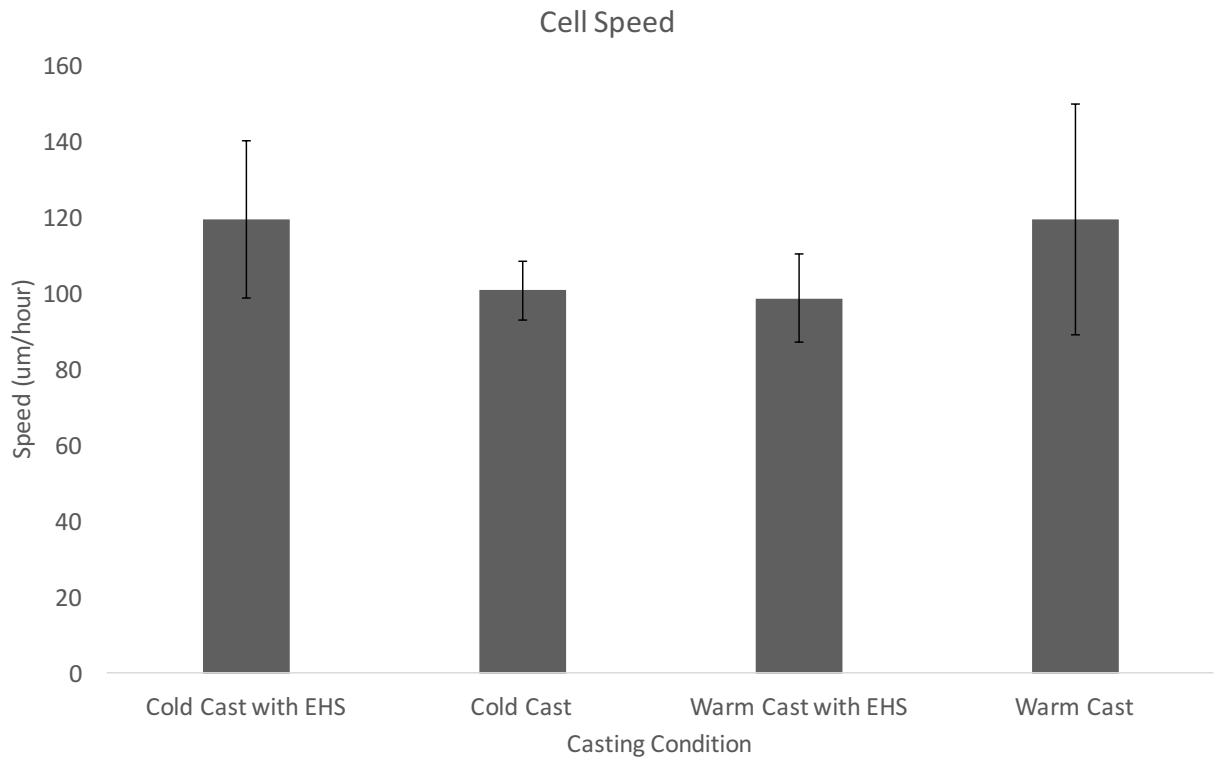

Figure 6: This graph shows the average speed of cells in collagen gels over a 6 hours period.

ImageJ was used to quantify cell motility in order to assess if differences in cell motility across the different casting conditions may be causes differences in the formation of vasculature. Singles cells were tracked over a period of 6 hours, and their average speed was determined for each condition (figure 6). The results show that there are no significant differences in cell motility across the casting conditions, which suggests that cells are moving relatively equally across the different conditions; however, matrix microstructure, microarchitecture, composition, and media regulate this movement, and organize it to form vasculature faster in certain conditions.

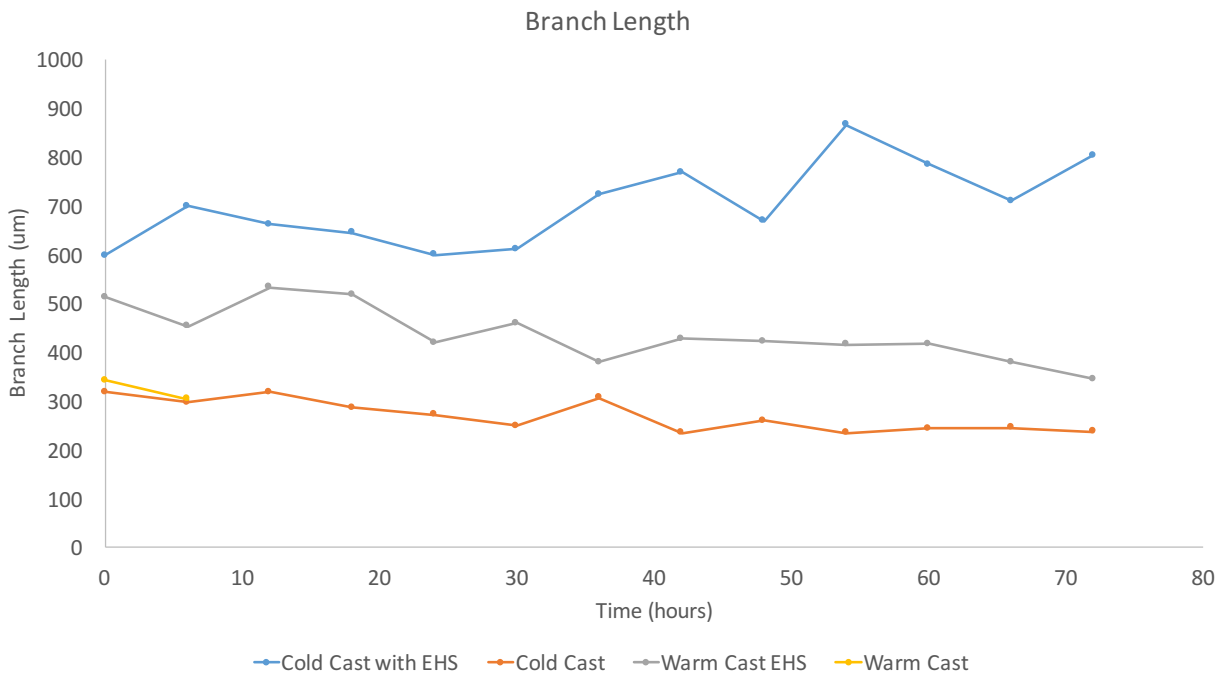

Figure 7: This graph shows the average vascular branch length every 6 hours over 72 hours. Warm cast with EHS collagen gels were not able to be imaged. Cold cast EHS collagen gels had the highest branch lengths, which cycled through growth and decay. Warm cast EHS gels were similar to the cold cast EHS gels, but had smaller branches. Cold cast gels without EHS had the lowest branch length and remained the most constant.

Next, vasculature branch lengthwas measured every 6 hours over a period of 72 hours. Results show that the vascular branch length cycles between growing and shortening over time with the conditions containing EHS, and remaining relatively constant in the warm cast condition without EHS (figure 7). Unfortunately, images for the warm cast condition without EHS could not be obtained for past 6 hours; however, the current data suggests that the branch lengths were likely similar to the cold cast without EHS condition. The cycling of growing and shortening vasculature seems to be caused by cells connecting and disconnecting to other vasculature branches, rather than continually growing in a linear fashion. Overall branch length was highest in the EHS cold cast condition, and lowest in the cold and warm casts without EHS, which is expected from previous studies.[7] EHS seems to induce a cycling growth of vasculature which slightly increases over time, while the cold cast enhances this behavior over the warm cast.

Additional ECM components available in EHS may be sequestering and presenting the growth factors available in the media in a way recognizable by the cells, eliciting an angiogenesis and vasculogenesis response. The matrix microstructure and microarchitecture changes in the cold cast may be enhancing this sequestration and release of growth factors to the cells, enhancing vasculogenesis and angiogenesis.

4. Conclusion

Matrix microstructure, microarchitecture, composition, and media type have a significant impact endothelial cell vasculogenesis and angiogenesis. Culturing endothelial cells in different media types with different levels of growth factors and FBS lead to differences in cell proliferation and cell morphology, where higher FBS and growth factor concentrations induce the most proliferative differences. Furthermore, when endothelial cells are cultured in a 3-D environment with different media types, they express more aligned vasculature with media containing greater concentrations of growth factors. These differences in endothelial cell behavior are important when considering more complex experiments involving co-cultures of two different cell types that require different growth media.

Casting conditions such as temperature and the inclusion and exclusion of EHS also show marked differences in endothelial cell behavior. Cell motility appears to be similar across conditions; however, there are differences in vascular branch lengths, suggesting that certain conditions organize cellular movement and induce cells to form vasculature. Furthermore, vasculature branch length seems to cycle through growth and shortening, connecting vasculature branches and disconnecting from them over time, which is enhanced in the EHS condition. Casting conditions using the cold cast with EHS promote the most vasculogenesis with the

longest branches, and fastest cycling, suggesting that these best mimic microenvironments that induce vasculogenesis such as in tumors. These results motivate a number of future studies including longer time lapse studies that further investigate the effects of casting conditions on vasculogenesis and angiogenesis. Furthermore, how can we best mimic the tumor microenvironment, to study the rapid angiogenesis and vasculogenesis that occurs, and what changes can be made to hinder these processes will be important to consider in future work.

5. Acknowledgements

This work was supported by the Cornell Center for Materials Research with funding from the Research Experience for Undergraduates program (DMR-1063059 and DMR-1120296). We would like to acknowledge assistance from the Imaging Facilities of Cornell's Biotechnology Resource Center (BRC; funded through NIH 1S10RR025502-01)

6. References

1. Bissell MJ, Kenny PA, Radisky DC. Microenvironmental regulators of tissue structure and function also regulate tumor induction and progression: the role of extracellular matrix and its degrading enzymes. Cold Spring Harb Symp Quant Biol. 2005;70:343-56.
2. Cheng L, Huang Z, Zhou W, Wu Q, Donnola S, Liu JK, et al. Glioblastoma stem cells generate vascular pericytes to support vessel function and tumor growth. Cell. 2013 Mar 28;153(1):139-52.
3. Infanger DW, Cho Y, Lopez BS, Mohanan S, Liu SC, Gursel D, et al. Glioblastoma stem cells are regulated by interleukin-8 signaling in a tumoral perivascular niche. Cancer Res. 2013 Dec 1;73(23):7079-89.

4. O'Brien FJ. Biomaterials & scaffolds for tissue engineering. Materials Today. 2011 3;14(3):88-95.
5. Schultz GS, Wysocki A. Interactions between extracellular matrix and growth factors in wound healing. Wound Repair Regen. 2009 Mar-Apr;17(2):153-62.
6. Siemann DW. The unique characteristics of tumor vasculature and preclinical evidence for its selective disruption by Tumor-Vascular Disrupting Agents. Cancer Treat Rev. 2011 Feb;37(1):63-74.
7. McCoy MG, Seo BR, Siyoung C, Fischbach C. Collagen I hydrogel microstructure and composition synergistically regulate vascular network formation. Journal of Materials Chemistry B. 2015. (in review)

Metal Thin Films as Oxygen Reduction Catalysts for Alkaline Fuel Cells

Andrés Molina-Villarino[*], Abigail R. Van Wassen[+], R. Bruce Van Dover[&], and Héctor D. Abruña[+]

[*]Department of Chemistry, University of Puerto Rico, Río Piedras Campus, Puerto Rico
[+]Department of Chemistry and Chemical Biology, Cornell University, Ithaca, New York
[&]Department of Materials Science and Engineering, Cornell University, Ithaca, New York

Abstract

A series of metal compositions were screened as cathode materials for catalytic activity for the oxygen reduction reaction (ORR) for alkaline fuel cells. As a continuation of a past study, a series of thin film binary compositions of Pd with Rh, Au, Ag, and Cu were sputter deposited onto glassy carbon electrodes. These were subsequently tested for ORR activity using rotating disk electrode (RDE) voltammetry. Of these, the Pd-Cu catalyst system was found to be the most effective one, considering catalytic activity and cost of the materials. A composition spread of $Pd_{1-x}Cu_x$ ($0 < x < 1$, in 0.1 increments) thin films was generated and tested. The $Pd_{0.5}Cu_{0.5}$ thin film exhibited the best performance of the catalysts tested.

Introduction

Fuel cells are a promising technology that can help address the energy crisis worldwide, because of their high energy to electricity conversion efficiency. There are different types that can be applied to newer areas including stationary power plants, vehicles, and portable devices such as laptops or mobile phones.[1] Within fuel cells, the alkaline fuel cell (**Fig. 1**) has arisen as an alternative to the more widespread acidic fuel cell, due to its potentially lower system cost and higher efficiency.

The chemical reactions involved in this system are of interest in many areas, including the oxygen reduction reaction (ORR) and oxidation of small organic molecules such as methanol in alkaline media, among others.[2] These reactions require the use of electrocatalysts so as to optimize system performance and achieve reasonable efficiencies.

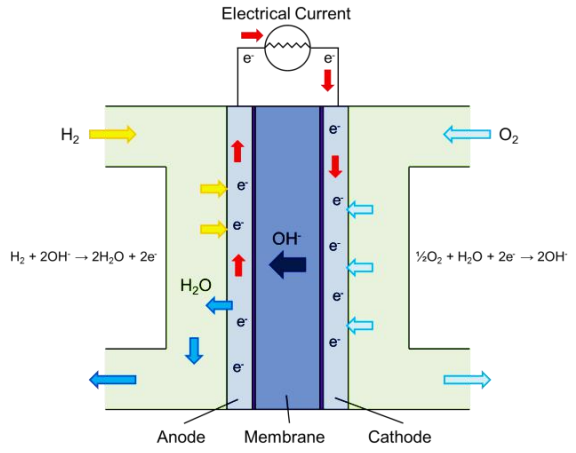

Fig. 1 Schematic of a typical alkaline fuel cell. Redrawn from www.energy.gov/eere/fuelcells/types-fuel-cells.

In this study, a high throughput method[3] was used to screen a set of catalysts for the ORR in alkaline media. Thin films composed of up to two different metal catalysts were sputter deposited onto glassy carbon electrodes that were subsequently electrochemically tested for ORR activity using rotating disk electrode (RDE) voltammetry. This approach was based on previous work by J. R. Dahn.[4]

Experimental

Reagents. Unless otherwise stated, all chemicals were used as received. Ultra high purity oxygen was purchased from Airgas®, and sodium hydroxide (≥98%) was purchased from Macron Fine Chemicals™. All aqueous solutions were prepared using deionized water from a 7148 Thermo Scientific Barnstead Nanopure dispensing system (18.2 MΩ-cm).

Electrode preparation. Glassy carbon disks (5 mm in diameter) were polished using 1, 0.3, and 0.05 μm alumina slurries until a mirror-like finish was obtained. They were rinsed with water and isopropyl alcohol and subsequently taken to a custom-built sputtering chamber[5] where films were deposited. Films were 50 nm in thickness and were deposited onto a 12 nm Ti adhesion layer initially deposited. After deposition, the disks were mounted into an exchangeable electrode tip, using a small piece of PTFE tape to provide a good seal. The electrode was then tested for ORR activity.

Electrochemical setup. Cyclic voltammetry (CV) and rotating disk electrode (RDE) voltammetry were carried out at room temperature in a three-electrode cell using a platinum-mesh counter electrode and an Ag/AgCl reference electrode. Experiments were carried out using a Pine AFRDE5 Bi-Potentiostat and a Pine AFMSRX Analytical Rotator. Prior to testing, the working electrode was cleaned electrochemically in the same 0.1 M sodium hydroxide solution that was later used for the ORR. Scan rates of 50 mV/s and 20 mV/s were used for all CV and RDE experiments, respectively, and rotation rates for RDE varied from 50 to 2000 rpm.

Results and Discussion

Based on previous work (**Fig. 2**) in which different metal thin films were screened for ORR activity, palladium was selected for a more in-depth study.

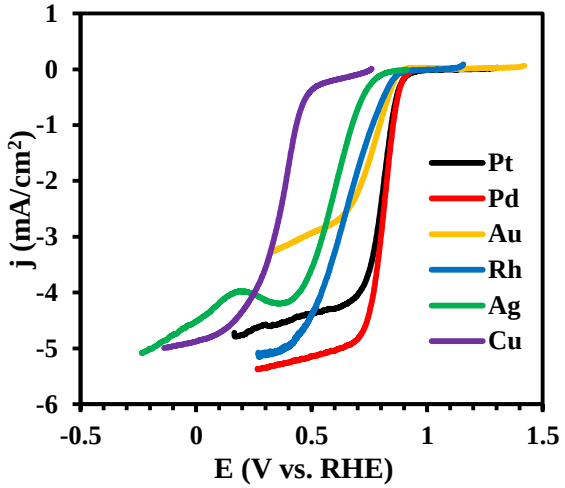

Fig. 2 RDE measurements for the ORR using different metal thin films. (O_2 saturated 0.1 M NaOH, ω = 1500 rpm, ν = 20 mV/s) c.o. Abigail Van Wassen.

The onset potential (E_{onset}; the potential at which the reaction starts to occur; calculated here as the potential at which 10% of the limiting current was observed) for palladium was observed at 0.88 V_{RHE} while for platinum, it was observed at 0.89 V_{RHE}. This value is relevant to overall efficiency, because it can be correlated to the cell voltage, which is one of the most important factors in determining fuel cell efficiency. This small difference indicates that the activity of these two catalysts is comparable. In addition the ORR on palladium proceeds by a 4 e^- transfer mechanism. These two characteristics of palladium suggest high fuel cell voltage and current, which could result in a higher overall efficiency.

Binary compositions, using palladium and the other metals studied, were prepared and tested for ORR activity, to assess how adding different metals affected catalytic activity. (**Fig. 3**)

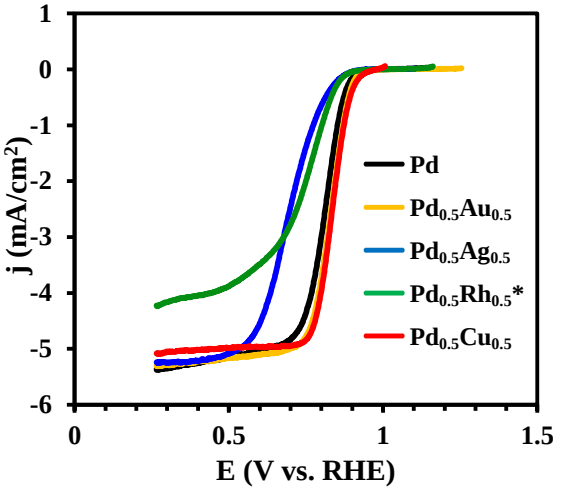

Fig. 3 RDE measurements for the ORR using different palladium composition metal thin films. (O_2 saturated 0.1 M NaOH, ω = 1500 rpm, ν = 20 mV/s) *The $Pd_{0.5}Rh_{0.5}$ film delaminated during the course of the experiment.

The $Pd_{0.5}Rh_{0.5}$ film delaminated during the experiment and the $Pd_{0.5}Ag_{0.5}$ film performed poorly, with respect to the others. On the other hand, the $Pd_{0.5}Au_{0.5}$ and $Pd_{0.5}Cu_{0.5}$ showed an enhanced catalytic activity, with onset potentials higher than that of the platinum thin film itself. Nonetheless, the $Pd_{0.5}Cu_{0.5}$ composition showed the highest E_{onset}, proving to be the best of the binary compositions tested.

Based on this observation, a composition spread of palladium and copper was generated and tested using the same methods. In this case, compositions of $Pd_{1-x}Cu_x$ ($0 < x < 1$, in 0.1 increments) were generated and tested. The results are shown in **Fig. 4**.

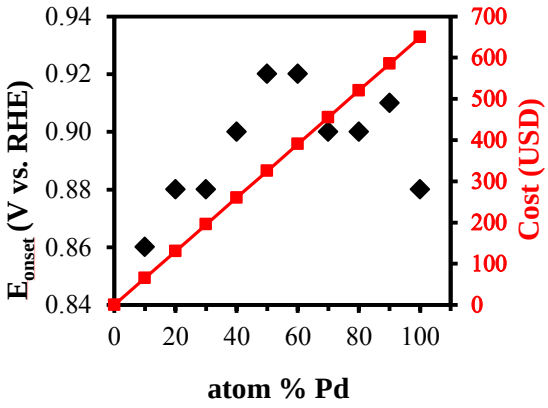

Fig. 4 Performance of Pd_xCu_{1-x} compositions, with respect to E_{onset} and overall cost. E_{onset} values were determined by RDE measurements for the ORR using the different palladium-copper thin films. (O_2 saturated 0.1 M NaOH, ω = 350 rpm, ν = 20 mV/s) The Pd_0Cu_1 thin film E_{onset} was at 0.67 V_{RHE}; this point was omitted from this graph for clarity. Prices were determined using the monthly average for Pd (Johnson Matthey) and Cu (KITCO®).

A volcano-like plot was observed with respect to the E_{onset} values for the different

palladium-copper compositions. Clearly, adding copper to the palladium catalyst improved its activity, with a maximum being reached at $Pd_{0.5}Cu_{0.5}$ and $Pd_{0.6}Cu_{0.4}$. Taking into consideration the activity and the cost and abundance of the screened catalysts, the best option for a fuel cell catalyst operating under alkaline conditions would be the $Pd_{0.5}Cu_{0.5}$, which would cost less than a third of the price of platinum.

Conclusions

Of the tested cathode materials as oxygen reduction catalysts for alkaline fuel cells, $Pd_{0.5}Cu_{0.5}$ proved to be the most efficient and effective material, in terms of E_{onset} and cost. Its activity was better than that of palladium and platinum. Even though more extensive research on the real applicability of this material and its roughness would be needed to claim that a real alternative to platinum for fuel cells has been developed, this study showed that $Pd_{0.5}Cu_{0.5}$ represents a promising route for research and improvement.

Acknowledgments

Andrés Molina-Villarino thanks the CCMR REU and the MARC Program for providing the opportunity and funds for this summer research. Special thanks to: my mentor, Abigail R. Van Wassen, Prof. R. Bruce van Dover, Prof. Héctor D. Abruña, and the rest of the Abruña Group at Cornell University for all the shared knowledge and teaching.

References

(1) Carrette, L.; Friedrich, K. A.; Stimming, U. *Fuel Cells* **2001**, *1* (1), 5.

(2) Spendelow, J. S.; Wieckowski, A. *Phys. Chem. Chem. Phys.* **2007**, *9* (21), 2654.

(3) Muster, T. H.; Trinchi, A.; Markley, T. A.; Lau, D.; Martin, P.; Bradbury, A.; Bendavid, A.; Dligatch, S. *Electrochimica Acta* **2011**, *56* (27), 9679.

(4) Liu, G. C.-K.; Sanderson, R. J.; Vernstrom, G.; Stevens, D. A.; Atanasoski, R. T.; Debe, M. K.; Dahn, J. R. *J. Electrochem. Soc.* **2010**, *157* (2), B207.

(5) Gregoire, J. M.; van Dover, R. B.; Jin, J.; Disalvo, F. J.; Abruña, H. D. *Rev. Sci. Instrum.* **2007**, *78* (7), 072212.